REPORT DOCUMENTATION PAGE

Form Approved OMB NO. 0704-0188

1. REPORT DATE (DD-MM-YYYY)	2. REPORT TYPE	3. DATES COVERED (From - To)
18-11-2014	Ph.D. Dissertation	-

4. TITLE AND SUBTITLE
Encapsulated and Monolithic Resonant Structures for Laser Applications

5a. CONTRACT NUMBER
W911NF-11-1-0297

5b. GRANT NUMBER

5c. PROGRAM ELEMENT NUMBER
611103

6. AUTHORS
Aaron Pung

5d. PROJECT NUMBER

5e. TASK NUMBER

5f. WORK UNIT NUMBER

7. PERFORMING ORGANIZATION NAMES AND ADDRESSES
University of Central Florida
Sponsored Programs
12201 Research Parkway, Suite 501
Orlando, FL 32826 -3246

8. PERFORMING ORGANIZATION REPORT NUMBER

9. SPONSORING/MONITORING AGENCY NAME(S) AND ADDRESS (ES)
U.S. Army Research Office
P.O. Box 12211
Research Triangle Park, NC 27709-2211

10. SPONSOR/MONITOR'S ACRONYM(S)
ARO

11. SPONSOR/MONITOR'S REPORT NUMBER(S)
59727-PH-MUR.75

12. DISTRIBUTION AVAILIBILITY STATEMENT
Approved for public release; distribution is unlimited.

13. SUPPLEMENTARY NOTES
The views, opinions and/or findings contained in this report are those of the author(s) and should not contrued as an official Department of the Army position, policy or decision, unless so designated by other documentation.

14. ABSTRACT
Typically, the composition of a laser system includes a gain medium, a pump illumination source, and an external feedback cavity. This cavity consists of a highly reflective mirror and an outcoupler component. The geometry of the outcoupler can be engineered to tailor the reflected or transmitted beam?s spatial and spectral distribution. Functionally, the transmitted beam profile is dependent on the laser application. Broadband reflection profiles can be obtained by utilizing a distributed Bragg reflector (DBR). A DBR device consists of multiple layers of alternating materials. Constructive interference of the reflected light off each interface between different materials

15. SUBJECT TERMS
Resonant Structures

16. SECURITY CLASSIFICATION OF:			17. LIMITATION OF ABSTRACT	15. NUMBER OF PAGES	19a. NAME OF RESPONSIBLE PERSON
a. REPORT	b. ABSTRACT	c. THIS PAGE			Martin Richardson
UU	UU	UU	UU		19b. TELEPHONE NUMBER 407-823-6819

Report Title

Encapsulated and Monolithic Resonant Structures for Laser Applications

ABSTRACT

Typically, the composition of a laser system includes a gain medium, a pump illumination source, and an external feedback cavity. This cavity consists of a highly reflective mirror and an outcoupler component. The geometry of the outcoupler can be engineered to tailor the reflected or transmitted beam?s spatial and spectral distribution. Functionally, the transmitted beam profile is dependent on the laser application. Broadband reflection profiles can be obtained by utilizing a distributed Bragg reflector (DBR). A DBR device consists of multiple layers of alternating materials. Constructive interference of the reflected light off each interface between different materials produces the spectrally broadband response. The spectral response is a function of the fabrication and material parameters of the DBR.

ENCAPSULATED AND MONOLITHIC RESONANT STRUCTURES FOR LASER APPLICATIONS

A Dissertation
Presented to
the Graduate School of
Clemson University

In Partial Fulfillment
of the Requirements for the Degree
Doctor of Philosophy

---

by
Aaron Joseph Pung
December 2013

Accepted by:
Dr. Eric G. Johnson, Committee Chair
Dr. John Ballato
Dr. Liang Dong
Dr. William Harrell
Dr. Lin Zhu

ABSTRACT

Typically, the composition of a laser system includes a gain medium, a pump illumination source, and an external feedback cavity. This cavity consists of a highly reflective mirror and an outcoupler component. The geometry of the outcoupler can be engineered to tailor the reflected or transmitted beam's spatial and spectral distribution. Functionally, the transmitted beam profile is dependent on the laser application. Broadband reflection profiles can be obtained by utilizing a distributed Bragg reflector (DBR). A DBR device consists of multiple layers of alternating materials. Constructive interference of the reflected light off each interface between different materials produces the spectrally broadband response. The spectral response is a function of the fabrication and material parameters of the DBR.

In contrast, guided-mode resonance filters (GMRF) exploit phase matching between evanescent- and guided-waves to provide a strong reflection. Based on the materials in the structure, the spectral response can demonstrate broadband or narrowband reflectivity. The operation wavelength of a GMRF is dependent on the structural parameters of the device as well as the angle of incidence. However, conventional designs of resonant optics leave critical aspects of the structure exposed to the surrounding environment. Additional damage or contamination to the waveguide or grating layer will significantly alter the device's spectral response.

This dissertation introduces two GMRF geometries aimed at device integration, development of similar-material resonant devices, and full-device protection from outside influence. Unlike distributed Bragg reflectors, these geometries do not rely heavily on

strict material and deposition requirements. Instead, they take advantage of the deposition processes to minimize coating deposition, achieve high reflectivity and demonstrate control over polarization dependence. Given their versatility in design and ability to withstand high power densities, these resonant structures find applications in fiber laser systems, spectral beam combining, and standard laser cavities.

DEDICATION

This dissertation is dedicated to my family, friends, and those who have relentlessly encouraged me along the way.

ACKNOWLEDGMENTS

I would like to thank my advisor, Dr. Eric Johnson, for his guidance, insight, and support throughout my graduate studies. Without his support to ongoing research opportunities, access to necessary equipment and facilities, and funding, this research effort would not have been possible.

Additionally, I would like to thank my committee members for their time, effort, and helpful advice: Dr. John Ballato, Dr. Liang Dong, Dr. William R. Harrell, and Dr. Lin Zhu. I would like to acknowledge Dr. Menelaos Poutous for his patience and training. Furthermore, I would like to thank Dr. Kristan Corwin for starting me on the path of optics research during my undergraduate years and Dr. Rich Fox for sustaining and increasing my interest.

I wish to thank my family for their undying support and words of encouragement. Furthermore, I would like to apologize for the distance and missed holiday occasions. You've been in my thoughts the entire journey.

I would like to thank the past and present members of the Micro-Photonics Laboratory as well as my colleague Zack A. Warren who supported this effort. Your time, effort, humor, and advice are priceless and greatly appreciated.

Lastly, I would like to thank my cat Snoball, for keeping me company over the years. She's happily offered many needed study breaks and numerous distractions; she will be repaid in full with cookies.

TABLE OF CONTENTS

Page

Table of Contents (Continued)

LIST OF TABLES

Table Page

LIST OF FIGURES

List of Figures (Continued)

Figure Page

List of Figures (Continued)

Figure Page

List of Figures (Continued)

Figure Page

List of Figures (Continued)

Figure Page

List of Figures (Continued)

Figure Page

List of Figures (Continued)

Figure Page

List of Figures (Continued)

Figure Page

List of Figures (Continued)

Figure Page

LIST OF ACRONYMS

ALD – Atomic Layer Deposition

ASE – Amplified Spontaneous Emission

DBR – Distributed Bragg Reflector

FDFD – Finite-Difference Frequency-Domain

FWHM – Full width at half maximum

GMRF – Guided-Mode Resonance Filter

ICP – Inductively Coupled Plasma

LASER – Light Amplification by Stimulated Emission of Radiation

LED – Light Emitting Diode

NIF – National Ignition Facility

PECVD – Plasma Enhanced Chemical Vapor Deposition

RCWA – Rigorous Coupled-Wave Analysis

RIE – Reactive Ion Etching

SEM – Scanning Electron Microscope

TMA – Trimethyl Aluminum

CHAPTER ONE

INTRODUCTION AND MOTIVATION

1.1 Introduction

The study of optics relies heavily on the ability to create, manipulate, and detect electromagnetic radiation. Once light is injected in an optical system, properties of the incident light (wavelength, amplitude, phase, polarization) may be precisely controlled by using basic optical components. These components include mirrors, gratings, prisms, and waveguides. Light exiting the system may be detected and characterized by use of a wavelength appropriate camera, beam block, or power meter. However, the functionality of each component is strongly dependent on the properties of the incident radiation due to chromatic dispersion and absorption.

In an effort to better control the characteristics of light introduced into the experiment, a variety of lighting sources have been developed. While polychromatic light can be obtained from white light and amplified spontaneous emission (ASE) sources [1], gas discharge lamps and light emitting diodes (LEDs) provide a more narrowband light source with a bandwidth of ~20 nm [2]. Further decrease in the source's bandwidth can be obtained through stimulated emission, offering a coherent and narrow linewidth source capable of amplification to extremely high power densities.

Due to the increasing presence of photonics in modern technology, laser systems now play a crucial role in many aspects of electronic devices. Specifically, their compact size, high efficiency, spectral linewidth, and output power are useful for system size

reduction and increased processing speed. The on-going progress of technology creates an ever-increasing opportunity for new applications and demands new materials and component geometries to provide better control over a system's light source. The latter topic is the focus of this dissertation.

The foundations of stimulated emission of radiation were introduced theoretically by Albert Einstein in 1916 [3] and 1917 [4]. With experimental verification of the theory demonstrated in 1928, the first practical oscillator design was conceived in 1951 by Charles Townes [5]. The first oscillator, based on an ammonia beam, was demonstrated by Townes, Gordon, and Zeiger in 1954 [6]. Soon thereafter, infrared and optical (visible) masers were developed [7], followed quickly by the first laser system in 1960 [8]. Since then, laser geometries have been developed using a variety of gain media. Together, these materials create a continuous regime from 0.2 μm (dye layers) to 27 μm (Pb salts) that coherent, monochromatic light may be obtained. Still longer wavelength sources exist in the millimeter wavelengths, based on methanol [9], methylamine [10], and methyl fluoride [11]. However, modern solid state laser systems based on alexandrite laser-pumped LiF:F_2^+ have also been developed, tunable from 0.2 μm – 10 μm [12].

Additional control over the output power of the laser system is also technology enabling. Low power handheld laser pointers emit 1–5 mW of power, while more powerful micro-machining diode-pumped lasers are capable of emitting 220 W of pulsed power [13]. At greater output powers, CO_2 lasers are capable of extending this limit to 100 kW [14], while extreme sources produced at Lawrence Livermore National Laboratory's National Ignition Facility (NIF) generate greater than 1.5 PW [15].

The arrangement of an external laser cavity employs two reflective components. The first, a high reflectivity mirror, provides strong feedback to maintain a large population of photons within the cavity. The second component, an outcoupler, has a slightly lower reflectivity allowing part of the beam to be removed from the laser cavity. In doing so, the exiting beam's characteristics – wavelength, amplitude, polarization, and phase – can be strongly influenced by the outcoupler geometry. These are shown in Fig. 1.1a. By controlling the spectral response of the out-coupler, different applications for the out-couplers can be realized. In one application, multiple couplers are used, each with a different reflectivity wavelength. Since the devices are made to work at an off-normal angle of incidence, the devices can be stacked for spectral beam combining. This is illustrated in Fig. 1.1b [16]. Thirdly, out-couplers have been used as the feedback element in infrared fiber lasers, as illustrated in Fig. 1.1c [17].

One well-known solution for obtaining broadband spectral reflectivity is the distributed Bragg reflector (DBR). Constructed from alternating, planar layers of high- and low-index materials, the profile of a DBR stack resembles a vertical 1-dimensional grating. Due to subsequent reflections from consecutive layer interfaces, constructive interference may be achieved if the refractive index and thickness of each layer satisfies the required phase matching conditions. Therefore, strict tolerances are inherently placed on the material and thickness needed for each layer to obtain the desired reflectivity profile. Furthermore, the geometry of the DBR stack limits the functionality of the device -- due to the non-structured surface, polarization dependence cannot be tailored nor spatially varied across the full device to achieve a spatially-varying response. As the

number of layers increases, a greater amount of material must be used during fabrication of the DBR stack compared with conventional resonant designs. Lastly, the use of multiple materials gives rise to differential thermal problems that arise at increasingly high power densities including thermal expansion, layer mismatch, and a change in refractive indices.

Plane ruled reflection gratings also provide a solution for wavelength stabilization and tuning within a laser cavity, but they, too, suffer from a number of limitations. These include low diffraction efficiency, sub-nanometer spectral stability due to thermally-induced distortion, and long free-space cavity sections are required for minimal output linewidth [20].

To eliminate these limitations, GMRFs were explored as a solution for spatially and spectrally controlling the reflected and transmitted beam characteristics of a laser system. Conventional and modified resonant structures were used as a means to minimize the amount of material deposited during fabrication. The structured surface allows for both polarization independent and polarization dependent spectra to be realized. As discussed below, these grating geometries have used spatially-static and spatially-variant structures to encode additional functionality into the outcoupler optic.

For resonant devices with a single spatial pattern, linear grating geometries have demonstrated narrowband high reflectivity at 2 μm for 100 W average power [21]. In order to eliminate the polarization sensitivity of the spectral response, hexagonal and square arrays of holes or posts may be used. Based on the polarization properties of the incident beam, polarization-independent geometries may be used to increase the overall

signal in the optical system, since reflectivity from the outcoupler component will be greater. In one application, both square- and hexagonal gratings demonstrated high reflectivity at 2.8 μm in an Er:ZBLAN fiber-based laser [18]. Additionally, recent GMRF designs have incorporated an anti-reflective surface with a linear grating for use at oblique angles of incidence [19]. These designs are illustrated in Fig. 1.1(d –g).

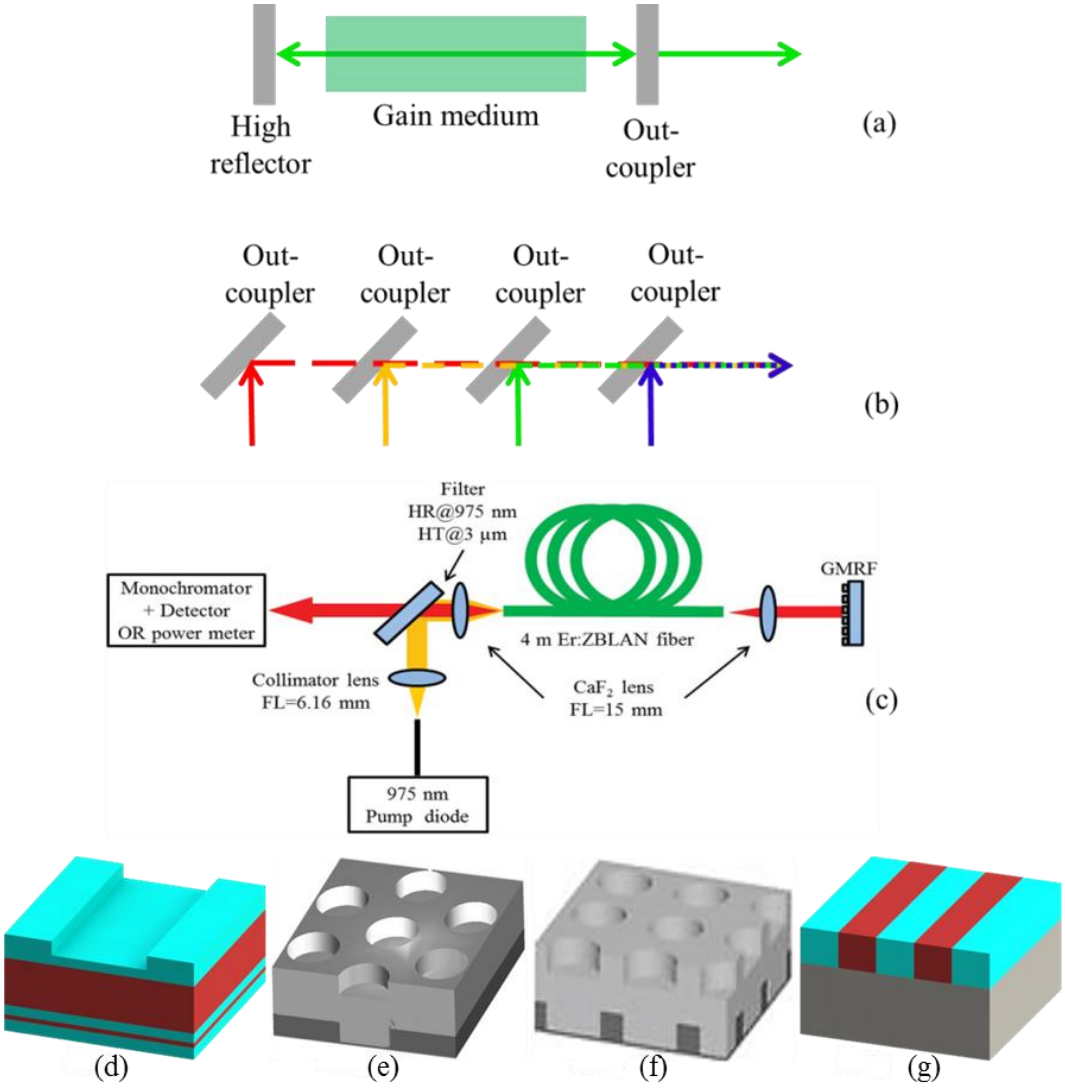

Fig. 1.1. Illustrations are shown for (a) a typical laser cavity, (b) out-couplers in a beam combining configuration [16], and (c) an out-coupler as the feedback element in a fiber laser system [17]. Device geometries are demonstrated for (d) a narrowband high reflector [21], (e) a unit cell for hexagonal, (f) a square array of holes [18], and (g) an anti-reflective surface based on a linear grating geometry [19].

Functionality of the resonant outcoupler component may be increased by spatially varying a single pattern. This step is done lithographically by adding a spatially-varying exposure to a pre-existing grating exposure. Such geometries have been investigated for customization of the reflected or transmitted beam's field profile. For instance, the polarization of a transmitted beam may be achieved using rotated linear grating segments, stitched together to create spatially varying resonant structures. These structures have been used as polarization converting elements for increased coupling in cylindrical hollow waveguides [22].

Further increasing the design's complexity, the fill fraction of the holes in a hexagonal array was spatially varied to demonstrate multiple resonance profiles within a single device. These devices have simultaneously shown polarization-selectivity and wavelength-dependent radial beam shaping [23]. Still other device geometries utilize azimuthal variation of the grating's fill factor to create wavelength-dependent azimuthally variation in the transmitted beam profile [24]. The spatially variant geometries of these optics are shown in Fig. 1.2; Figs. 1.3 and 1.4 illustrate the wavelength dependence of the transmitted beam profile for the radial and azimuthal GMRF devices. Changes in the transmitted beam's polarization are a function of the polarization sensitivity of the out-coupling mirror. The beam profile may be altered by creating a phase offset as the light passes through the device.

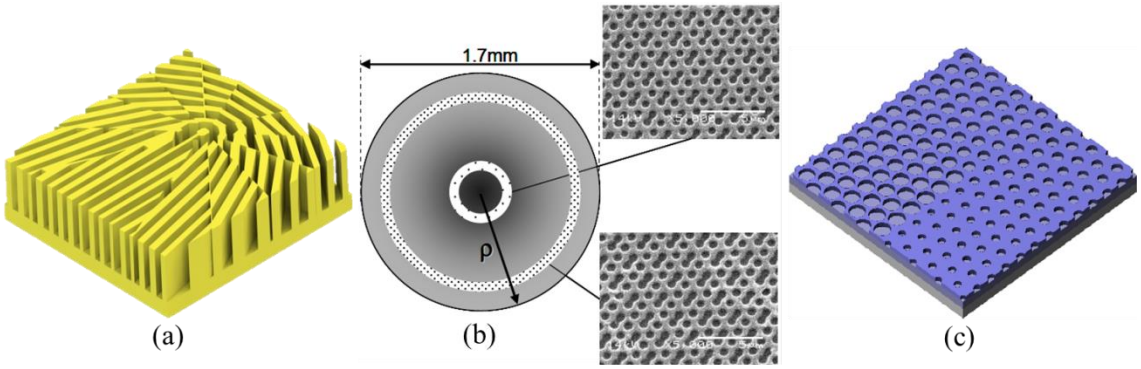

Fig. 1.2. Spatially variant device geometries are illustrated for (a) a polarization converting element [22], (b) a radially variant GMRF [23], and (c) an azimuthally variant GMRF [24].

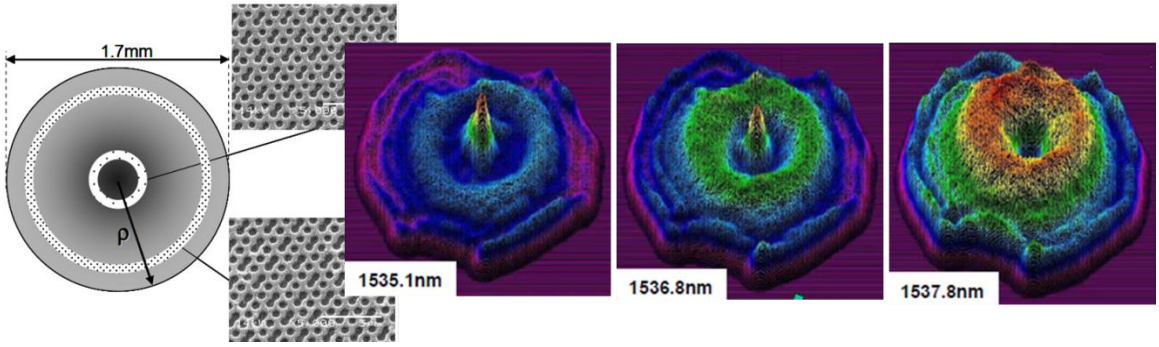

Fig. 1.3. (Left) The device geometry is illustrated for a radially varying hole diameter. (Right) Experimental beam profiles demonstrate the effect of a radial variation at different wavelengths (1535.1 nm, 1536.8 nm, and 1537.8 nm) [23].

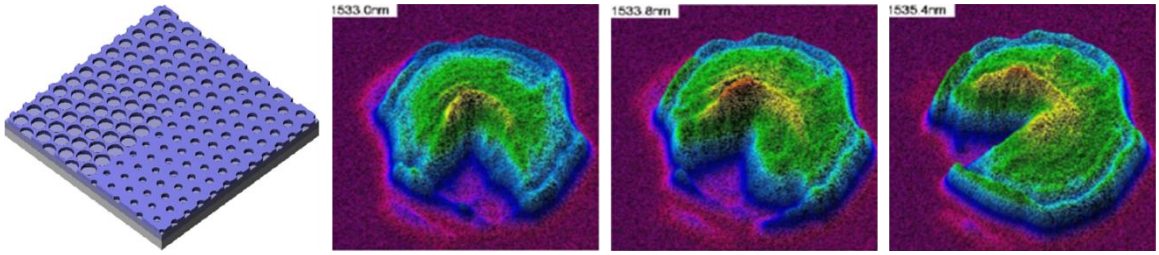

Fig. 1.4. (Left) The device geometry is illustrated for an azimuthally varying hole diameter. (Right) Experimental beam profiles demonstrate the effect of azimuthal variation in hole diameter at different wavelengths (1533.0 nm, 1533.8 nm, and 1535.4 nm) [24].

The resonances demonstrated in Fig. 1.3 vary spectrally from 1535.1 nm to 1537.8 nm. During this time, the reflected and transmitted profiles will change with respect to wavelength, as shown. Due to the transmission-based profile measurements, the reflected beam profile at 1535.1 nm would resemble a doughnut since only the central portion of the beam is transmitted. However, at an incident wavelength of 1537.8 nm, the reflected beam profile would now resemble a tightly confined spot similar to the transmitted profile of 1535.1 nm. These transmission profiles are achieved by radially varying the duty cycle of the hexagonal grating. The stability of a resonance in one part of the grating at a given wavelength is obtained, while resonance conditions at another radial location on the grating are not supported for the same wavelength. While the specific operation wavelengths of this device may be tailored, the importance of spatial variation within the grating enables resonant devices to be used as spatial beam shaping elements.

A similar concept may be applied to the azimuthally varying device in Fig. 1.4. For instance, at 1533.0 nm incident wavelength, a pie wedge is formed in the reflected region, leaving a similar-pie wedge missing from the transmitted spectrum. As the incident wavelength is incrementally increased, the resonant conditions of the first profile are no longer valid. However, resonances conditions are met in adjacent portions of the grating, forming a continuous sweep of the pie wedge around the center of the device. This is shown in the transmitted beam profiles as the incident wavelength is swept from 1533.0 nm to 1535.4 nm.

1.2 Motivation

Due to the narrowband GMRF's high degree of sensitivity, they have found a variety of applications in sensing and filtering. The change in spectral profile due to a change in the surrounding environment has applications in spectral beam combining [16], biosensors [25]–[28], pollution sensing [29], color filters [30], humidity sensors [31], and spectroscopy [32].

When used as outcoupler components, this sensitivity is not desired because strong, stable reflectance is needed within the laser cavity to ensure wavelength stabilization. Therefore, it is imperative that the geometry and operation of the device are robust enough to withstand changes in the application environment. For use in lasing systems, this means that the location and profile of the resonance should not change over time. Since the resonance condition is a function of the device geometry, any deviation from the ideal geometry will lead to a different resonance condition and spectral response. Given the typical beam size of the source and relative period of the grating, contamination on the surface from dust, dirt, or other impurities could cause the resonance to shift to an undesired wavelength or alter the reflectivity profile. Thus, one current problem with the technology lies with preserving the cleanliness of the grating surface to conserve the resonance condition under any environment.

A second major concern regarding these resonance device geometries is their application at high power. As with any optical device, the materials associated with the device have properties that change as a function of power (through the Kerr effect) and temperature, including refractive index (dn/dT) and mechanical expansion, characterized

by the coefficient of thermal expansion (CTE). These differ greatly between the most commonly used materials used in micro-fabrication. For example, the CTE value of silicon nitride is ~5.8 times greater than that of fused silica [33]. At extremely high power densities, the devices undergo large temperature variations, and can cause the materials to expand at different rates with respect to each other. This leads to the possibility of fatigue and failure of the device, as well as stress-optic influences that will greatly impact performance.

For resonant structures, this effect is amplified due to the standing wave at resonance. While the field amplification at resonance may be found computationally, the relationship between the linewidth and the maximum electric field intensity (MEFI) at resonance has been previously investigated [34]. If the difference between the CTE values is large, the materials will not expand uniformly, causing cracking, delamination, or separation between the layers. On the other hand, if the refractive indices change greatly with respect to each other, a large variation in index contrast will be seen within the structure. In this case, the resonance conditions will differ from the intended geometry and the desired spectral response will be lost. Solutions to these problems are required as newer and more exotic out-coupler geometries become present within modern devices.

Therefore, the thesis of this work is the development of robust solutions to solve current problems in high power optical systems. Given the prevalence of lasers in modern technology, this work's relevance is derived from its potential to create robust optical resonators. Their ability to address issues regarding contamination, delamination, and

deposition cracking increase overall system stability. In parallel, they can act as control elements for power scaling, beam condition, shaping, combining and splitting, polarization and spectral selectivity.

Chapter 2 discusses the techniques used to analyze the spectral response of the resonant structures. Closed-form solutions are obtained for distributed Bragg reflectors as well as resonant structures. Both devices are analyzed using a Rigorous Coupled-Wave Analysis routine. Particle Swarm Optimization is discussed as a means to efficiently search a multi-modal solution space for a 'best' solution. Finally, three specific examples are given to illustrate the practicality of these techniques.

Chapter 3 presents a monolithic resonant structure as a solution to thermal issues in high power laser systems. The device is constructed from two similar ultra-low CTE materials. This allows the substrate to expand at the same rate as the device layers, preserving the shape and dimensions of the structure. An ideal geometry is introduced, along with an exploration of the effect of varying the fabrication parameters. Device fabrication is examined with an emphasis on the formation of the submerged air void and top waveguide formation. The fabricated device is then imaged, tested, and computationally investigated.

Chapter 4 discusses a device geometry that utilizes encapsulation to remove the resonant structure from contamination. Similar in format to Chapter 3, an ideal device geometry is presented along with its spectral response. The spectral response is then examined as a function of varying the fabrication parameters of the device. The fabrication process of the device and a cross-section of the image are examined.

Experimental results are shown for the fabricated device, and the process space is again explored for the realistic device geometry.

Appendix A offers a detailed explanation of the specific fabrication steps, including substrate preparation, photoresist application, the post-applied and post-exposure bake, pattern exposure, development, etching, and deposition.

Appendix B investigates the effects of finite beam size on the spectral response of the GMRFs. It will be shown that as the diameter of the incident beam decreases, the device's reflectivity decreases in a predictable manner. Simulation and experimental results are compared for a top-hat beam profile.

CHAPTER TWO

DESIGN AND SIMULATION

2.1 Introduction

Modern optical systems range from simple multi-lens arrangements to complex integrated circuits. In order to understand and estimate the performance of any one of these systems, simulations of the devices' performance are desired. For most structures, both analytic and numerical tools can be used. While most details of the spectral performance of a distributed Bragg reflector (DBR) may be found analytically, this is not the case with GMRFs – only the spectral location of the GMRF's resonance may be predicted analytically. Other details about the device's spectral performance (e.g. full-width at half maximum (FWHM), reflectivity, symmetry) must be determined using numerical simulations.

Increasing the complexity of a device typically increases the number of fabrication parameters. Since each of these parameters plays a role in determining the spectral profile, fast computation and optimization are desired. To this end, rigorous coupled-wave analysis (RCWA) was used to determine the spectral characteristics of the designs discussed throughout this work. In certain designs, optimization of the fabrication parameters becomes imperative for the required functionality of the device. To save time, particle swarm optimization (PSO) was used in conjunction with RCWA simulations. These simulation techniques are discussed below, followed by results in a conventional DBR, a conventional GMRF, and an inverted broadband reflector.

2.2 Rigorous Coupled-Wave Analysis

As previously stated, the mode distribution in the waveguide of a guided-mode resonance is described by a transcendental equation, whose solutions must be determined numerically. The spectral location of the resonance, however, is obtained through the phase matching condition applied to the grating equation [35]. To gain an accurate understanding of device behavior and spectral response, several computation routines have been developed. These include transfer matrix method (TMM), scattering matrix method (SMM), Plane-Wave Expansion Method (PWEM), Waveguide Mode Analysis (WMA), Method of Lines (MoL), Rigorous Coupled-Wave Analysis (RCWA), and Finite-Difference Frequency-Domain (FDFD).

RCWA is a method for analyzing electromagnetic diffraction of a plane wave incident on a planar grating [36] as well as many other geometries. It utilizes a semi-analytical approach; the device geometry is defined along the lateral axes (X-Y) allowing plane wave solutions and spatial harmonics of the electromagnetic field to be numerically solved for a single layer. Each layer is assumed to be constant along the vertical (Z) axis and the numerical solutions for each layer are analytically propagated to the next layer using PWEM. No assumptions are made regarding the source or materials. Transmission and reflection are calculated prior to finding the mode coefficients, allowing for the fields to be visualized inside the device.

This formulation assumes infinite repetition of the designated unit cell. Field calculations are based in the frequency-domain, permitting calculations to be done for any angle of incidence and incorporate dispersion for accurate material response. Due to

the analytic portion of the solution, efficient scaling in the vertical axis allows for any number of layers. However, device construction scales poorly in the lateral axes, and high index contrast or use of metals causes poor solution convergence due to Gibb's phenomenon.

The derivative forms of Maxwell's equations are given in equation (2.1).

$$\begin{aligned} \nabla \bullet \vec{B} &= 0 \\ \nabla \bullet \vec{D} &= \rho_x \\ \nabla \times \vec{E} &= -j\omega\vec{B} \\ \nabla \times \vec{H} &= -j\omega\vec{D} + \vec{J} \end{aligned} \tag{2.1}$$

The constitutive relations, $\vec{D} = \varepsilon\vec{E}$ and $\vec{B} = \mu\vec{H}$, relate the displacement current ($\vec{D}$) to the permittivity and induced electric field ($\vec{E}$), and the magnetic field ($\vec{H}$) to the permeability and the induced magnetic field ($\vec{B}$). The curl of a 3-dimensional field can be expanded to relate the spatial components to the orthogonal field [37].

$$\nabla \times E = \left(\frac{\partial E_z}{\partial y} - \frac{\partial E_y}{\partial z}\right) i + \left(\frac{\partial E_x}{\partial z} - \frac{\partial E_z}{\partial x}\right) j + \left(\frac{\partial E_y}{\partial x} - \frac{\partial E_x}{\partial y}\right) k. \tag{2.2}$$

Applying (2.2) to Maxwell's equations, (2.3) and (2.4) are obtained [38]. Assuming that isotropic materials are used, the E- and H-fields can be normalized to produce the right-hand side terms.

$$\begin{aligned} \nabla \times \vec{E} &= -j\omega\mu_0\mu_r\vec{H} \Rightarrow \\ \frac{\partial E_z}{\partial y} - \frac{\partial E_y}{\partial z} &= -j\omega\mu_0\mu_r H_x = \mu_{xx}\tilde{H}_x \\ \frac{\partial E_x}{\partial z} - \frac{\partial E_z}{\partial x} &= -j\omega\mu_0\mu_r H_y = \mu_{yy}\tilde{H}_y \\ \frac{\partial E_y}{\partial x} - \frac{\partial E_x}{\partial y} &= -j\omega\mu_0\mu_r H_z = \mu_{zz}\tilde{H}_z \end{aligned} \tag{2.3}$$

$$
\begin{aligned}
\nabla \times \vec{H} &= j\omega\varepsilon_0\varepsilon_r\vec{E} \Rightarrow \\
\frac{\partial H_z}{\partial y} - \frac{\partial H_y}{\partial z} &= j\omega\varepsilon_0\varepsilon_r E_x = \varepsilon_{xx}E_x \\
\frac{\partial H_x}{\partial z} - \frac{\partial H_z}{\partial x} &= j\omega\varepsilon_0\varepsilon_r E_y = \varepsilon_{yy}E_y \\
\frac{\partial H_y}{\partial x} - \frac{\partial H_x}{\partial y} &= j\omega\varepsilon_0\varepsilon_r E_z = \varepsilon_{zz}E_z
\end{aligned}
\tag{2.4}
$$

Due to the numeric solution in the x-y plane, the components' Fourier transform is only taken along these lateral directions, while the z component remains unchanged. The periodic relative permittivity can be expanded in a Fourier series; a similar description is used for the periodic relative permeability [39]. Given the Fourier components, the plane wave amplitude, the E- and H-field components can be described by equations (2.5) and (2.6). The wave vector components ($k_{x,m}$ and $k_{y,n}$) are given by $k_{x,m} = k_{x,inc} - 2\pi m/\Lambda_x$ and $k_{y,n} = k_{y,inc} - 2\pi n/\Lambda_y$, where m and n are integer values representing the diffractive order; $k_{x,inc}$ and $k_{y,inc}$ are the wave vectors of the incident field [40].

$$
\begin{aligned}
E_x(x,y,z) &= \sum_{m=-\infty}^{\infty}\sum_{n=-\infty}^{\infty}\vec{S}_{x,m,n}(z)\cdot e^{-j(k_{x,m}x+k_{y,m}y)} \\
E_y(x,y,z) &= \sum_{m=-\infty}^{\infty}\sum_{n=-\infty}^{\infty}\vec{S}_{y,m,n}(z)\cdot e^{-j(k_{x,m}x+k_{y,m}y)} \\
E_z(x,y,z) &= \sum_{m=-\infty}^{\infty}\sum_{n=-\infty}^{\infty}\vec{S}_{z,m,n}(z)\cdot e^{-j(k_{x,m}x+k_{y,m}y)}
\end{aligned}
\tag{2.5}
$$

$$\tilde{H}_x(x,y,z) = \sum_{m=-\infty}^{\infty}\sum_{n=-\infty}^{\infty} U_{x,m,n}(z)\cdot e^{-j(k_{x,m}x+k_{y,m}y)}$$
$$\tilde{H}_y(x,y,z) = \sum_{m=-\infty}^{\infty}\sum_{n=-\infty}^{\infty} U_{y,m,n}(z)\cdot e^{-j(k_{x,m}x+k_{y,m}y)} \quad (2.6)$$
$$\tilde{H}_z(x,y,z) = \sum_{m=-\infty}^{\infty}\sum_{n=-\infty}^{\infty} U_{z,m,n}(z)\cdot e^{-j(k_{x,m}x+k_{y,m}y)}$$

Substitution of (2.5) and (2.6) into equations (2.3) and (2.4) yields Maxwell's equations in Fourier space. Renormalizing the wave vectors and z-component using $\tilde{k}_x = k_x/k_0$, $\tilde{k}_y = k_y/k_0$, $\tilde{k}_z = k_z/k_0$, and $\tilde{z} = k_0 z$ gives rise to equations (2.7) and (2.8).

$$-j\tilde{k}_{y,m}U_{z,m,n}(\tilde{z}) - \frac{dU_{y,m,n}(\tilde{z})}{d\tilde{z}} = \sum_{q=-\infty}^{\infty}\sum_{r=-\infty}^{\infty} a_{m-q,n-r}S_{x,q,r}(\tilde{z})$$
$$\frac{dU_{x,m,n}(\tilde{z})}{d\tilde{z}} + j\tilde{k}_{x,m}U_{z,m,n}(\tilde{z}) = \sum_{q=-\infty}^{\infty}\sum_{r=-\infty}^{\infty} a_{m-q,n-r}S_{y,q,r}(\tilde{z}) \quad (2.7)$$
$$-j\tilde{k}_{x,m}U_{y,m,n}(\tilde{z}) + jk_{y,m}U_{x,m,n}(\tilde{z}) = \sum_{q=-\infty}^{\infty}\sum_{r=-\infty}^{\infty} a_{m-q,n-r}S_{z,q,r}(\tilde{z})$$

$$-j\tilde{k}_{y,m}S_{z,m,n}(\tilde{z}) - \frac{dS_{y,m,n}(\tilde{z})}{dz} = \sum_{q=-\infty}^{\infty}\sum_{r=-\infty}^{\infty} b_{m-q,n-r}U_{x,q,r}(\tilde{z})$$
$$\frac{dS_{x,m,n}(\tilde{z})}{dz} + j\tilde{k}_{x,m}S_{z,m,n}(\tilde{z}) = \sum_{q=-\infty}^{\infty}\sum_{r=-\infty}^{\infty} b_{m-q,n-r}U_{y,q,r}(\tilde{z}) \quad (2.8)$$
$$-j\tilde{k}_{x,m}S_{y,m,n}(\tilde{z}) + j\tilde{k}_{y,m}S_{x,m,n}(\tilde{z}) = \sum_{q=-\infty}^{\infty}\sum_{r=-\infty}^{\infty} b_{m-q,n-r}U_{z,q,r}(\tilde{z})$$

These equations are solved at every point in the X-Y plane, for all combinations of *m* and *n*. The size of the resulting equations is rather large, and is better handled in matrices of the form $-j\mathbf{K}_y\mathbf{u}_z - \frac{d}{d\tilde{z}}\mathbf{u}_y = \boldsymbol{\varepsilon}_r\mathbf{s}_x$, where $\mathbf{K}_y$, $\mathbf{u}_z$, $\mathbf{u}_y$, $\boldsymbol{\varepsilon}_r$, and $\mathbf{s}_x$ are defined in (2.9) [41].

$$\mathbf{K}_y = \begin{bmatrix} \tilde{k}_{y,1,1} & & & 0 \\ & \tilde{k}_{y,1,2} & & \\ & & \ddots & \\ 0 & & & \tilde{k}_{y,m,n} \end{bmatrix} \quad \mathbf{u}_z = \begin{bmatrix} U_{z,1,1} \\ U_{z,1,2} \\ \vdots \\ U_{z,m,n} \end{bmatrix} \quad \mathbf{u}_y = \begin{bmatrix} U_{y,1,1} \\ U_{y,1,2} \\ \vdots \\ U_{y,m,n} \end{bmatrix}$$
$$\mathbf{s}_x = \begin{bmatrix} \mathrm{s}_{x,1,1} \\ \mathrm{s}_{x,1,2} \\ \vdots \\ \mathrm{s}_{x,m,n} \end{bmatrix} \quad \varepsilon_r = \begin{bmatrix} \text{Toeplitz} \\ \text{convolution} \\ \text{matrix} \end{bmatrix} \tag{2.9}$$

Applying this format to the remaining equations of (2.7) and (2.8), the semi-analytical form of Maxwell's equations is obtained in linear space. These are given in equation sets (2.10) and (2.11).

$$\begin{aligned} -j\mathbf{K}_y\mathbf{u}_z - \frac{d}{d\tilde{z}}\mathbf{u}_y &= \boldsymbol{\varepsilon}_r\mathbf{s}_x \\ \frac{d}{d\tilde{z}}\mathbf{u}_x + j\mathbf{K}_x\mathbf{u}_z &= \boldsymbol{\varepsilon}_r\mathbf{s}_y \\ \mathbf{K}_x\mathbf{u}_y - \mathbf{K}_y\mathbf{u}_x &= j\boldsymbol{\varepsilon}_r\mathbf{s}_z \end{aligned} \tag{2.10}$$

$$\begin{aligned} -j\mathbf{K}_y\mathbf{s}_z - \frac{d}{d\tilde{z}}\mathbf{s}_y &= \boldsymbol{\mu}_r\mathbf{u}_x \\ \frac{d}{d\tilde{z}}\mathbf{s}_x + j\mathbf{K}_x\mathbf{s}_z &= \boldsymbol{\mu}_r\mathbf{u}_y \\ \mathbf{K}_x\mathbf{s}_y - \mathbf{K}_y\mathbf{s}_x &= j\boldsymbol{\mu}_r\mathbf{u}_z \end{aligned} \tag{2.11}$$

The bottom equations of each equation set can be solved for the z component. The longitudinal components of the field amplitude may be eliminated by substituting the z component into the equation set of the orthogonal field. Doing so leaves four equations and just as many unknowns: unknowns: $\mathbf{u}_x, \mathbf{u}_y, \mathbf{s}_x,$ and $\mathbf{s}_y$. The resulting equations can be written in block matrix form.

$$\frac{d}{d\tilde{z}}\begin{bmatrix}\mathbf{u}_x\\ \mathbf{u}_y\end{bmatrix}=\mathbf{Q}\begin{bmatrix}\mathbf{s}_x\\ \mathbf{s}_y\end{bmatrix},\quad \mathbf{Q}=\begin{bmatrix}\mathbf{K}_x\boldsymbol{\mu}_r^{-1}\mathbf{K}_y & \varepsilon_r-\mathbf{K}_x\boldsymbol{\mu}_r^{-1}\mathbf{K}_x\\ \mathbf{K}_y\boldsymbol{\mu}_r^{-1}\mathbf{K}_y-\varepsilon_r & -\mathbf{K}_y\boldsymbol{\mu}_r^{-1}\mathbf{K}_x\end{bmatrix} \tag{2.12}$$

$$\frac{d}{d\tilde{z}}\begin{bmatrix}\mathbf{s}_x\\ \mathbf{s}_y\end{bmatrix}=\mathbf{P}\begin{bmatrix}\mathbf{u}_x\\ \mathbf{u}_y\end{bmatrix},\quad \mathbf{P}=\begin{bmatrix}\mathbf{K}_x\varepsilon_r^{-1}\mathbf{K}_y & \mu_r-\mathbf{K}_x\varepsilon_r^{-1}\mathbf{K}_x\\ \mathbf{K}_y\varepsilon_r^{-1}\mathbf{K}_y-\mu_r & -\mathbf{K}_y\varepsilon_r^{-1}\mathbf{K}_x\end{bmatrix} \tag{2.13}$$

The left-hand side of (2.13) can be differentiated with respect to *z*, and substituted into the left-hand side of (2.12) to obtain $\frac{d^2}{d\tilde{z}^2}\begin{bmatrix}\mathbf{s}_x\\ \mathbf{s}_y\end{bmatrix}=\mathbf{P}\cdot\frac{d}{d\tilde{z}}\begin{bmatrix}\mathbf{u}_x\\ \mathbf{u}_y\end{bmatrix}\Rightarrow\frac{d^2}{d\tilde{z}^2}\begin{bmatrix}\mathbf{s}_x\\ \mathbf{s}_y\end{bmatrix}=\mathbf{P}\cdot\mathbf{Q}\begin{bmatrix}\mathbf{s}_x\\ \mathbf{s}_y\end{bmatrix}$.

Solving for $\mathbf{PQ}$, the final wave equation is obtained in matrix form, as shown in (2.14) [42].

$$\frac{d^2}{d\tilde{z}^2}\begin{bmatrix}\mathbf{s}_x\\ \mathbf{s}_y\end{bmatrix}-\boldsymbol{\Omega}^2\begin{bmatrix}\mathbf{s}_x\\ \mathbf{s}_y\end{bmatrix}=0,\qquad \boldsymbol{\Omega}^2=\mathbf{PQ} \tag{2.14}$$

Rather than numerically solve this large set of ordinary differential equations, each of these can be solved analytically. The set of solutions is of the form:

$$\begin{bmatrix}\mathbf{s}_x(\tilde{z})\\ \mathbf{s}_y(\tilde{z})\end{bmatrix}=e^{-\boldsymbol{\Omega}\tilde{z}}\mathbf{a}^{+}+e^{\boldsymbol{\Omega}\tilde{z}}\mathbf{a}^{-}, \tag{2.15}$$

where $\mathbf{a}^{+}$ and $\mathbf{a}^{-}$ are column vectors describing the proportionality constants for the differential equation. Their direction of propagation is indicated by their superscripts; forward propagating waves are denoted by +, backward propagating waves by –.

Using the matrix property $f(\mathbf{A})=\mathbf{V}_{\mathbf{A}}f(\lambda_{\mathbf{A}})\cdot\mathbf{V}_{\mathbf{A}}^{-1}$, it is possible to define propagation direction-based exponential terms $e^{\boldsymbol{\Omega}\tilde{z}}$ and $e^{-\boldsymbol{\Omega}\tilde{z}}$ such that $e^{\boldsymbol{\Omega}\tilde{z}}=\mathbf{W}\exp(\boldsymbol{\lambda}\tilde{z})\mathbf{W}^{-1}$ and $e^{-\boldsymbol{\Omega}\tilde{z}}=\mathbf{W}\exp(-\boldsymbol{\lambda}\tilde{z})\mathbf{W}^{-1}$. Here, $\mathbf{A}$ is an arbitrary square matrix of full rank, $\mathbf{V}_{\mathbf{A}}$ is an Eigen-vector calculated from $\mathbf{A}$, $\mathbf{W}$ is an Eigen-vector matrix calculated from $\boldsymbol{\Omega}^2$, and $\lambda_{\mathbf{A}}$

is a diagonal Eigen-value matrix also calculated from $\boldsymbol{\Omega}^2$. Substituting $e^{\boldsymbol{\Omega}\tilde{z}}$ and $e^{-\boldsymbol{\Omega}\tilde{z}}$ into (2.15) and combining the proportionality constants with the Eigen-vector matrix yields:

$$\begin{bmatrix}\mathbf{s}_x(\tilde{z})\\ \mathbf{s}_y(\tilde{z})\end{bmatrix} = \mathbf{W}e^{-\lambda\tilde{z}}\mathbf{c}^+ + \mathbf{W}e^{\lambda\tilde{z}}\mathbf{c}^- \tag{2.16}$$

In a similar manner, a solution may be written for the magnetic fields; this allows the magnetic field Eigen-vector matrix, $\mathbf{V}$, to be calculated from Eigen-value solution of $\boldsymbol{\Omega}^2$. This relationship, shown in (2.17), relates the electric field to the magnetic field Eigen-vectors – knowing one field indicates knowledge of the orthogonal field.

$$\begin{aligned}\frac{d}{dz}\begin{bmatrix}\mathbf{u}_x(\tilde{z})\\ \mathbf{u}_y(\tilde{z})\end{bmatrix} &= \mathbf{V}\boldsymbol{\lambda}e^{-\lambda\tilde{z}}\mathbf{c}^+ + \mathbf{V}\boldsymbol{\lambda}e^{\lambda\tilde{z}}\mathbf{c}^- = \mathbf{Q}\begin{bmatrix}\mathbf{s}_x\\ \mathbf{s}_y\end{bmatrix} = \mathbf{QW}e^{-\lambda\tilde{z}}\mathbf{c}^+ + \mathbf{QW}e^{\lambda\tilde{z}}\mathbf{c}^-,\\ \Rightarrow \mathbf{V}\boldsymbol{\lambda} &= \mathbf{QW} \quad \text{or} \quad \mathbf{V} = \mathbf{QW}\boldsymbol{\lambda}^{-1}.\end{aligned} \tag{2.17}$$

The amplitudes of the plane wave expansion for the electric and magnetic fields can be combined in a single matrix equation (2.18) [43].

$$\begin{aligned}\begin{bmatrix}\mathbf{s}_x(\tilde{z})\\ \mathbf{s}_y(\tilde{z})\end{bmatrix} &= \mathbf{W}e^{-\lambda\tilde{z}}\mathbf{c}^+ + \mathbf{W}e^{\lambda\tilde{z}}\mathbf{c}^-\\ \begin{bmatrix}\mathbf{u}_x(\tilde{z})\\ \mathbf{u}_y(\tilde{z})\end{bmatrix} &= -\mathbf{V}e^{-\lambda\tilde{z}}\mathbf{c}^+ + \mathbf{V}e^{\lambda\tilde{z}}\mathbf{c}^-\end{aligned} \Rightarrow \begin{bmatrix}\mathbf{s}_x(\tilde{z})\\ \mathbf{s}_y(\tilde{z})\\ \mathbf{u}_x(\tilde{z})\\ \mathbf{u}_y(\tilde{z})\end{bmatrix} = \begin{bmatrix}\mathbf{W} & \mathbf{W}\\ -\mathbf{V} & \mathbf{V}\end{bmatrix}\begin{bmatrix}e^{-\lambda\tilde{z}} & 0\\ 0 & e^{\lambda\tilde{z}}\end{bmatrix}\begin{bmatrix}\mathbf{c}^+\\ \mathbf{c}^-\end{bmatrix} \tag{2.18}$$

The fields are determined by $\mathbf{W}$ and $\mathbf{V}$, and the amplitudes are given by $\mathbf{c}$ coefficients. The forward propagation and phase accumulation are described by the Eigen-values. Mode solutions are propagated in both directions in the medium, adhering to the boundary conditions of other modes in adjacent slabs. Scattering matrices are then used to match the tangential components of the fields at the boundaries prior to propagating into the next slab.

At this point, the Redheffer Star Product is used to apply scattering matrices for multiple layers. Due to the product of scattering matrices, the layers of the device are connected to the reflected and transmission region [42]. For a 3 layer device, this can be described by (2.19) and (2.20), where $\mathbf{S}_1$, $\mathbf{S}_2$, and $\mathbf{S}_3$ are scattering matrices of layers 1, 2, and 3 respectively. $\mathbf{S}_{ref}$ and $\mathbf{S}_{trn}$ represent the scattering matrices of the superstrate and substrate.

$$\mathbf{S}_{123} = \mathbf{S}_3 \otimes \mathbf{S}_2 \otimes \mathbf{S}_1 \tag{2.19}$$

$$\mathbf{S}_{global} = \mathbf{S}_{trn} \otimes \mathbf{S}_{123} \otimes \mathbf{S}_{ref} \tag{2.20}$$

The matrices connecting the device to the superstrate and substrate regions are given by the reflection-side and transmission-side scattering matrices, respectively. The full device is then connected. Finally, the transverse components are used to find the longitudinal field components -- diffraction efficiency and power in the diffracted orders is found using equations (2.21) and (2.22) [41].

$$\left|\vec{\mathbf{r}}\right|^2 = \mathbf{r}_x^2 + \mathbf{r}_y^2 + \mathbf{r}_z^2, \quad \mathbf{R} = \mathrm{Re}\left[\frac{\mathbf{K}_{\mathrm{z,ref}}}{k_{\mathrm{z,inc}}}\right] \cdot \left|\vec{\mathbf{r}}\right|^2, \quad R = \sum \mathbf{R} \tag{2.21}$$

$$\left|\vec{\mathbf{t}}\right|^2 = \mathbf{t}_x^2 + \mathbf{t}_y^2 + \mathbf{t}_z^2, \quad \mathbf{T} = \mathrm{Re}\left[\frac{\mathbf{K}_{\mathrm{z,ref}}}{k_{\mathrm{z,inc}}} \frac{\mu_{\mathrm{ref}}}{\mu_{\mathrm{trn}}}\right] \cdot \left|\vec{\mathbf{t}}\right|^2, \quad T = \sum \mathbf{T} \tag{2.22}$$

2.3 Particle Swarm Optimization

Using RCWA, the spectral response from an optical device may be calculated as a function of some parameter. Ultimately, the spectral response is based on the device geometry; for complex devices, there are many fabrication parameters to optimize. For

this reason, additional routines have been developed to optimize the structural parameters of a device to yield the desired spectral output prior to device fabrication. Conventional optimization routines include iterative and heuristic methods; this section specifically concentrates on heuristic methods, with an emphasis placed on particle swarm optimization (PSO).

Conventional heuristic optimization routines include mimetic algorithms (MA), differential evolution (DE), genetic algorithms (GA), particle swarm optimization (PSO), and simulated annealing (SA). Of these, MA, DE and GA are evolution-based algorithms, creating solutions to optimization problems based on the evolution of an original solution. Alternatively, SA and PSO are based on solution comparison. As a solution space is examined, SA monitors a decreasing probability of accepting poor solutions, while PSO compares all solutions across the space and iteratively moves individual particles towards a best global result before re-comparing new results.

Introduced as a concept for optimizing nonlinear functions, PSO is a method for finding a best overall solution in a multivariable space [44], [45]. Compared with genetic algorithms, particle swarm optimization has fewer parameters and has better stability and global convergence for solving intricate problems [46]. Since the spectral response of a photonic device is intimately related to its structural parameters, restrictions on one can lead to severely restrict the other. Within the space of device fabrication, the number of variables is used in a point-by-point search of a ‘best solution’. This can be costly in terms of time and resources. Instead, particle swarm optimization may be used to simulate many variations of the structural parameters to determine the best possible

design within the fabrication window. For a typical design, fabrication parameters include lateral period, duty cycle, grating height, grating geometry (hexagonal or linear), refractive index, angle of incidence and wavelength; these parameters alone give rise to a 7-dimensional process space.

Functionally, a 'swarm' is initialized; each particle placed at random locations across the process space with a unique set of structural parameters used during simulation. The particles are incrementally simulated, building a set of measurements for the particle swarm. However, the solution space is often populated with many "local best" solutions – the task of PSO is to find the best solution globally. Without having *a priori* knowledge of the solution, this can become difficult. To alleviate this, a merit function is used to judge which solution best meets the application criteria. In addition, the merit function can be maximized or minimized to provide a better solution set. The merit function resembles $M(p_1, p_2) = A(p_1, p_2)$, where p_1 and p_2 are the device parameters, and A is a feature of the spectral response (ex. diffraction efficiency).

With respect to the full process space, the optimized solution may lie in a confined region leading to a narrow solution space and restricted tolerances in fabrication. For this reason, it may be necessary to increase bandwidth of the solution, offering robustness to the design. Other parameters may also be incorporated in the merit function to meet requirements of the application. However, the parameters may not be equally important in the merit function; these can be properly scaled using logarithms or exponentials to emphasize large design changes. In this case, the merit function is the product of the appropriately weighted variables: $M(p_1, p_2) = A(p_1, p_2) \bullet \log\left[B(p_1, p_2)\right]$.

A comparison of all merit function results yields a global best for the current set of simulations. The swarm is updated, changing only the velocity of the particles; particle position is a function of a change in time and velocity. The velocity $\left(v_i^{k+1}\right)$ and position $\left(x_i^{k+1}\right)$ are described by equation (2.23) [47].

$$v_i^{k+1} = wv_i^k + cr_1^k(p_g^k - x_i^k) + sr_2^k(p_i^k - x_i^k)$$
$$x_i^{k+1} = x_i^k + \chi v_i^{k+1},\ \vec{\chi}_i = \begin{bmatrix} d_1 \\ d_2 \\ \varepsilon_2 \end{bmatrix} \tag{2.23}$$

An inertia and cognitive term are represented by wv_i^k and $cr_1^k(p_g^k - x_i^k)$, respectively; x_i^k is the position of the particle that is being updated; since all particles share information about their best solution, this term gives the tendency for the particle to move towards a local term. The "self" term, $sr_2^k(p_i^k - x_i^k)$, describes the particle's motion near the solution. The randomness coefficient r_2^k tends to make the particle wander in a circle in lieu of turning around and heading back toward the global solution. This allows more solutions to be covered. The constriction term, χ, ensures a maximum velocity of the particles.

Together, applying an optimization routine like PSO to an RCWA routine results in a very powerful tool. The ability to explore an N-dimensional space in a time-efficient manner for a given device geometry can greatly decrease the time needed to serially explore the same product space, while simultaneously ensuring an optimized solution. Implementation of the RCWA and PSO routines described above will be exemplified in both broadband spectral reflectors and narrowband resonant reflectors.

2.4 Example 1 - Broadband Spectral Reflectors

As previously stated, the DBR stack acts as a one dimensional photonic crystal; each of the layers has a thickness of $\lambda_0/4n\cos\theta_i$, where λ_0 is the wavelength in free space, n is the refractive index of the layer, and θ_i is the angle of incidence on the layer. Known as a "quarter-wave stack", this geometry provides high reflectivity centered on λ_0. As described in (2.24), the reflectance coefficient, *r*, is a function of the layer parameters [48].

$$r = \frac{n_1 n_3^{2m} - n_4 n_2^{2m}}{n_1 n_3^{2m} + n_4 n_2^{2m}} \tag{2.24}$$

Substituting $\varepsilon = n^2$ in (2.24), equation (2.25) is obtained.

$$r = \frac{\left(\varepsilon_1 \varepsilon_3^{2m}\right)^2 - \left(\varepsilon_4 \varepsilon_2^{2m}\right)^2}{\left(\varepsilon_1 \varepsilon_3^{2m}\right)^2 + \left(\varepsilon_4 \varepsilon_2^{2m}\right)^2},\ R = |r|^2 \tag{2.25}$$

Here, *m* is the number of layer pairs, and R is the reflectance. The electric permittivities of the surrounding medium and substrate are given by ε_1 and ε_4, while the permittivity of the alternating layers are represented by ε_2 and ε_3. A typical DBR geometry is shown in Fig. 2.1.

Upon interaction with the successive layers, light will reflect off of each interface and interfere constructively. As an example, alternating layers of silicon dioxide (SiO_2) and silicon nitride (Si_3N_4) can achieve >98% reflection with as few as 3 layer pairs around $\lambda_0 = 1550$ nm. While the high reflectivity component in the laser cavity should ideally demonstrate 100% reflectivity, a laser's output power peaks when the reflectivity

of the out-coupler component is ~80% [49]. For a large number of layer pairs, a strong broadband reflectivity can be found. The reflectivity versus wavelength for 10 layer pairs is shown on the right hand side in Fig. 2.1, with input values of $\varepsilon_1 = 1.0$, $\varepsilon_2 = 2.1237$, $\varepsilon_3 = 3.7959$, and $\varepsilon_4 = 2.0846$. The reflectance profile was obtained via RCWA to check the closed-form analysis.

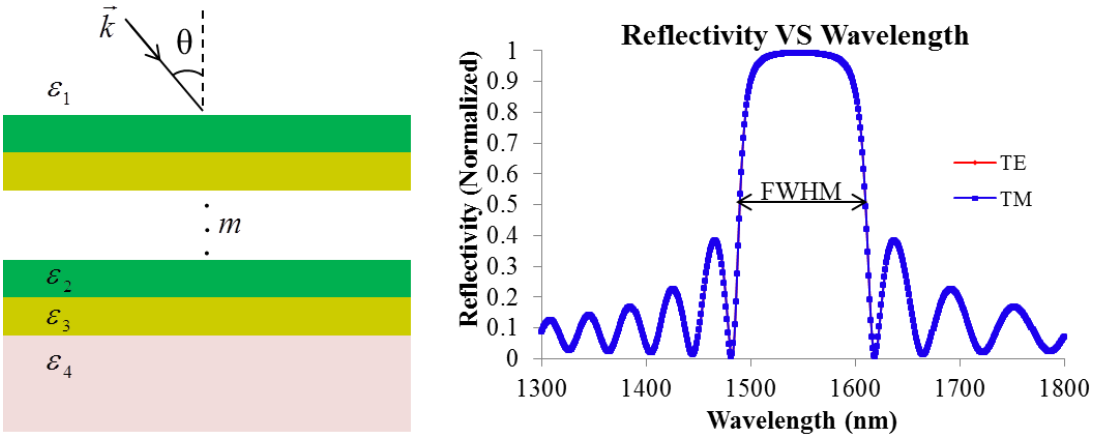

Fig. 2.1. (Left) A multilayer Distributed Bragg Reflector geometry is shown. (Right) A plot of reflectivity versus wavelength is shown for a 10 layer pair structure.

DBR devices are also used for providing strong cavity feedback, but there are limitations introduced by the periodic geometry. One disadvantage is the highly reflective sidebands on both sides of the stop-band region; in Fig. 2.1, the sidebands reach ~40% reflectivity. Furthermore, DBR mirrors typically work at close-to-normal angles of incidence. To mitigate this, recent studies have employed unconventional deposition techniques to design a geometry operable at angles up to $\theta_i = 70°$ [50]. Still, strong sidebands persist. Lastly, fabrication of the device is limited by strict requirements placed on the coating thickness and material availability due to tolerances in the deposition process. Any change in the thickness or electric permittivity of a layer will arise as a

difference in the optical path length through the layer. In turn, this affects the phase delay and constructive interference ultimately changing the spectral performance.

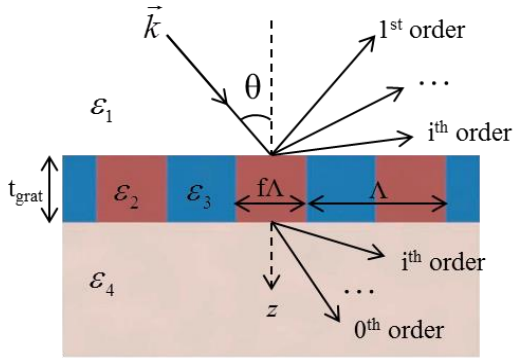

Fig. 2.2 A single layer waveguide grating geometry is shown.

Alternatively, linear grating geometries (Fig. 2.2) can provide strong broadband reflectance as well. Mathematically, the fields inside the grating structure can be represented by Helmholtz equations. For homogenous materials, (2.26) is obtained. In its general form, it is represented by equation (2.27) [36].

$$\frac{\partial^2}{\partial x^2}U(x,z)+\frac{\partial^2}{\partial z^2}U(x,z)+\left(\varepsilon_L^2 k_0\right)^2 U(x,z)=0 \tag{2.26}$$

$$\frac{\partial^2}{\partial z^2}G_m(z)+t_m^2 G_m(z)=0 \tag{2.27}$$

In these equations, $U(x,z)$ represents the incident electric field with horizontal (X) and vertical (Z) components, ε_L is the permittivity of layer L ($L=1$ for the superstrate, $L=2$ for the grating region, and $L=3$ for the substrate) and k_0 is the wave vector of the incident field. $G_m(z)$ represents the general form of the solution of equation (2.27), and represents the Fourier coefficients of the reflected field.

$$G_m(z)=T_m\exp\left[it_m(z-h)\right]+R_m\exp\left[-it_m(z-h)\right]. \tag{2.28}$$

T_m and R_m represent the complex amplitude of the transmitted and reflected diffraction orders in the superstrate and substrate; h represents the height of the grating, and t_m represents the transmission coefficient where $t_m^2 = (kn_m)^2 - a_m^2$. The tangential component of the phase for the 0^{th} and m^{th} reflected diffracted orders are given by α_0 and α_m, respectively, as defined in equation (2.29).

$$\alpha_0 = k\varepsilon_1^2 \sin\theta, \qquad \alpha_m = \alpha_0 + \frac{2\pi m}{\Lambda} \tag{2.29}$$

In the superstrate region, the reflected field becomes a superposition of the incident field and the reflected fields, U_{inc} and U_R. The incident and reflected fields are defined in equations (2.30) and (2.31).

$$U_{inc}(x,z) = \exp\left[ik\varepsilon_1^2\left(x\sin\theta_i + z\cos\theta_i\right)\right] \tag{2.30}$$

$$U_R(x,z) = G(x,z)\exp\left(-i\alpha_0 x\right) \tag{2.31}$$

Since the G(x,z) is periodic, it can be expressed as a Fourier series, with Fourier coefficients $G_m(z)$. Since the transmitted and reflected fields are of similar form, they can be rewritten as the summation of (2.32) and (2.33).

$$U_R(x,z) = \sum_{m=-\infty}^{+\infty} R_m \exp\left[i\left(\alpha_m x + r_m z\right)\right] \tag{2.32}$$

$$U_T(x,z) = \sum_{m=-\infty}^{+\infty} T_m \exp\left\{i\left[\alpha_m x + t_m(z-h)\right]\right\} \tag{2.33}$$

In dielectric materials, real-valued reflection and transmission coefficients represent propagating waves; imaginary values correspond to energy in evanescent orders, propagating along the interface.

The grating equation (2.34) describes the relationship between the wavelength of the incident light, λ_0, the angle of incidence, θ_i, and the grating parameters ($\varepsilon_1, \varepsilon_{L=2}, \Lambda$). This relationship determines the angles into which the various diffracted orders are divided after interacting with the grating.

$$\varepsilon_{L=2}^2 \sin\theta_m = \varepsilon_1^2 \sin\theta_i + m\lambda_0/\Lambda \tag{2.34}$$

While *m* is an integer, the other variables may be non-integer values. Solving for the diffraction angle of various orders yields (2.35).

$$\theta_m = \sin^{-1}\left(\frac{\varepsilon_1^2 \sin\theta_i + m\lambda_0/\Lambda}{\varepsilon_{L=2}^2}\right) \tag{2.35}$$

To consider a numerical example, the grating geometry shown in Fig. 2.2 is considered. With a superstrate and substrate of air and fused silica $(\varepsilon_1 = 1.000,\ \varepsilon_4 = 2.084)$, light of wavelength $\lambda_0 = 1.55$ μm is normally incident $(\theta_i = 0°)$ on the grating with lateral period $\Lambda = 2.0$ μm. The grating is further characterized by the ratio of the grating pillar width to the lateral period, called the duty cycle; in this case, the grating pillar width was half of the lateral period. In this case, $\lambda_0 < \Lambda$, and real values of θ_i occur for $m = -1, 0, +1$. Specifically, the angles of diffraction are: $\theta_{-1} = -1.8803°$, $\theta_0 = 0.000°$ and $\theta_{+1} = +1.8803°$. The diffraction conditions change when λ_0 becomes comparable to Λ. In the case where $\lambda_0 = \Lambda$, the same diffracted orders exist, but the angles of diffraction are greater $(\theta_{-1} = -2.542°,\ \theta_0 = 0.000°,\ \theta_{+1} = 2.542°)$.

However, when $\lambda_0 > \Lambda$ all non-zero diffractive orders become evanescent, and only the $m = 0$ order is allowed to propagate in the device. At this point, the alternating

materials in the one dimensional grating region can be described by an effective index [39], [51]. For more complex grating geometries, methods for estimating an effective index have also been found [52], [53]. An explanation of the effect of the grating's depth has also been proposed for both 1-D and 2-D geometries [54]. If the effective permittivity exceeds that of the surrounding superstrate and substrate, diffracted waves can become guided along the grating, causing the region to act as a leaky waveguide. The change in amplitude of the propagating wave in the waveguide is characterized by a propagation constant, β_m, and the associated propagation coefficient of the leaky mode, β [55]. These are given in equations (2.36) and (2.37).

$$\beta_m = k\left(\varepsilon_{L=2}^2 \sin\theta_i - m\lambda_0/\Lambda\right) \tag{2.36}$$

$$\beta = \beta_m + i\xi \tag{2.37}$$

Associated with the loss of the leaky mode, ξ is determined for the resonance wavelength, λ_0. In the special case when a resonance is associated with a single leaky mode, the spectral location of the resonance can be used to find the full-width at half-maximum, where Γ is the loss of the leaky mode as determined at the resonance wavelength, given by (2.38) [55].

$$\Delta\lambda_{FWHM} = \lambda_0\Lambda\Gamma/\pi. \tag{2.38}$$

When the propagation constant of the wave in the leaky waveguide matches that of the evanescent waves, strong coupling is achieved. Phase matching between the incident and leaky field is produced by the grating, allowing the external waves to couple into guided modes confined to the waveguide. The waveguide is considered "leaky" in

that the grating allows light to 'leak' out of the waveguide and couple strongly with the incident field. This effect, identified as "guided-mode resonance", gives rise to a narrowband resonance for materials with low permittivity contrast. The spectral response is ideal for fabricating narrowband spectral filters known as Guided-Mode Resonance Filters (GMRFs) [35]. Based on the total internal reflection of the propagating guided waves and the necessary phase matching condition produced by the grating, an eigenvalue equation can be obtained for TE and TM polarizations as shown in equations (2.39) and (2.40). The variables κ, γ, and δ are defined as follows: $\kappa_i = \left(\varepsilon_g k^2 - \beta_i^2\right)^{1/2}$, $\gamma_i = \left(\beta_i^2 - \varepsilon_1 k^2\right)^{1/2}$, and $\delta_i = \left(\beta_i^2 - \varepsilon_3 k^2\right)^{1/2}$.

$$\tan\left(\kappa_i d\right) = \frac{\kappa_i\left(\gamma_i + \delta_i\right)}{\kappa_i^2 - \gamma_i\delta_i} \tag{2.39}$$

$$\tan\left(\kappa_i d\right) = \frac{\varepsilon_g\kappa_i\left(\varepsilon_3\gamma_i + \varepsilon_1\delta_i\right)}{\varepsilon_1\varepsilon_3\kappa_i^2 - \varepsilon_g^2\gamma_i\delta_i} \tag{2.40}$$

These equations are transcendental, and must be solved numerically. The solutions yield the resonance wavelength for the appropriate polarization, but reveal no information regarding the amplitude, linewidth, or symmetry of the resonance. Aside from the role of the propagation constant and wave vector, it is important to note that the relative permittivity of the materials plays an important role in the spectral response of the device. As shown in Fig. 2.3, broadband resonance was demonstrated using RCWA for the geometry illustrated in Fig. 2.2.

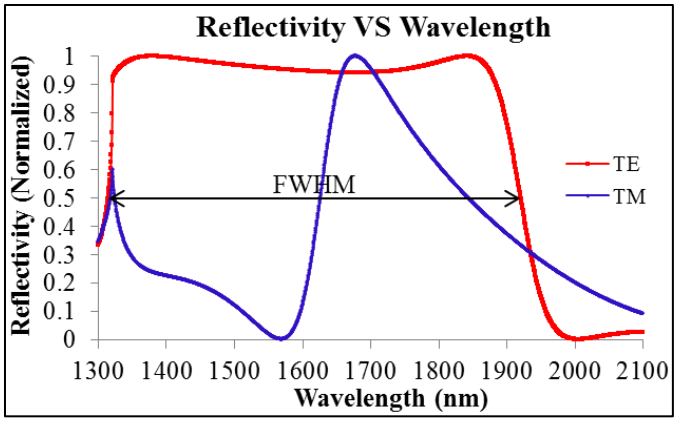

Fig. 2.3. A plot of reflectivity versus wavelength is shown for a broadband resonant structure.

The superstrate and substrate are represented by $\varepsilon_1 = 1.000$ and $\varepsilon_4 = 2.079,$ while the alternating materials in the grating region are given by $\varepsilon_2 = 3.960$ and $\varepsilon_3 = 11.179.$ The superstrate and substrate are considered to be semi-infinite and homogenous. The grating has a period of $\Lambda = 916$ nm and thickness $t_{grat} = 417.87$ nm. Incident light is polarized parallel to the grating grooves, or "TE" polarization. The TE spectral response demonstrates a 605 nm full-width at half-maximum (FWHM) while the TM response shows strong reflectivity only around 1700 nm. The device parameters were similar to those found in recent literature reporting broadband GMR structures [56].

2.5 Example 2 - Narrowband Spectral Reflectors

In a similar manner, the materials that make up the grating region can be chosen such that low index contrast is used. In doing so, equations (2.39) and (2.40) may be solved numerically to obtain narrowband resonance solutions. These can be plotted to show the resonance regime for both polarizations of a given device geometry as shown in Fig. 2.4. The simulated device's geometry is similar to that presented in Fig. 2.2, but with different

material parameters. In the case of a narrowband resonance filter, the superstrate and substrate are air $(\varepsilon_1 = 1.00)$ and fused silica $(\varepsilon_4 = 2.079)$, respectively. Alternating materials in the grating region have permittivities $\varepsilon_2 = 2.439$ and $\varepsilon_3 = 3.084$. The grating parameters are $\Lambda = 1012$ nm, $h = 787.5$ nm, $f = 64\%$, at normal incidence $(\theta_i = 0°)$.

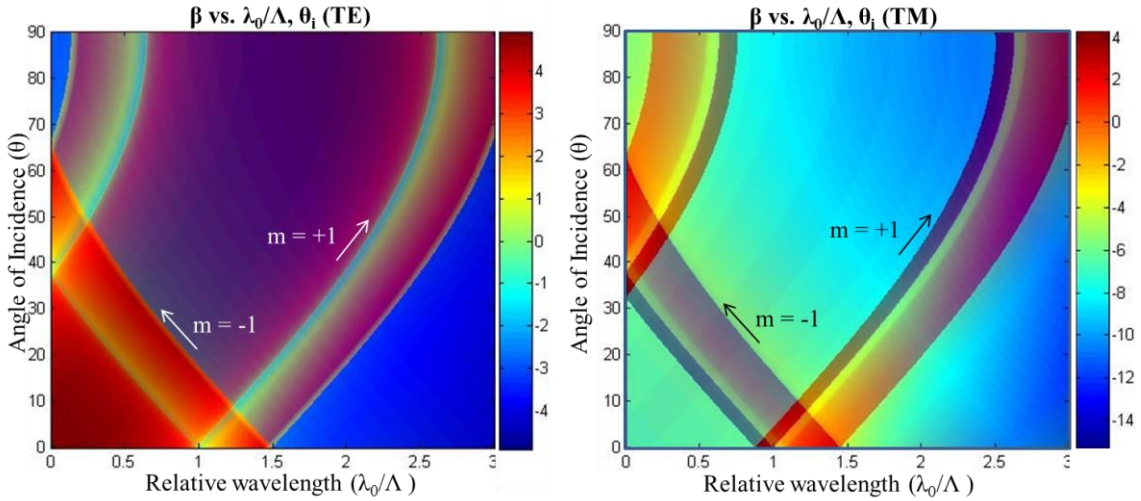

Fig. 2.4. Numerical solutions to the transcendental equations are a plotted for TE (left) and TM (right) polarizations. Color is indicative of the value of the propagation constant; relative magnitude is shown to the right of the plot.

In both plots, the propagation constants are calculated. The positive values of β satisfy the propagation requirement necessary for a resonance to occur. The groups are represented by swooping regions of red, orange, and yellow. The left edge of each swooping curve represents the diffraction limit inherent in the grating, while the right edge represents the propagation limit for the diffracted wave inside the grating region. Resonances caused by the $m = \pm 1$ diffracted orders are labeled by arrows. The spectral split indicates that a single resonance at normal incidence will split into two resonances at larger angles of incidence, θ_i. Using RCWA to simulate the resonance profile, Fig. 2.5 is obtained. The simulation parameters are the same as those used in Fig. 2.3.

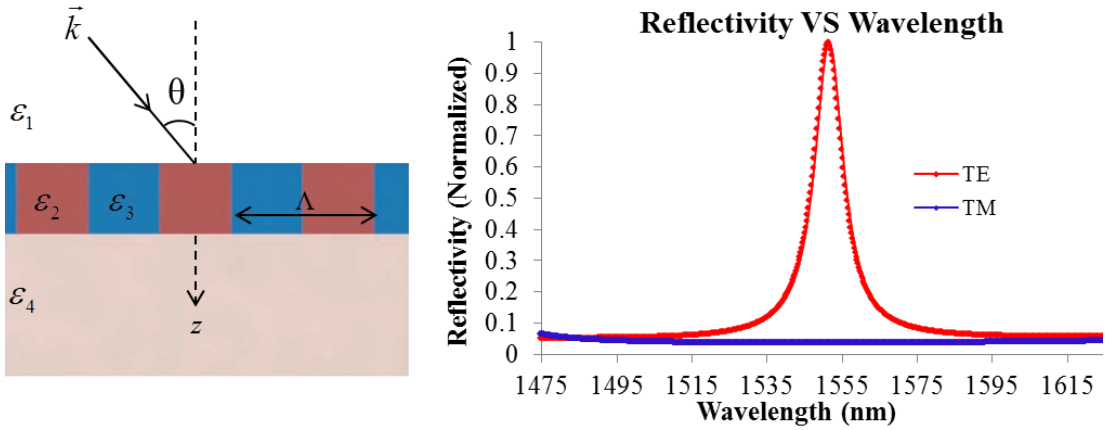

Fig. 2.5. (Left) A sample device profile is illustrated for a narrowband waveguide-grating GMRF. (Right) The spectral response of the illustrated device is shown.

While the index contrast between materials in the grating region have been briefly discussed, it is helpful to have an intuitive understanding of how altering design parameters changes the spectral response of the resonant device. The reflectivity can be simulated as both a function of wavelength and a GMRF fabrication parameter. As shown in Fig. 2.8 – Fig. 2.12 examine changes in period (Λ), grating height (T_{grat}), duty cycle (f·Λ), and refractive index (ε^2) are considered. These parameters are indicated in Fig. 2.6. The specific fabrication parameters are listed in the inset of each figure, and the color bar to the right of each plot represents the magnitude of the reflectivity for a given data point. Fig. 2.7 illustrates the basic polarization-dependent resonance response upon which all subsequent simulations are based.

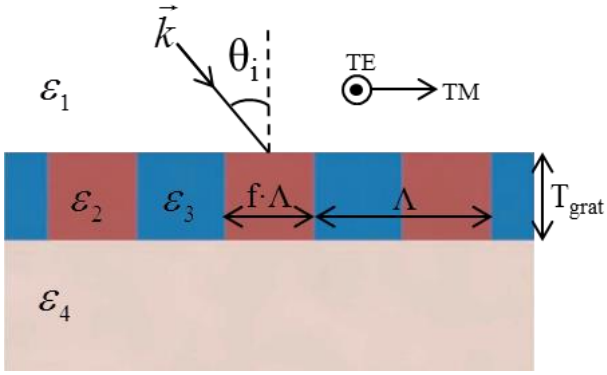

Fig. 2.6. Refractive index profile for the ideal waveguide grating geometry.

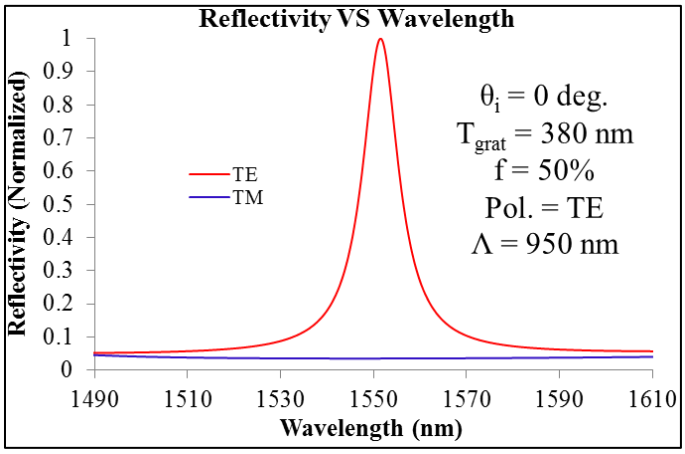

Fig. 2.7. Reflectivity is simulated versus wavelength for the ideal waveguide grating geometry.

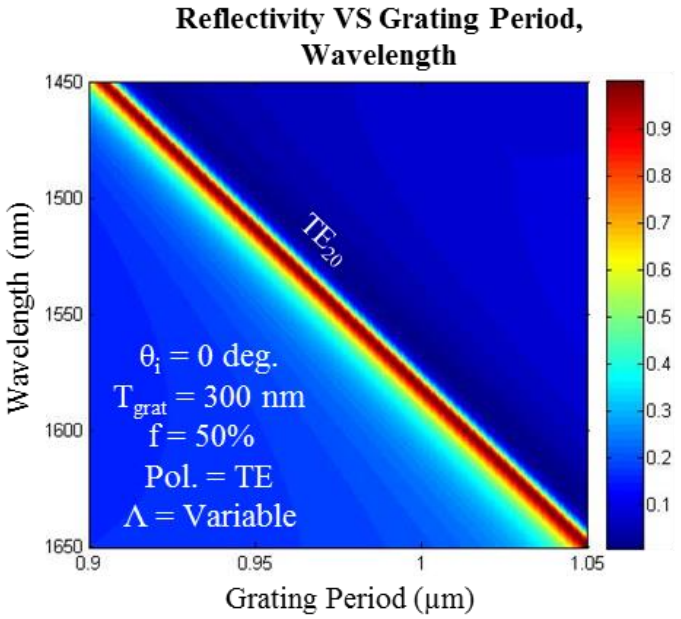

Fig. 2.8. Reflectivity is simulated versus wavelength as a function of lateral grating period for the ideal waveguide grating geometry. Incident radiation is TE polarized.

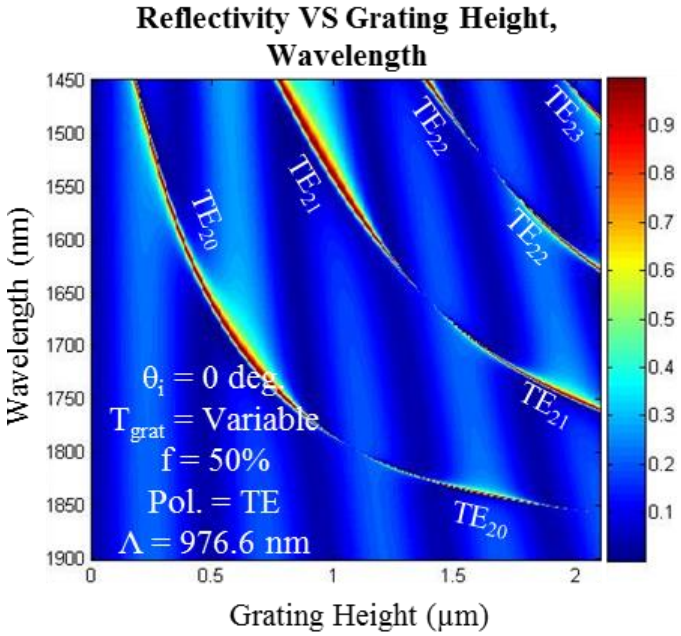

Fig. 2.9. Reflectivity is simulated versus wavelength as a function of grating height for the ideal waveguide grating geometry. Incident radiation is TE polarized.

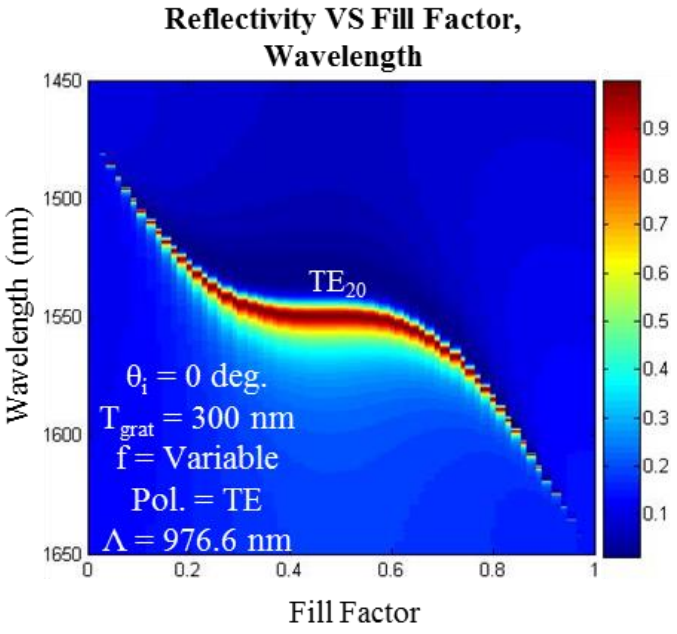

Fig. 2.10. Reflectivity is simulated versus wavelength as a function of fill factor for the ideal waveguide grating geometry. Incident radiation is TE polarized.

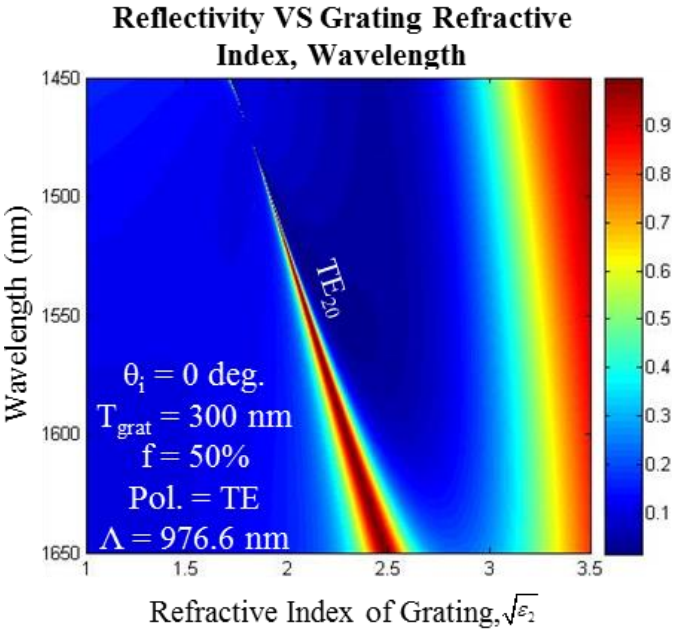

Fig. 2.11. Reflectivity is simulated versus wavelength as a function of grating refractive index for the ideal waveguide grating geometry. Incident radiation is TE polarized.

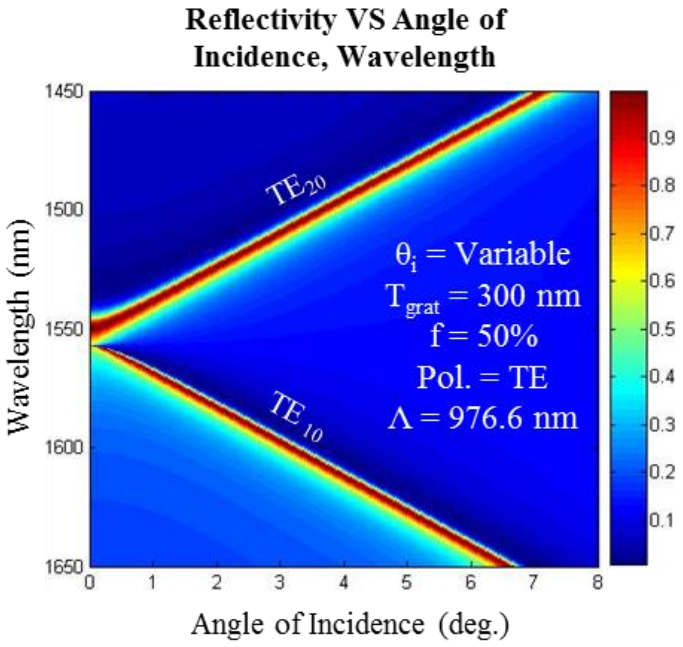

Fig. 2.12. Reflectivity is simulated versus wavelength as a function of angle of incidence for the ideal waveguide grating geometry. Incident radiation is TE polarized.

In Fig. 2.8, reflectivity is simulated as a function of wavelength and grating period. As the period of the grating increases, the position of the resonance red-shifts linearly at a rate of ~13.7 nm for every 10 nm the period is increased. The linear relationship comes as no surprise; from equation (2.40), it can be seen that Λ is embedded in β, which is present in each κ, γ, and δ term.

In contrast, variation in the height of the grating (Fig. 2.9) does not have a linear effect on the resonance location; this is also somewhat intuitive, since the grating thickness T_{grat} arises as the argument of a tangent in (2.40). Due to the geometry of the device, decreasing the height of the grating also decreases the thickness of the waveguide. As the grating height decreases to 0, a guided mode cannot be sustained, and the resonance is lost. Along with a slight redshift in the resonance location, increased

grating thicknesses are able to sustain higher order modes in the waveguide. These manifest as additional resonant lines in the figure.

Fig. 2.10 illustrates the effect of variation in the duty cycle; the resonance can be seen to become non-existent as the fill factor of the grating becomes 0 or 1. This makes sense, as these represent the cases where the waveguide-grating consists of one material. At this point, the grating acts as a simple thin-film providing low reflectivity of the incoming light, based on Fresnel's equations:

$$\begin{aligned} r_{TE} &= \frac{n_1\cos(\theta_i) - n_2\cos(\theta_t)}{n_1\cos(\theta_i) + n_2\cos(\theta_t)} \quad t_{TE} = \frac{2n_1\cos(\theta_i)}{n_1\cos(\theta_i) + n_2\cos(\theta_t)} \\ r_{TM} &= \frac{n_2\cos(\theta_i) - n_1\cos(\theta_t)}{n_1\cos(\theta_t) + n_2\cos(\theta_i)} \quad t_{TM} = \frac{2n_1\cos(\theta_i)}{n_1\cos(\theta_t) + n_2\cos(\theta_i)} \end{aligned}, \tag{2.41}$$

where θ_t transmission angle is obtained via Snell's Law, $n_i \sin\theta_i = n_t \sin\theta_t$. Furthermore, the most stable regime for the resonance appears to be when the fill factor is between 40 – 60% of the grating period. The refractive index of a specific layer is related to that layer's electric permittivity by equation (2.42).

$$n_i = \sqrt{\varepsilon_i} \tag{2.42}$$

As the refractive index of the grating region changes, the profile of the resonance is seen to change dramatically (Fig. 2.11). At low refractive indices, the index contrast between the materials that comprise the waveguide-grating is too low to sustain a guided mode. Practically, a finite number of materials are available during fabrication limiting the available index contrast. As the refractive index of one material increases, the index contrast increases. When the index contrast is ~1, the waveguide grating acts as a thin

film. However, when the index is greater than 1, guided-modes can exist in the waveguide and produce a resonance. As the index contrast increases, the resonance red-shifts and widens. In extreme cases, this can lead to broadband resonances, seen in Fig. 2.3.

Lastly, the change in reflectivity as a function of angle of incidence is illustrated in Fig. 2.12. As the angle of incidence increases, the resonance is seen to split into two spectrally separated resonances, each deviating linearly from the initial spectral location at normal incidence. Depending on the geometry, GMRFs can be extremely sensitive to the angle of incidence; for the simulated device, the resonance separates at ~0.25°. With such small tolerances, this can make some GMRF devices difficult to align experimentally, and caution and patience must be exercised.

Similar trends in the reflectivity apply equally to broadband and narrowband GMRFs as parameters of the fabrication are varied. Experimentally, variations in the fabrication process will become more apparent for the narrowband structures. Henceforth, the analysis will focus on narrowband resonant structures.

In the conventional design, the grating layer remains exposed. Since this is an integral part of the design, an inverted resonant structure was conceived in order to maintain a narrowband resonance and protect the grating layer. Chapter two will discuss the motivation, process space, fabrication, and subsequent experimental results of the inverted monolithic resonant filters.

While the design of the inverted resonant structures protects the grating layer and provides a homogenous resonant structure, the waveguide layer remains vulnerable to the

surrounding atmosphere. Chapter three demonstrates a design to encapsulate the waveguide and grating, simultaneously protecting them both using a waveguide grating geometry. A thick cladding layer can then added for protection. To alleviate a prolonged deposition, chemical-free direct wafer bonding was utilized, allowing the waveguide grating to become encapsulated between a 0.5 mm fused silica and the 1.0 mm thick substrate.

2.6 Example 3 – Inverted Broadband Spectral Reflectors

For the previous examples, the resonant devices geometries were optimized for high reflection for the $m = 0$ diffraction order. Based on the grating equation (2-34), it is known that under proper conditions, higher diffractive orders can exist within a resonant device. The tangential phase component of the diffracted orders are given by equation (2-43), where α_0 is the tangential component of the 0^{th} order phase, k is the wave vector, and n_I is the refractive index of the region of interest. The diffractive order number is given by m, and Λ is the period of the grating.

$$\alpha_m = \alpha_0 + \frac{2\pi m}{\Lambda}, \quad \alpha_0 = k n_I \sin\theta \tag{2-43}$$

From this relationship, it can be concluded that the $m = 0$ order has no effect on the phase of the reflected signal. This is not the case with higher order, nonzero diffraction orders. At $m = 0$, the left term reduces to α_0, since the numerator of the second term goes to zero. When $m \neq 0$, the phase of the reflected signal can be incrementally altered by $2\pi/\Lambda$.

Using this information, a device was to be designed that offered simultaneous control over the amplitude and phase of the reflected signal. An inverted grating design was chosen similar to previous studies [57]. The results of this study are shown below for comparison in Fig. 2.13.

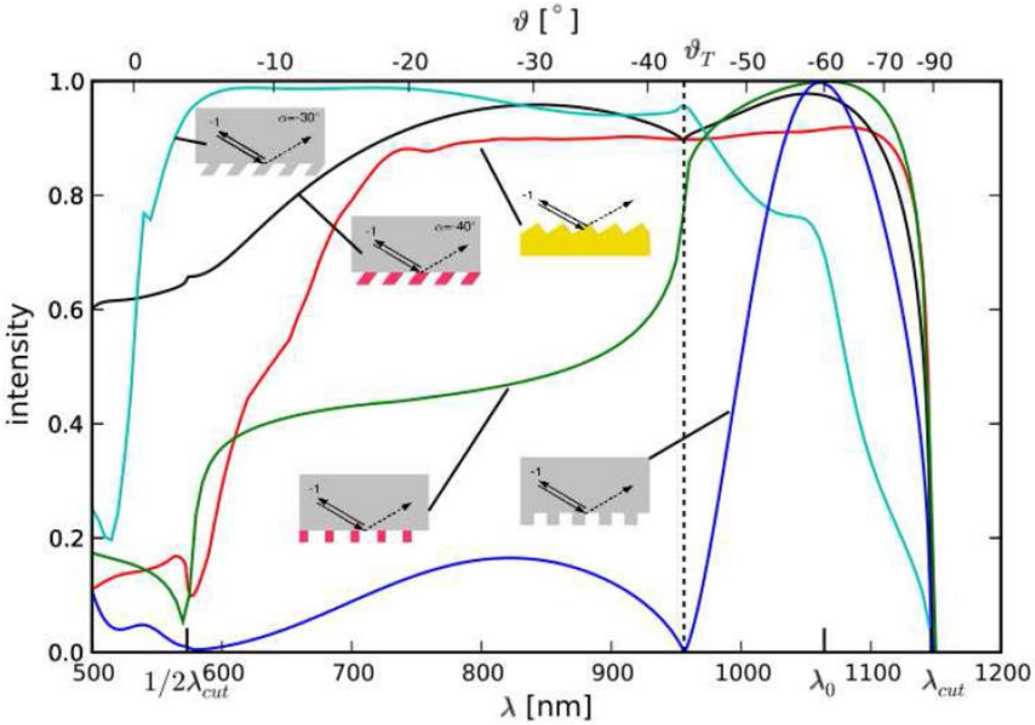

Fig. 2.13. Intensity is plotted versus wavelength for six device geometries. [57]

With the exception of the blazed grating, all other inverted grating geometries exhibit high reflectivity over a wide spectral band. Of the devices shown, the largest spectral band showing greater than 90% reflectivity is from the single-material linear grating with the tilted grooves.

The device geometry seen in Fig. 2.14 is based on a seven-parameter fabrication space: substrate refractive index (ε_2), deposition refractive index (ε_3), grating period (Λ),

grating ridge width $\left(f \cdot \Lambda \right)$, grating thickness $\left(T_{grat} \right)$, top planar layer thickness $\left(T_{wg} \right)$, and angle of incidence $\left(\theta_i \right)$. The design is further complicated by the restraint to optimize reflection in the $m = -1$ order; since this is not the primary diffractive order for guided-mode resonance devices, the device response is less intuitive. Based on the optimized geometry, conformal deposition could be used and the fabrication procedure is simplified, since a slanted grating geometry is not required. To further illustrate the effectiveness of the optimization routine, the spectral response of a non-optimized geometry is shown in the left image of Fig. 2.15.

Given that multivariable parameters space, a PSO routine was used in conjunction with RCWA to obtain a broadband reflection centered around $\lambda_{inc} = 2300$ *nm.* After the ideal parameters are found, the process space can be mapped to examine tolerances surrounding the fabrication process. The ideal device geometry is shown in Fig. 2.13.

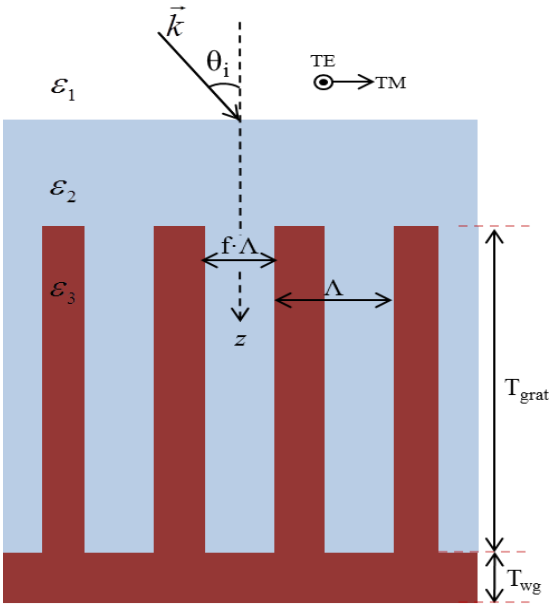

Fig. 2.14. Ideal refractive index profile for the inverted broadband geometry.

The linear grating has a lateral period and ridge width of $\Lambda = 950$ nm and $f \cdot \Lambda = 407$ nm, respectively, and is conformally filled with hafnium oxide (HfO_2) The grating pillars and planar top layer have thicknesses of $T_{grat} = 2.973\ \mu m$ and $T_{wg} = 489\ nm$. At 60 degrees angle of incidence, more than 90% of TE polarized light is reflected over a 290 nm band. This reflectivity is based on a resonance caused by the $m = -1$ diffracted order. Polarization dependence is seen upon comparison of the TE and TM spectral response.

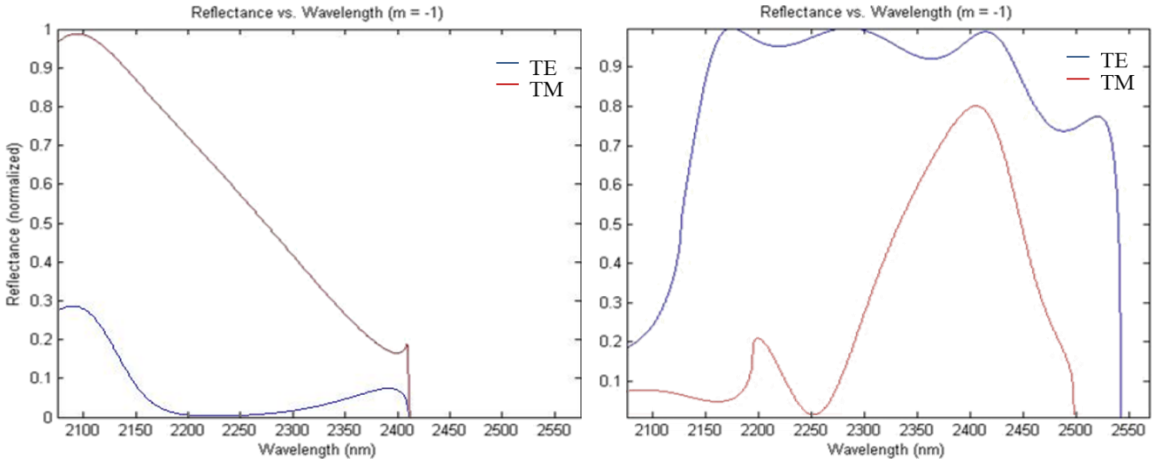

Fig. 2.15. Reflectance is plotted against wavelength for the m = -1 diffracted order for TE and TM polarizations using (left) an unoptimized structure, and (right) an optimized structure.

As seen in the right image of Fig. 2.15, the spectral response of the TE polarization is greater than 90% over a band of 290 nm. While this is less than the devices previously mentioned, it provides the ability to utilize standard lithography techniques to obtain a similar response while enabling control over the reflected phase profile.

2.7 Conclusion

As shown in the previous examples, a variety of outcoupler geometries can be designed based on application requirements. However, the spectral response of the device is a function of the coupled device parameters. Since the spectral response of an ideal resonant geometry cannot be analytically derived, computational routines must be used to understand the device behavior for a set of conditions. In this work, an RCWA routine was used to analyze the geometries needed for a variety of applications.

To quickly analyze and reach an optimized parameter set, PSO was utilized. This allowed for a quick search and optimization of the design's multi-dimensional process space. By carefully tailoring the merit function of the optimization routine, the specified response could be reached.

CHAPTER THREE

INVERTED MONOLITHIC RESONANT FILTERS

3.1 Introduction

Highly reflective, narrowband mirrors are important to the stability and narrow linewidth produced by mid- to high-power laser systems. As a solution, Distributed Bragg Reflector (DBR) multilayer stacks are often used. However, their fabrication relies heavily on multiple coatings that must be matched in refractive index and thickness to achieve proper phase retardation of the reflected beams. Additionally, DBR stacks cannot work effectively at large angles of incidence. Furthermore, the use of multiple materials can cause a differential thermal expansion between each layer, resulting in mechanical stress and strain within the device. For thick coating stacks, this may cause unwanted delamination or cracking.

Alternatively, guided-mode resonance filters (GMRFs) may be used to provide narrowband reflection at the desired wavelength. The first GMRF devices utilized a waveguide-grating geometry, demonstrating a versatile, tunable design that could maintain strong narrowband reflection [35]. Subsequent GMRF geometry designs have separated the two layers, placing the grating on top of the waveguide to act as a diffractive element [32], [58]. While the mechanics of the resonance remain the same, the separation allows the waveguide to become protected from the environment, but this leaves the grating vulnerable to external damage and contamination. Moreover, altering

the grating layer will modify its diffractive properties, affecting the resonance condition and resonance profile.

In an effort to protect the grating, an 'inverted' GMRF geometry was designed [59], [60]. By placing the waveguide on top of the grating layer, the grating layer is protected from damage. While this places the waveguide on top of the etched structure, the fabrication method allows for a single-material, monolithic resonant structure to be fabricated. In doing so, the thermal mismatch between different materials is removed leading to a more stable resonant device in mid- to high-power laser systems. Similar to the conventional GMRF design, a definitive index contrast is needed between the waveguide, grating, and subsequent layers in order to trap and propagate the diffracted light. Unlike the conventional designs, light incident on the inverted device will transmit through the waveguide and encounter the grating with a wavelength shifted by $\lambda' = \lambda_0 / n_{wg}$. Here, λ_0 is the incident wavelength in vacuum and n_{wg} is the refractive index of the waveguide. Upon reaching the grating, transmitted diffractive orders pass through the grating while the reflected orders will diffract into the waveguide, causing a resonance to occur at the proper conditions. Polarization dependence of the device can be eliminated by implementing a hexagonal grating geometry in place of the original linear grating geometry [61].

3.2 Design and Process Space (Linear Grating)

To develop a fabrication design, rigorous coupled-wave analysis (RCWA) was used to simulate and explore the process space. To understand how the device design fit

within the window of fabrication and experimental tolerances, reflectivity was simulated as a function of wavelength and various design parameters. This was first done for the case of an ideal structure – a slab waveguide resting on a binary grating. The simulation results are illustrated in Fig. 3.1 - Fig. 3.8. In Fig. 3.3 – Fig. 3.8, the resonant modes within the simulation are identified by TE_{ij} modes. This represents a TE mode profile in the waveguide, characterized by *i* vertical divisions and *j* horizontal divisions of the mode intensity distribution.

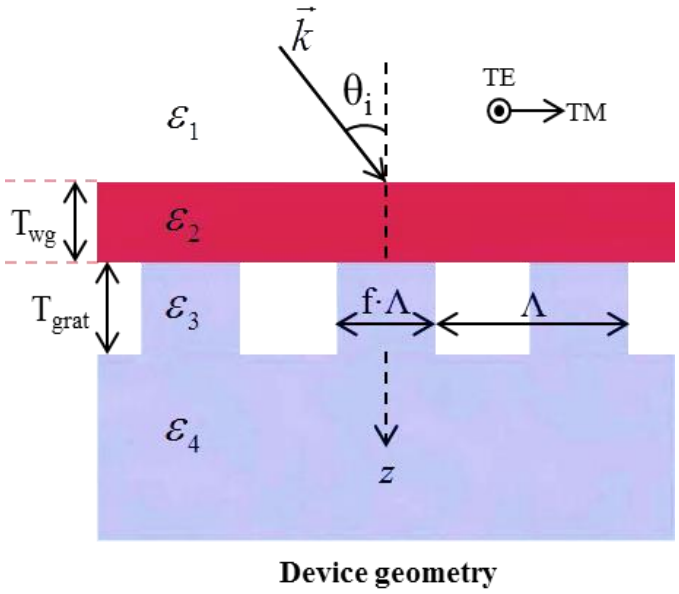

Fig. 3.1. Ideal refractive index profile for the inverted linear grating geometry.

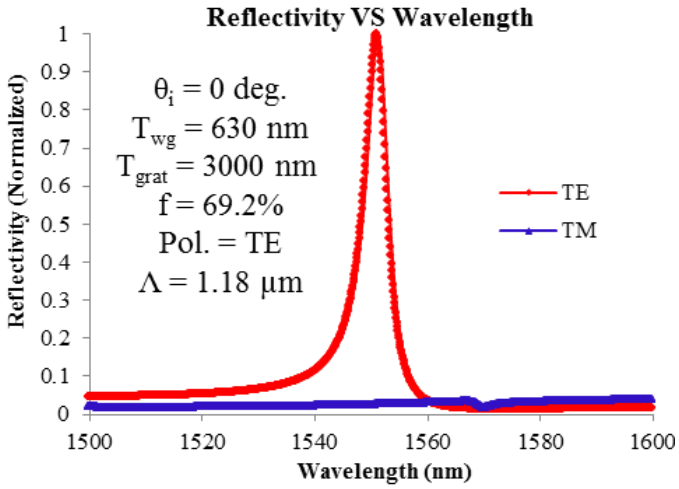

Fig. 3.2. Reflectivity is simulated versus wavelength for the ideal inverted linear grating geometry.

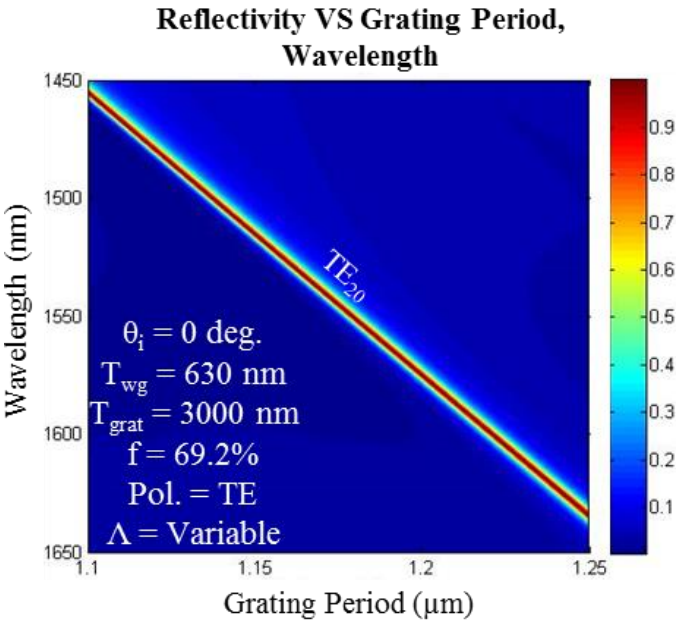

Fig. 3.3. Reflectivity is simulated versus wavelength as a function of lateral grating period for the ideal inverted linear grating geometry. Incident radiation is TE polarized.

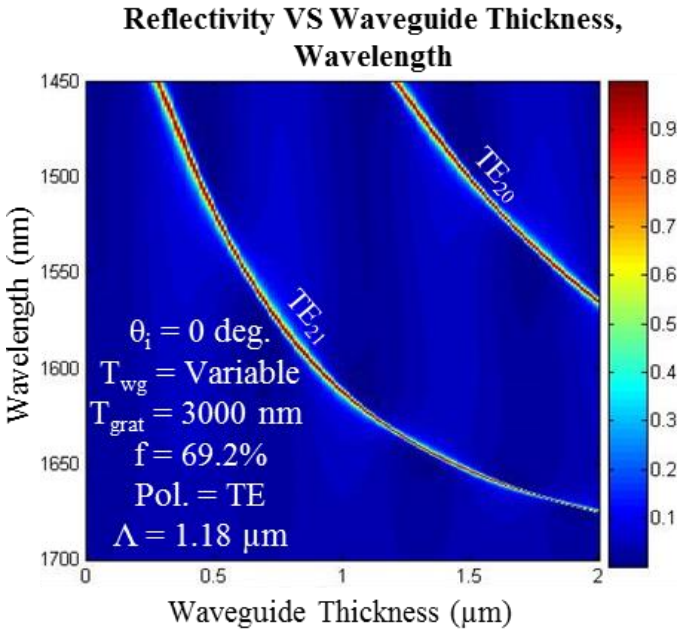

Fig. 3.4. Reflectivity is simulated versus wavelength as a function of waveguide thickness for the ideal inverted linear grating geometry. Incident radiation is TE polarized.

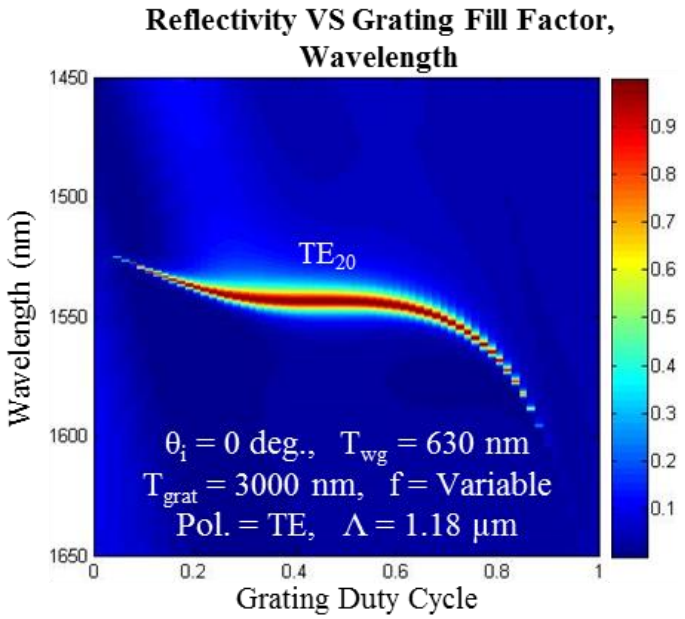

Fig. 3.5. Reflectivity is simulated versus wavelength as a function of fill factor for the ideal inverted linear grating geometry. Incident radiation is TE polarized.

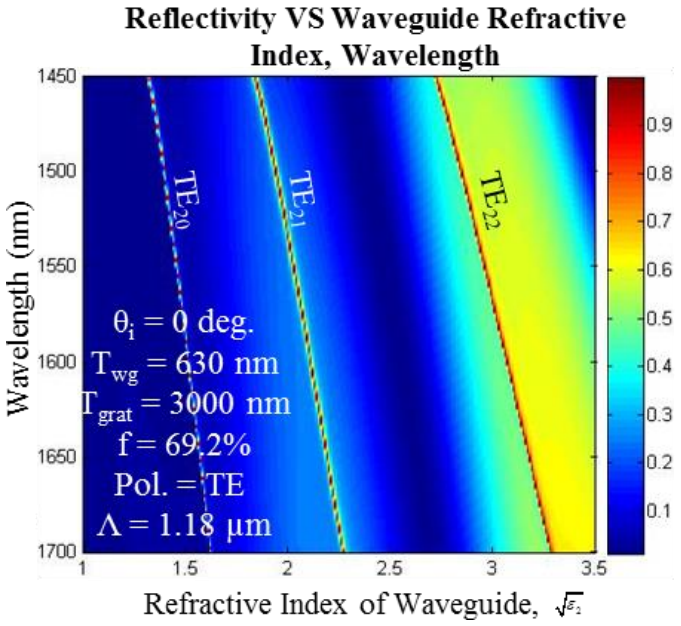

Fig. 3.6. Reflectivity is simulated versus wavelength as a function of waveguide refractive index for the ideal inverted linear grating geometry. Incident radiation is TE polarized.

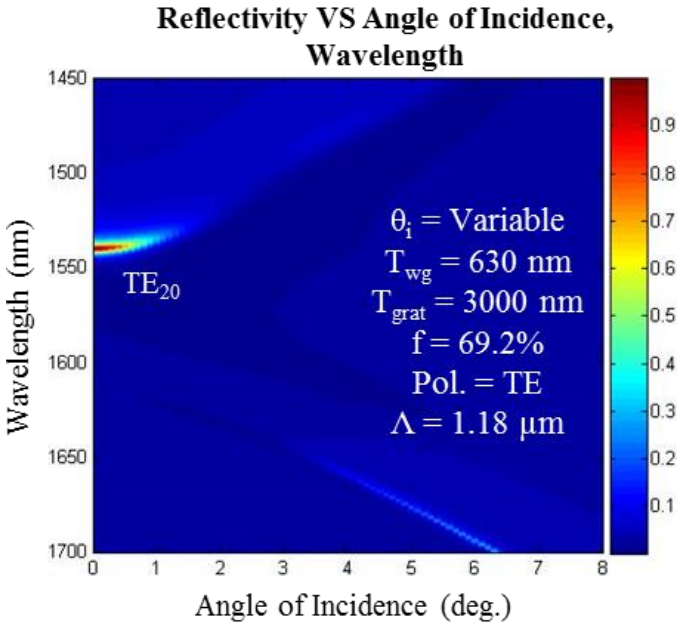

Fig. 3.7. Reflectivity is simulated versus wavelength as a function of angle of incidence for the ideal inverted linear grating geometry. Incident radiation is TE polarized.

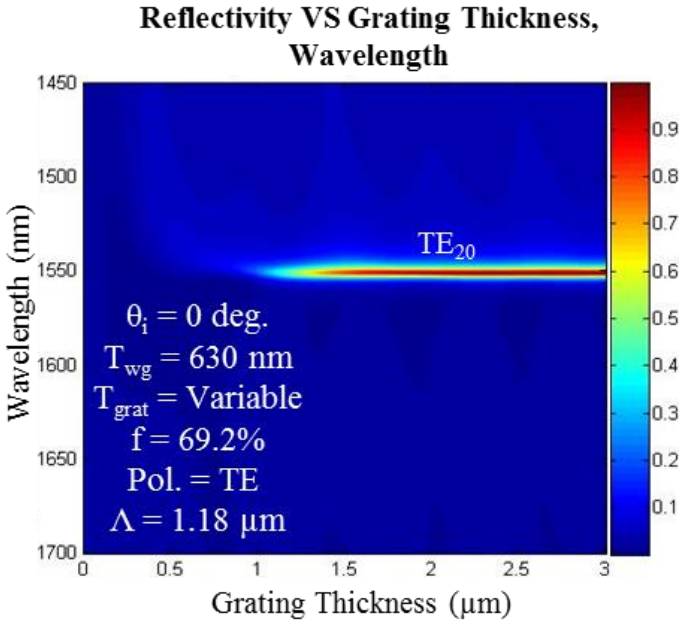

Fig. 3.8. Reflectivity is simulated versus wavelength as a function of grating thickness for the ideal inverted linear grating geometry. Incident radiation is TE polarized.

The trends for each variable strongly resemble that of the waveguide-grating as previously discussed. As the lateral period of the grating increases (Fig. 3.3), the resonance wavelength linearly red-shifts at a rate of 11.94 nm for every increment of $\Delta\Lambda = 10$ nm, and the line-width of the resonance is maintained.

As the height of the waveguide is increased (Fig. 3.4), the location of the resonance red-shifts non-linearly. At large waveguide thicknesses, additional resonances occur, corresponding to higher-order propagation modes in the waveguide. For example, a 1.5 μm-thick waveguide will have resonances at 1501.3 nm and 1654 nm, corresponding to the TE_{20} and TE_{21} modes respectively.

Variation in the grating's fill factor (Fig. 3.5) has a similar effect for the inverted GMRF as seen with the conventional design. The inverted waveguide can provide lower sideband reflectivity, but this can be overcome in the conventional design by depositing

additional layers to suppress non-resonant reflection. Antireflection (AR) coatings would be an example of such a coating. Additionally, the resonance location appears to be more stable for the inverted GMRF at lower duty cycles, maintaining a fairly constant spectral resonance position over 15% more of the duty cycle when compared to the conventional design using the waveguide-grating.

Alternatively, a change in the permittivity of the waveguide creates a stark difference between the response of the waveguide-grating and inverted GMRF. For the case of the waveguide-grating, the resonance broadens as the permittivity contrast between the grating and non-grating materials increase. In the waveguide-grating geometry, a resonance cannot be sustained when $\varepsilon_2 = \varepsilon_3$, since the effective permittivity of the waveguide must be larger than that of the surrounding media. For the inverted structure, the media surrounding the waveguide are vacuum $(\varepsilon_1 = 1.00)$ and the effective index of the grating beneath it. Since the non-grating material is also air, the effective permittivity of the grating region is lower than that of the substrate material, and also lower than the permittivity of the waveguide. This allows a resonance to be sustained in the waveguide as long as proper index conditions are met. As the permittivity of the waveguide is increased, the permittivity contrast of the waveguide increases compared to the surrounding materials. Aside from the slight red-shift, this leads to a broadened resonance (larger FWHM) as previously noted. The additional increase in the off-resonant reflectivity is based on Fresnel reflection. Fig. 3.6 presents reflectivity versus wavelength as a function of the refractive index of the waveguide.

This plot may be misleading in that it appears as if a resonance cannot be obtained at specific values of the waveguide permittivity. In reality, the resonance location continues to redshift with increasing permittivity. The second and third resonance lines refer to the TE_{21} and TE_{22} modes.

With respect to the angular tolerance (Fig. 3.7), the inverted geometry appears to yield a more stable resonance, since the spectral location does not shift over a tilt of ~1 degree. Unlike the resonance of the waveguide-grating, the resonance then blue-shifts instead of splitting into two separate, spectrally shifted peaks. However, weak resonances do occur at higher angles of incidence (> 5 deg.) as expected. This resonance shifts at a rate of 17.6 nm/deg., and resembles the TE_{10} mode. For parameter and consistency in window size, these lie outside the range of the simulation.

The thickness of the grating layer (Fig. 3.8) is shown to play a minor role in the stability of the resonance, as no strong resonances are predicted for gratings shorter than 1.5 μm thick. This is partly due to the interaction between the guided wave and the top of the substrate, ε_4.

3.3 Fabrication Process (Linear Grating)

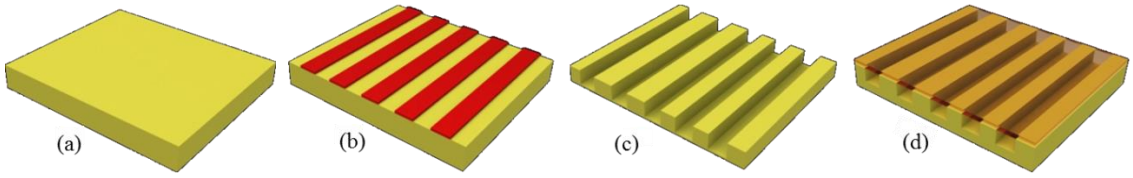

Fig. 3.9. The fabrication process for the inverted linear GMRF design is illustrated.

The device fabrication process begins with cleaned, optically polished UV grade fused silica substrates. The substrates are immersed in Surpass 3000 [62], promoting adhesion of the photoresist to the surface of the substrate (Fig. 3.9a). Shipley 1805 photoresist [63] was subsequently coated on the substrate. Following a post-applied bake step, a GCA g-line 5X reduction stepper tool was used to expose the linear grating pattern (Fig. 3.9b). Development of the photoresist included a post-exposure bake and immersion in MF-319 liquid developer [64].

Using the patterned photoresist as a soft etch mask, a Unaxis Versaline inductively-coupled plasma (ICP) reactive-ion etcher (RIE) was used to transfer the pattern 1.05 µm into the substrate, as shown in Fig. 3.9c. During the etch process, 70 sccm of CHF_3 and 2 sccm of O_2 were used, demonstrating an etch rate of 260 nm/min in fused silica, and 140 nm/min in photoresist. The waveguide was deposited using a high-frequency plasma-enhanced chemical-vapor deposition (PECVD) as shown in Fig. 3.9d. The deposition utilizes 30 W of RF power, 1420 sccm of N_2O, and 400 sccm of 2% silane (SiH_4) to produce a 50 nm/min deposition rate of SiO_x.

Following fabrication, cross-section scanning-electron microscope (SEM) images were taken, illustrating the success of the fabrication process and allowing the fabricated

device to be imaged. Furthermore, the SEM data can be directly imported into an RCWA routine, providing a precise permittivity profile for comparative simulations. These simulations can then be used to quickly and accurately explore the process space of the fabricated device. A comparison of the fabricated structure and modified simulation is shown in Fig. 3.10.

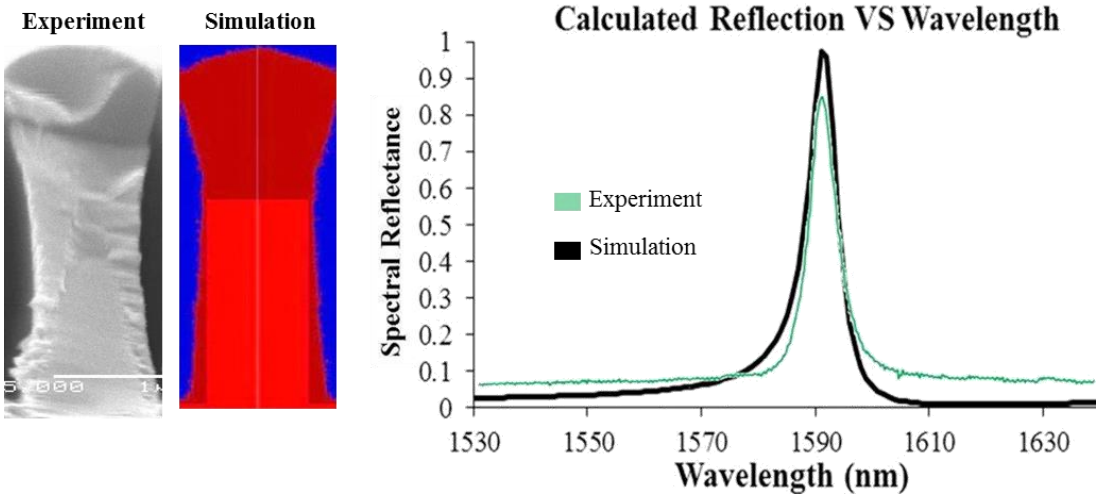

Fig. 3.10. (Left) Cross-section SEM of the fabricated device. (Middle) The cross-section imported as a material profile for simulations. (Right) Overlapped plots of reflection versus wavelength for the SEM imported simulation and experiment.

From Fig. 3.10, the experimental profile is significantly different than the ideal case shown in Fig. 3.1. The non-conformal nature of the PECVD process deposits more material on the top and bottom surfaces of the binary grating than on the sidewalls of the grating. This causes shoulders to form on the top edges of grating surface. As the deposition continues, the shoulders continue to grow outwards towards the shoulders forming on the adjacent pillars. When the shoulders meet, an air void is pinched off, entrapping a pocket of air between the waveguide deposition, the etched grating walls, and the top of the substrate. The trapped air pockets form the (lower) effective index needed to sustain a resonance in the deposited waveguide. The air pocket formation is

illustrated in Fig. 3.11, and is an expected consequence of the deposition technique. Techniques for simulating the deposition process have included level set [65]–[69] and string method [41] algorithms.

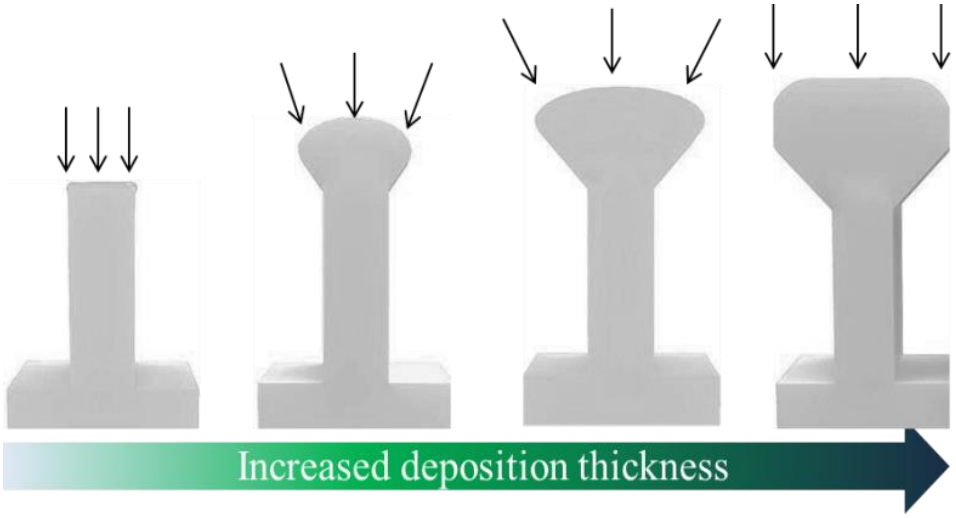

Fig. 3.11. The formation of the air pockets during PECVD deposition is illustrated.

Another difference between the ideal and fabricated profiles concerns the bottom of the grating. As illustrated in Fig. 3.11, the bottom of the grating ridges should remain sharp [70], whereas the SEM profile in Fig. 3.10 depicts pointed edges. This arises from the initial grating profile. Post fabrication, it was discovered that the etched grating had a triangular profile. This caused the air hole to pinch at the bottom of the grating, similar to the top of the air void. Even though the simulation in Fig. 3.10 is based on a rectangular grating, the permittivity of the grating and deposition are close enough that the difference between grating profiles does not make a noticeable difference in the reflected spectra. However, understanding is gained from the ability to simulate the fabricated devices, and exploring the devices' process space. Simulation results are shown in Fig. 3.12 – 3.17

with a format similar to that of the ideal inverted linear structure. In Fig. 3.14 – 3.17, incident radiation has TE polarization.

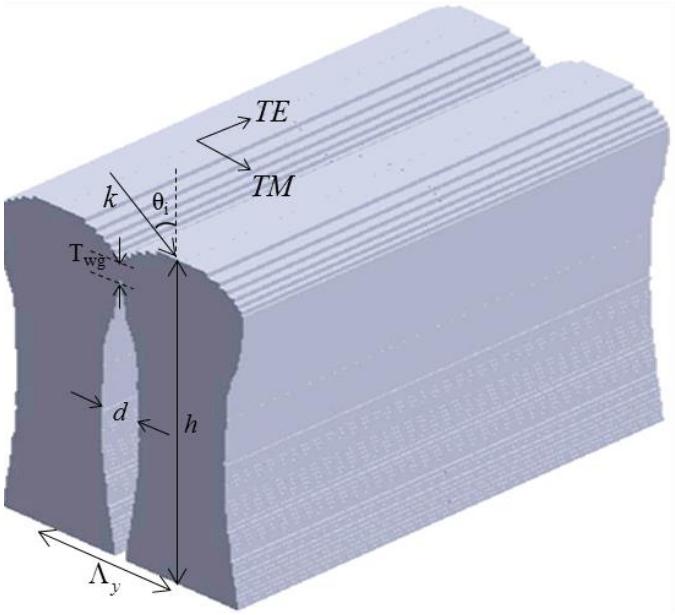

Fig. 3.12. Three-dimensional reconstruction of the refractive index profile used to explore the process space.

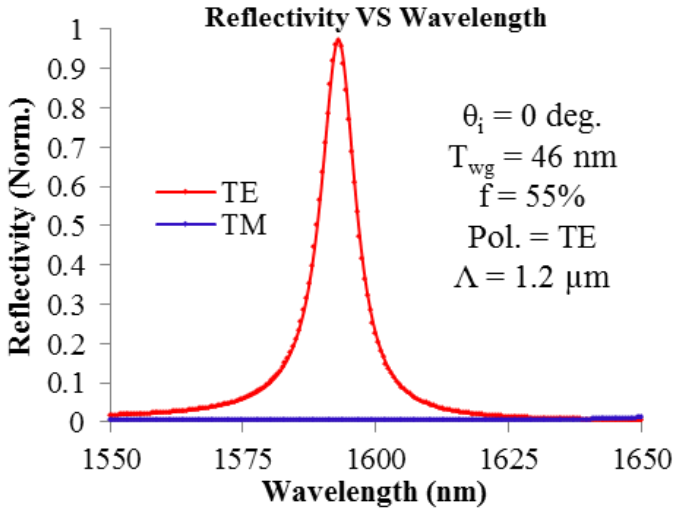

Fig. 3.13. Reflectivity is simulated versus wavelength for the fabricated inverted linear grating geometry.

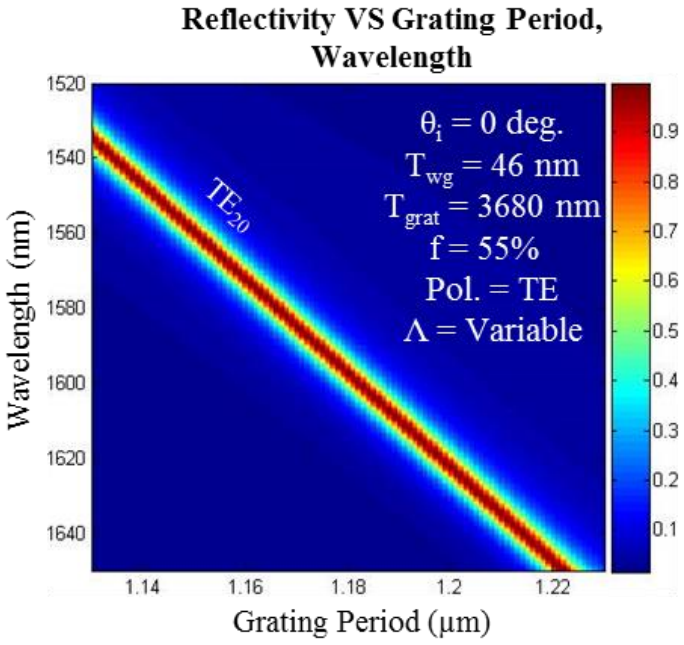

Fig. 3.14. Reflectivity is simulated versus wavelength as a function of lateral grating period for the fabricated inverted linear grating geometry.

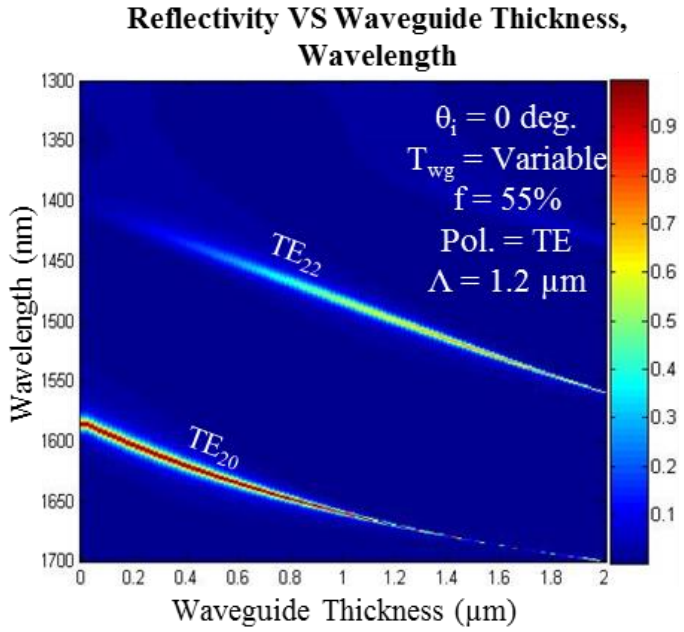

Fig. 3.15. Reflectivity is simulated versus wavelength as a function of waveguide thickness for the fabricated inverted linear grating geometry.

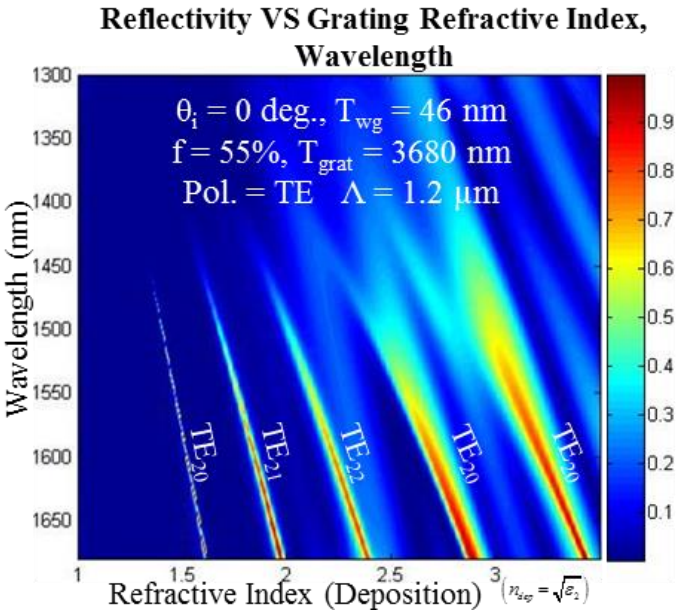

Fig. 3.16. Reflectivity is simulated versus wavelength as a function of waveguide refractive index for the fabricated inverted linear grating geometry.

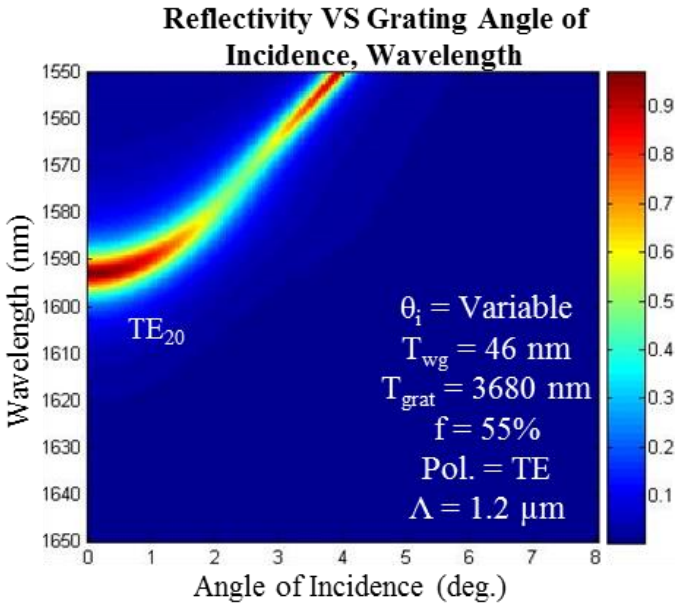

Fig. 3.17. Reflectivity is simulated versus wavelength as a function of the source's angle of incidence on the fabricated inverted linear grating geometry.

In comparison to the ideal structure, many of the same trends are seen in the modified profile. All simulations are performed in TE polarization, since no appreciable resonance is seen in TM in the spectral window of interest (Fig. 3.13). As the grating period increases, the spectral location of the resonance shifts 12.5 nm for every 10 nm the lateral period is increased (Fig. 3.14).

Furthermore, an increase in the thickness of the waveguide, T_{wg}, leads to an asymptotic redshift in the resonance location. Closer inspection of Fig. 3.15 suggests that a resonance may still exist when the thickness of the waveguide is zero. This result is due to the non-ideal simulated geometry of the device. Since the encapsulation of air holes is based on the shoulder formation (Fig. 3.11), diffracted waves may still be weakly guided outside of the region T_{wg}, due to the effective index surrounding the non-porous layers. As the T_{wg} increases, additional modes are able to propagate within the waveguide, each corresponding to a different propagating mode. For instance, a waveguide thickness of ~1000 nm allows the TE_{20} and TE_{22} modes to propagate at 1660 nm and 1483 nm, respectively.

Additionally, the permittivity of the deposition material may be altered. In doing so, higher order propagation modes are allowed to propagate. As the permittivity increases, the resonance red-shifts; further increasing the permittivity allows different modes to propagate at higher orders, or at different places within the GMRF structure. For illustration purposes, the reflectivity was plotted against wavelength and the refractive index of the deposition, n_{dep} (Fig. 3.16). Simulations predict that for refractive indices lower than $n_{dep} = 1.36$, no resonance is obtained in the inverted structure for the

other fabrication parameters. This is due to the low index contrast between the waveguide and grating region. At n_{dep} = 1.36, a weak resonance occurs at 1468 nm. As n_{dep} increases, the TE_{20} mode redshifts at a rate of 84.8 nm for $\Delta n_{dep} = 0.1$. At n_{dep} = 1.6, the TE_{21} begins propagating in the top of the structure. As n_{dep} continues to increase, the TE_{21} mode redshifts at a rate of 63.9 nm for each increase of $\Delta n_{dep} = 0.1$. Continuing in this manner, the TE_{22} mode begins propagating at $n_{dep} = 1.91$, and continues to red-shift at a rate of 47.4 nm for each increase of $\Delta n_{dep} = 0.1$.

Beyond this point, the refractive index of the deposition is high enough to allow propagation in other regions of the inverted structure. Around $n_{dep} = 2.5$, a TE_{20} mode begins to propagate in the bottom of the structure; the effective index at the bottom of the grating/deposition region is strong enough to support a guided mode. Similarly, around $n_{dep} = 2.8$, the TE_{20} mode is able to propagate in the central region of the pillars. As a general trend, as the refractive index of the deposition coating increases, the linewidth of the resonance also increases [60], as shown in Fig. 3.16; furthermore, off-resonance reflection increases as well, based on Fresnel reflection from the surface.

Finally, the reflectivity was simulated as a function of wavelength and angle of incidence, θ_i. Unlike conventional GMRFs, an increase in θ_i does not split the resonance. Instead, the (TE_{20}) resonance blue shifts as illustrated in Fig. 3.17. In the linear region, the resonance blue shifts at a rate of 14.7 nm for every increase of $\Delta\theta_i = 1°$. With a thorough understanding of each variable's impact in the resonance condition, changes can

be made to the device geometry or experiment to alter the resonance profile for any desired application.

3.4 Design and Process Space (Hexagonal Grating)

As shown in Fig. 3.13, resonant devices based on a linear grating geometry will exhibit strong polarization dependence. Therefore, maximum reflectance will be achieved when the incident source is completely polarized along the designed axis of operation of the device. Phenomenologically, it has been shown that a polarization-independent filter may be obtained by employing a two-dimensional grating, symmetrical along the X and Y axes. Since the new unit cell is invariant under a rotation of $90°$ a linearly polarized source will produce strong reflectivity for polarization angles of both φ and $\varphi+90°$ [71]. Similarly, other symmetric grating geometries can be used that are invariant over $180°/n$. One example of this is a hexagonal grating, which is invariant under $60°$ rotations and allows posts or holes to have a greater packing density compared to a square grating.

Similar to the analysis of the inverted linear grating, the devices' process space can be mapped by simulating reflectivity as a function of the fabrication parameters. Similar to the analysis of the linear device, these include grating period, waveguide thickness, hole radius, waveguide refractive index, angle of incidence, and grating thickness.

Due to the symmetry of the hexagonal grating, three fundamental diffraction planes exist, allowing the device to support both TE and TM guided waves [72].

Furthermore, it is possible to obtain a TE and TM resonance for a single wavelength. For a conventional GMRF, this is done by changing the devices' structural parameters to produce a resonance at a known location for the orthogonal polarization [73]. The resonances may then be described by the TE and TM mode profiles along both axes as illustrated in Fig. 3.18. The overlayed resonance profile shows a TE_{10} along X and a TM_{20} mode along Y. The mode inside the full waveguide will then be a hybrid of the two modes.

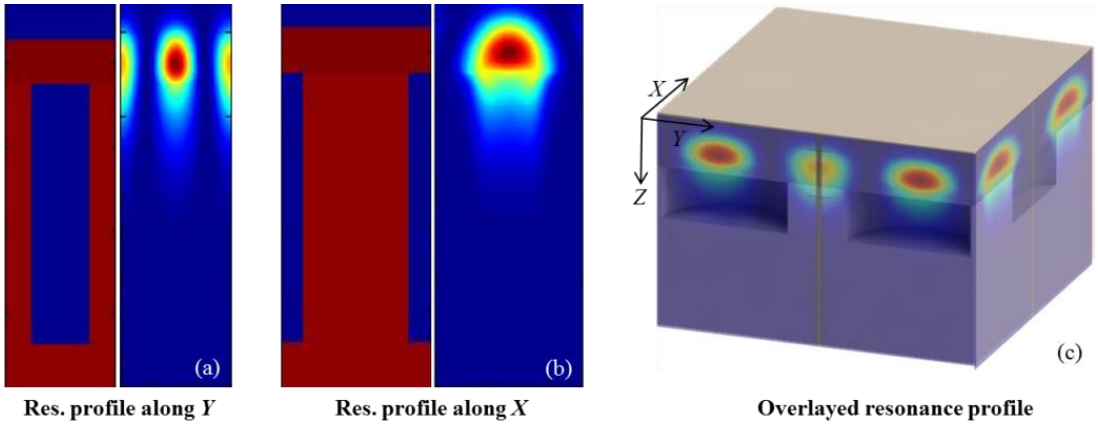

Fig. 3.18. Simulated field profiles along the (a) Y and (b) X direction are shown at the resonance condition. (c) The fields are overlapped onto the inverted grating structure.

The fabrication space of the inverted hexagonal geometry is illustrated in Fig. 3.21 – 3.26, with device parameters listed in the inset, simulated at TE polarization. The resonant fields in along X and Y are identified by the TE_{ij} and TM_{kl} modes shown above the resonances. Throughout the text, these are indicated by $TE_{ij}TM_{kl}$. As with the linear-grating devices, TE_{ij} represents a TE mode profile in the waveguide in the YZ plane characterized by *i* vertical divisions and *j* horizontal divisions of the mode intensity distribution and TM_{kl} represents a TM mode profile in the waveguide in the XZ plane

characterized by *k* vertical divisions and *l* horizontal divisions of the mode intensity distribution. Using the device geometry (Fig. 3.19) and fabrication parameters (Fig. 3.20), the ideal inverted device produces a resonance at λ_{res} = 1718 nm with a 3 nm FWHM for both TE and TM polarizations.

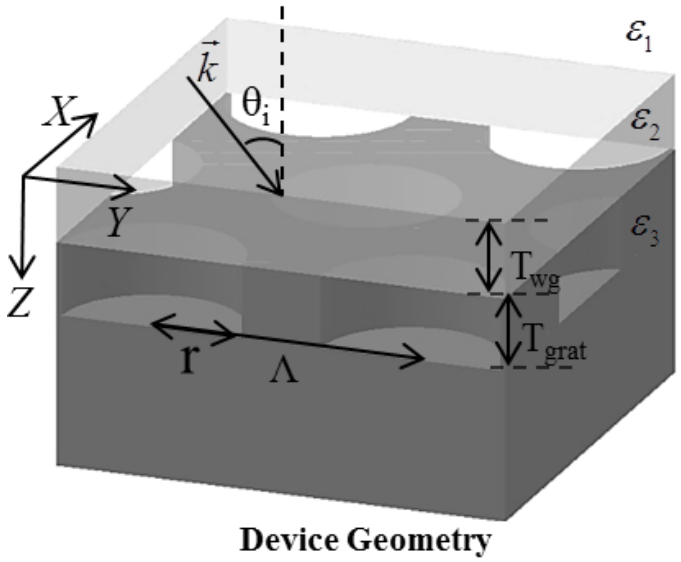

Fig. 3.19. Ideal refractive index profile for the inverted hexagonal grating geometry.

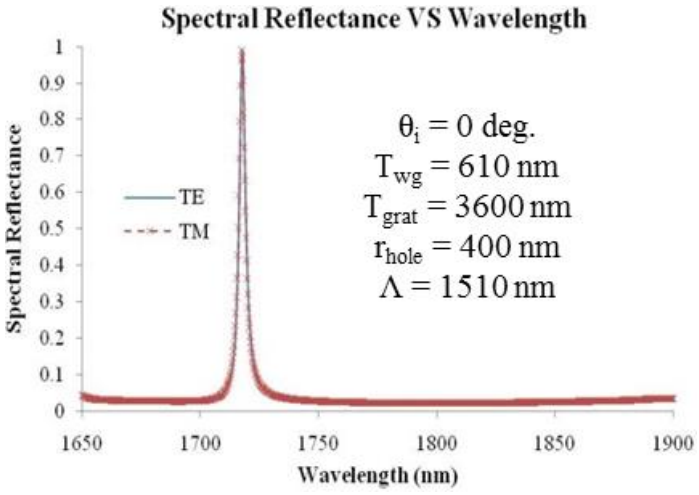

Fig. 3.20 Reflectivity is simulated versus wavelength for the ideal inverted hexagonal grating geometry.

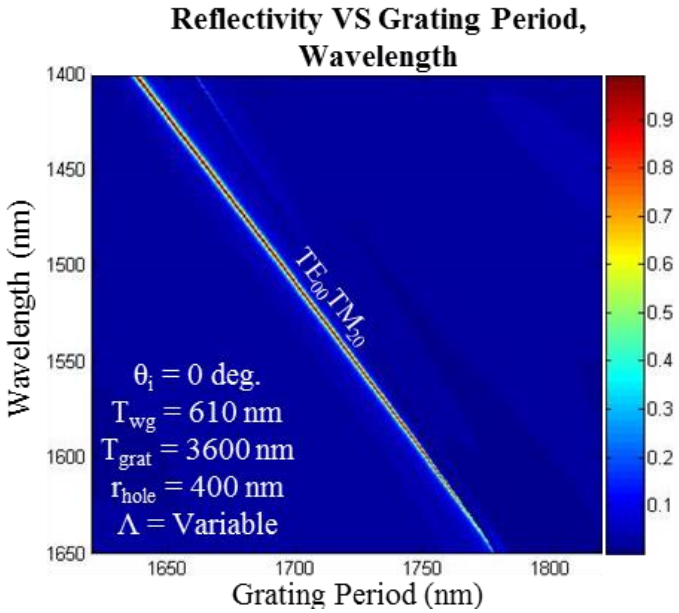

Fig. 3.21. Reflectivity is simulated versus wavelength as a function of lateral grating period for the ideal inverted hexagonal grating geometry. Incident radiation is TE polarized.

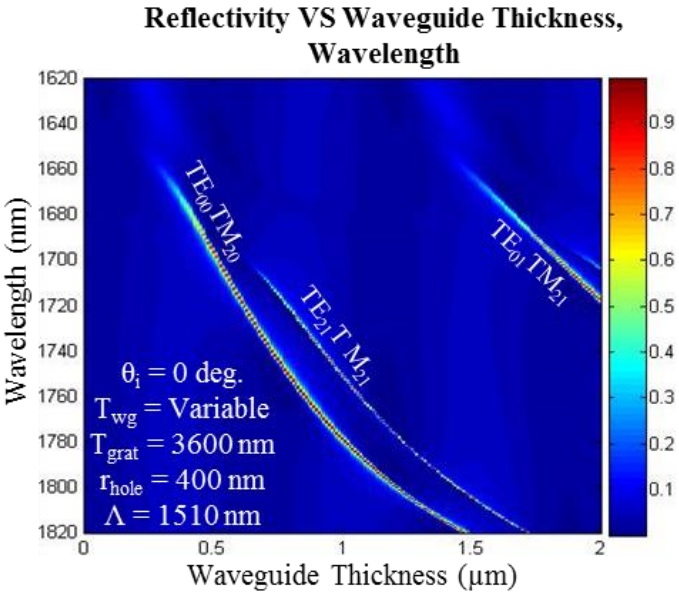

Fig. 3.22. Reflectivity is simulated versus wavelength as a function of waveguide thickness for the ideal inverted hexagonal grating geometry. Incident radiation is TE polarized.

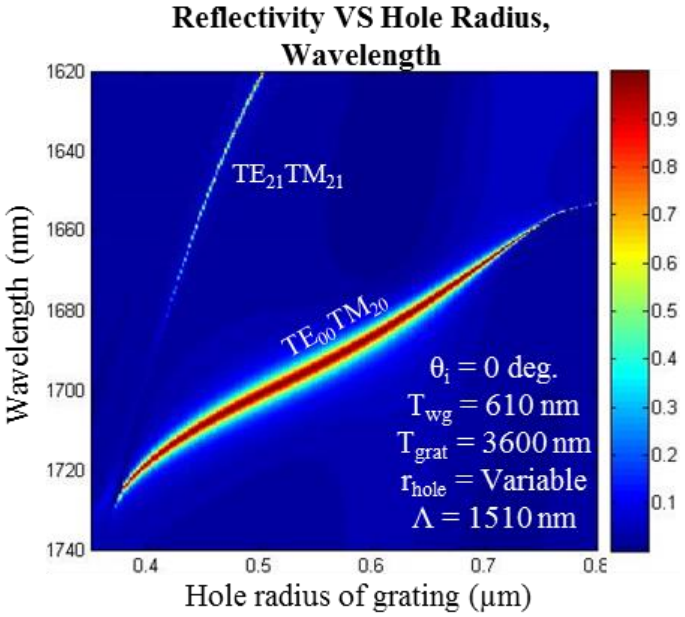

Fig. 3.23. Reflectivity is simulated versus wavelength as a function of hole radius for the ideal inverted hexagonal grating geometry. Incident radiation is TE polarized.

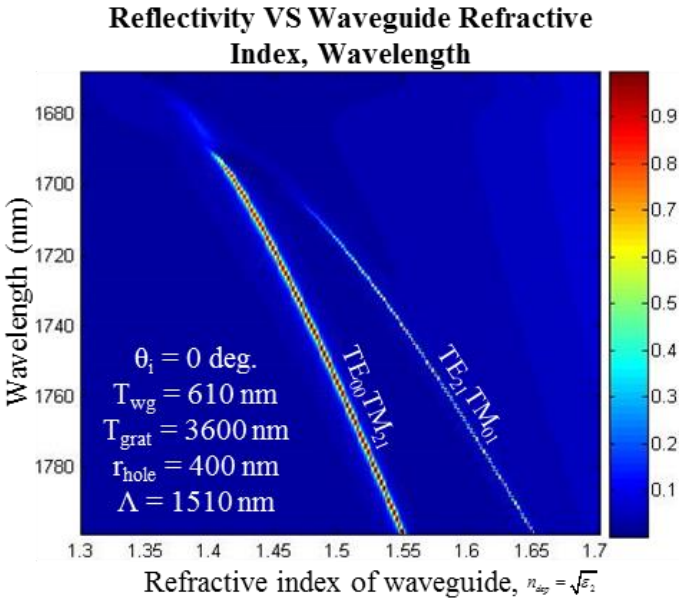

Fig. 3.24. Reflectivity is simulated versus wavelength as a function of the waveguide's refractive index for the ideal inverted hexagonal grating geometry. Incident radiation is TE polarized.

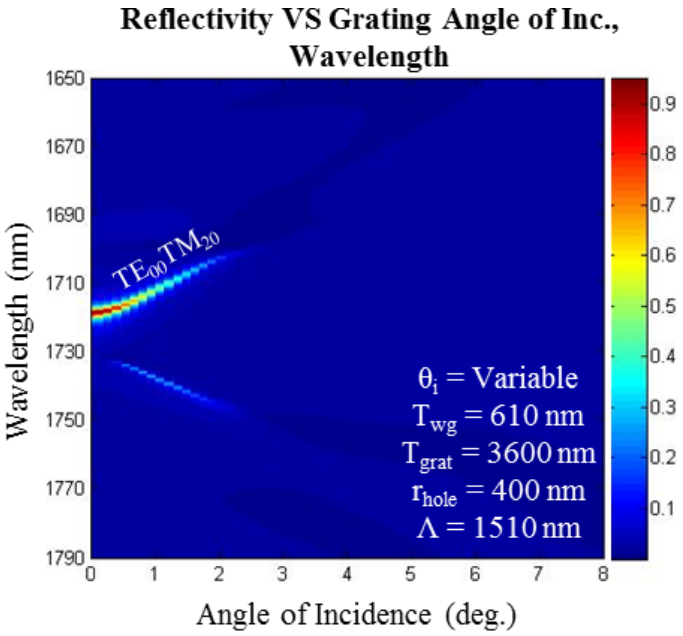

Fig. 3.25. Reflectivity is simulated versus wavelength as a function of angle of incidence on the ideal inverted hexagonal grating geometry. Incident radiation is TE polarized.

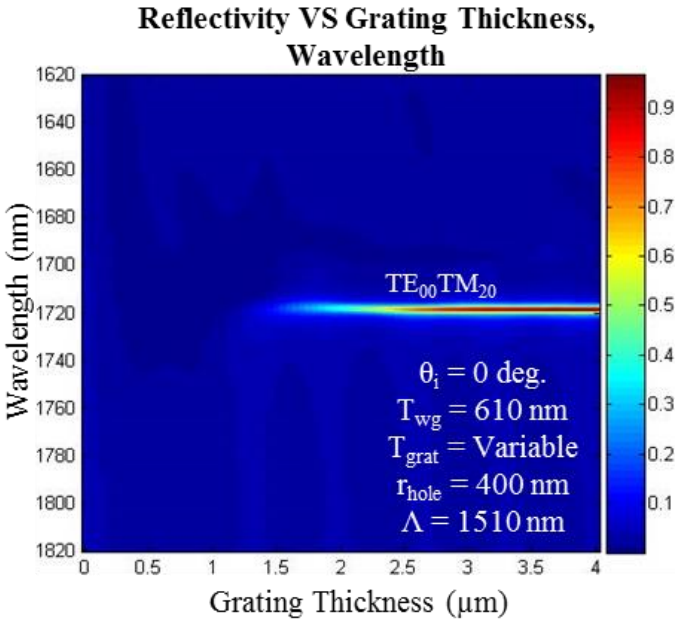

Fig. 3.26. Reflectivity is simulated versus wavelength as a function of grating thickness for the ideal inverted hexagonal grating geometry. Incident radiation is TE polarized.

First, the effect of the lateral grating period on the resonance location was examined (Fig. 3.21). The lateral period (Λ) is defined as the distance between the centers of two adjacent holes, as shown in Fig. 3.19. Due to the hexagonal geometry of the grating, the distance between the center of the holes along X is $\Lambda_X = \Lambda$ while the center-to-center hole distance along Y is $\Lambda_Y = \sqrt{3} \cdot \Lambda$. As the period of the grating increases, the resonance wavelength red-shifts linearly at a rate of 17.4 nm for every 10 nm of lateral period increase – slightly greater than that found for the linear geometry. Furthermore, the simulation predicts that significantly increasing the period will eliminate the resonance; this occurs because the other parameters are held constant. Since all variables are strongly coupled, other parameters would necessarily need to be optimized to produce a strong resonance.

Increasing the thickness of the waveguide (Fig. 3.22) red-shifts the initial resonance, and also brings into existence other, higher-order resonances. Along the initial resonance ($TE_{00}TM_{20}$), a second resonance ($TE_{21}TM_{21}$) reaches greater than 20% reflectivity at a thickness of 680 nm and redshifts in the same manner as the initial resonance. As the waveguide thickness increases to 2000 nm, an additional resonance ($TE_{01}TM_{21}$) begins to propagate.

Increasing the radius of the holes in the hexagonal grating (Fig. 3.23) leads to a non-linearly blue-shift in the resonance location. Between radii of 400 nm and 700 nm, the $TE_{00}TM_{20}$ resonance shifts at an average rate of -1.7 nm for every 10 nm of radial increase; the negative shift is indicative of the shift to shorter wavelengths. Furthermore, the hole radius affects the width of the resonance; for this geometry, the maximum full-

width at half-maximum achieved is ~5 nm. This can be achieved by increasing the hole radius, for example, to 516 nm. In contrast, the $TE_{21}TM_{21}$ resonance is seen to blue-shift at a much faster rate, and does not share the stability of the $TE_{00}TM_{20}$ resonance.

If the permittivity of the waveguide is increased (Fig. 3.24), an effect similar to that in Fig. 3.6 is predicted. In lieu of permittivity, the refractive index was plotted as the parameter, since the permittivity and refractive index are closely related by $\varepsilon = n^2$. The main $TE_{00}TM_{21}$ resonance red-shifts at an average rate of 80 nm for each increase of the $\Delta n_{wg} = 0.01$ in the waveguide index. The higher order resonance, $TE_{21}TM_{01}$, also red-shifts with an increase in the waveguide refractive index, shifting at an average rate of 58 nm for every $\Delta n_{wg} = 0.01$.

As the illumination is moved off-normal (Fig. 3.25), the initial resonance location is seen to blue-shift and split into two unequal resonances. The main, strong resonance demonstrates a $TE_{00}TM_{20}$ mode profile. In their linear regions, the strong and weak resonances shift -9.5 nm and 8.3 nm for every increment of $\Delta\theta_i = 1°$. Furthermore, the amplitude of the $TE_{00}TM_{20}$ resonance decreases by half within a 1° offset.

Lastly, the Fig. 3.26 illustrates the effect of the grating thickness on the resonance. As the grating thickness exceeds 2 μm, a strong resonance stabilizes, and remains at a constant spectral location. The large separation of the waveguide and substrate allows for a significantly thick layer of a lower effective refractive index to form under the waveguide. Simultaneously, this eliminates the possibility of a super mode forming between the waveguide and substrate, within the spectral region of interest.

3.5 Fabrication Process (Hexagonal Grating)

Fabrication of the device illustrated in Fig. 3.19 uses similar techniques as those illustrated in Fig. 3.1. With the foresight of how the waveguide forms (Fig. 3.11), additional processes were made to ensure vertical sidewalls so that a more pencil-shaped void would be obtained as the waveguide is formed. The fabrication process is illustrated in Fig. 3.27.

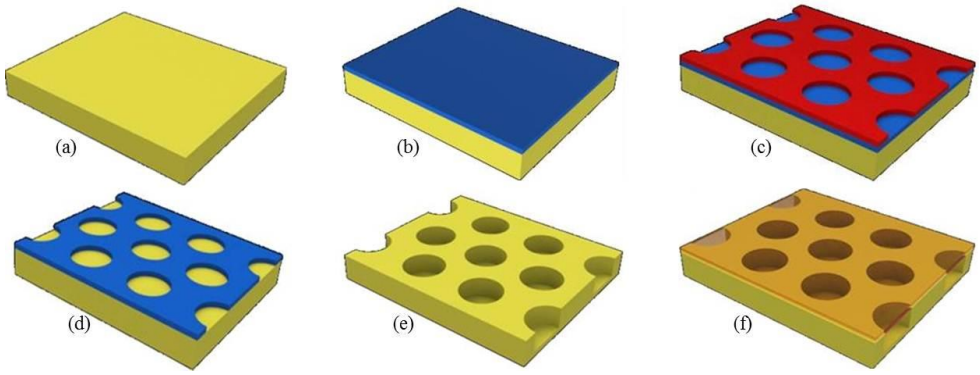

Fig. 3.27. The fabrication process for the inverted hexagonal GMRF design is illustrated.

Four inch diameter, UV-grade fused silica substrates are cleaned prior to the addition of a thin layer of chrome to utilize as a hard etch mask. The 155 nm thick chrome layer is deposited via electron beam physical vapor deposition (PVD) on a Lesker PVD 75 tool. Shipley 1805 [63] photoresist was spin-coated on to the coated wafer to a thickness of 380 nm. The photoresist was subsequently patterned on a GCA g-Line 5X reduction stopper tool. Acting as an etch mask for the chrome layer, the lithography hexagonal grating pattern was transferred into the chrome layer with a wet etch process.

The pattern transfer into the chrome etch is a particularly difficult step in this process. Due to the small feature size, it is difficult to tell when the hole has adequately cleared using the wet chrome etchant. In order to tell when the hole was adequately

cleared, a microscope capable of back-side illumination was used. Top-down illumination with a microscope allows for the top layer of the patterned photoresist to come into focus. By switching to backside illumination, the diameter of the cleared holes can be determined by the amount of light shining up through the chrome mask. This process is complicated by the fact that the chrome etch process is an immersion step -- additional etch time beyond when the holes have cleared allows the chrome etchant to eat under the photoresist pattern. Since it is difficult to discern the boundary of the photoresist using back-side illumination, the final pattern transferred into the chrome mask cannot be observed without removing the photoresist. Once the photoresist is removed, however, further chrome etching cannot be done since the mask has been removed.

The photoresist was then stripped, and an inductively coupled plasma (ICP) etcher (Unaxis Versaline) transferred the pattern of the chrome mask into the substrate. As with the fabrication of the inverted linear structure, the etch process utilized 70 sccm (cubic centimeters per minute at standard temperature and pressure) of CHF_3 and 2 sccm O_2 to obtain an etch rate of 260 nm/min. in fused silica. The fused silica to chrome etch electivity was found to be 10:1. 800 W and 40 W of ICP RF and bias RF powers were used.

Following the transfer etch, remaining chrome on the wafer's surface was removed with a wet etch process. Plasma enhanced chemical vapor deposition (PECVD) on an STS PECVD tool employed high-frequency oxide layer deposition to deposit silicon oxide over the etched grating structure. The PECVD process used a 30 W RF

power combined with 1420 sccm of nitrous oxide and 2% silane (400 sccm) to achieve a 50 nm/min deposition rate. A 32 min. deposition resulted in a 1.6 μm thick layer of SiO_x. The cross-section of the fabricated device is shown in Fig. 3.28.

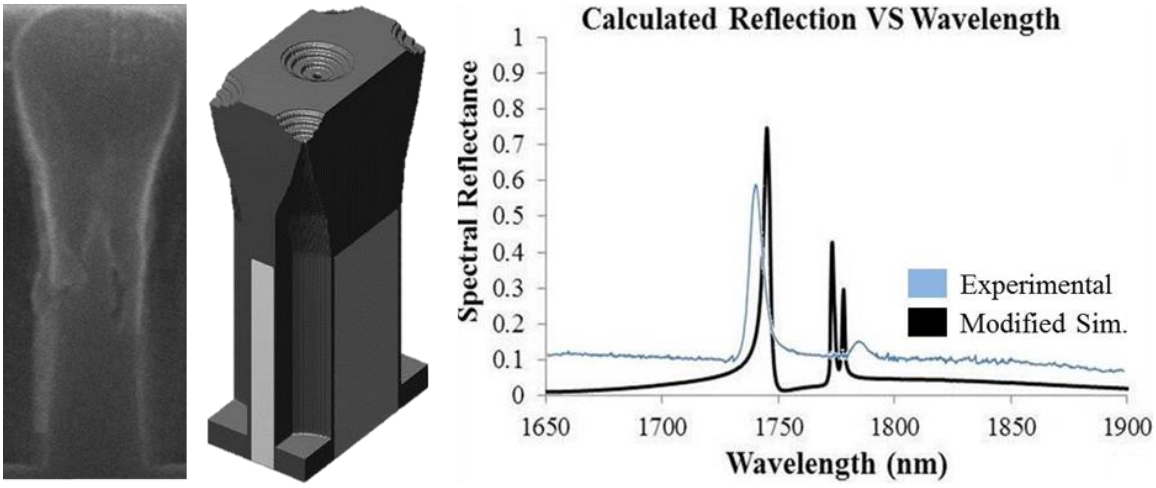

Fig. 3.28. (Left) Cross-section SEM of the fabricated device. (Middle) The cross-section created from measured SEM images as a material profile for simulations. (Right) Overlapped plots of reflection versus wavelength for fabricated and simulated profiles.

The formation of the shoulders was expected in the same manner as the linear grating, since the fabrication process makes the shape of the waveguide independent of material. Unlike the inverted linear grating geometry, the deposition on the hexagonal devices was stopped prior to the shoulders meeting. While the air void is not completely encapsulated, the effective refractive index of the leaky waveguide continues to satisfy the coupling condition needed to form a resonance. This is an effect of phase matching at the boundary using the grating equation for a hexagonal grating geometry and the effective index of the leaky waveguide at the top of the structure.

SEM measurements from both the *XY* and *YZ* planes were used in subsequent simulations examine the device's fabrication space. In doing so, lateral measurements could be made of the hole diameter along *Z*, and were appropriately scaled based on the

elliptical nature of the holes in the hexagonal grating from the *XY* plane. The SEM images are shown in Fig. 3.29.

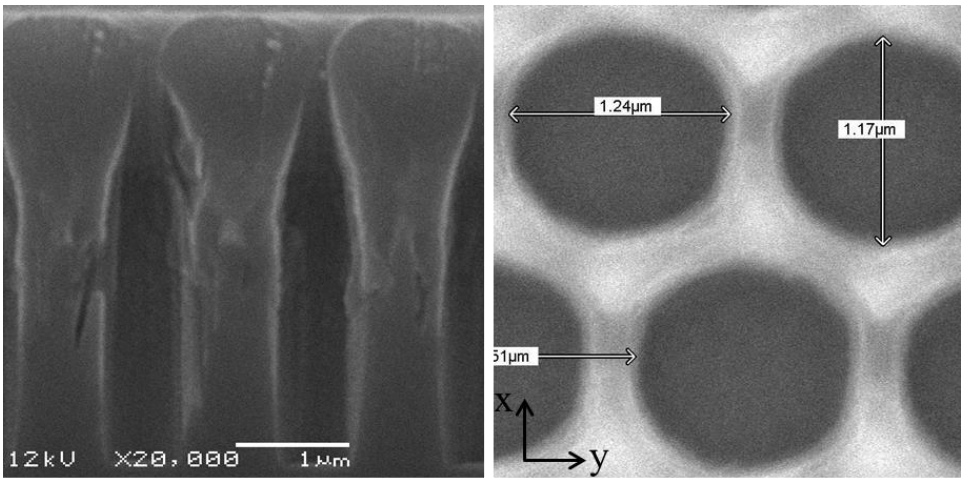

Fig. 3.29. (Left) Cross-section SEM of the fabricated device along *YZ* plane. (Right) SEM image along the XY plane prior to waveguide PECVD deposition. The ellipticity of the holes is measured using the indicated measurements.

Using the above measurements, the holes have a slightly elliptical profile; the ratio of the diameters in X and Y are $d_y/d_x = 1.059$. The simulated device and its associated process space are illustrated in Fig. 3.30 – 3.34.

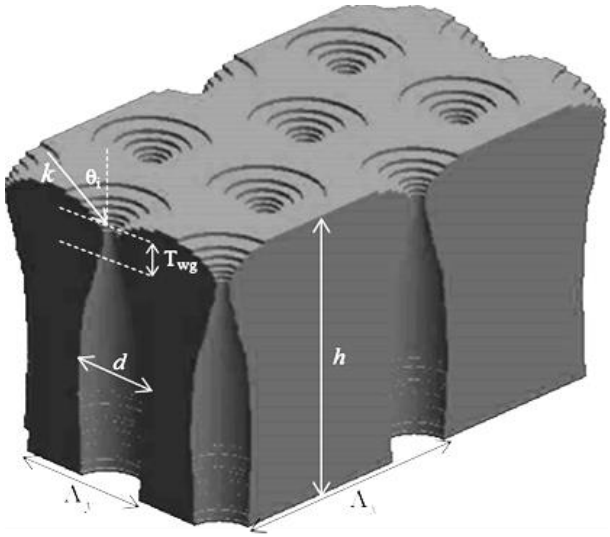

Fig. 3.30. Three-dimensional reconstruction of the refractive index profile used to explore the process space.

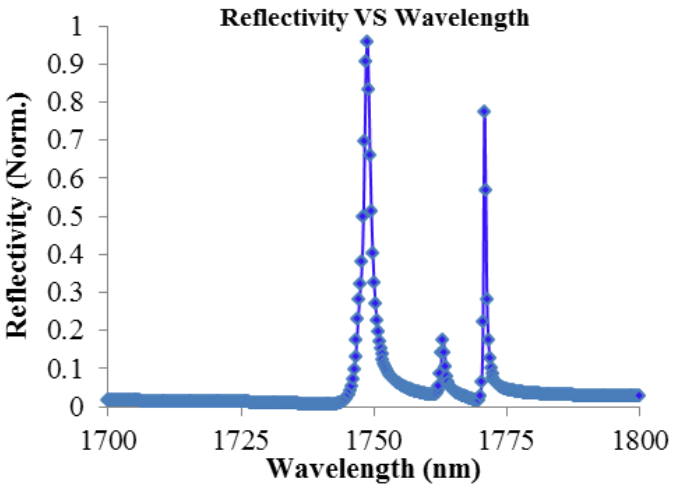

Fig. 3.31. Reflectivity versus wavelength for the structure shown in Fig. 3.30. Measurements are in TE polarization.

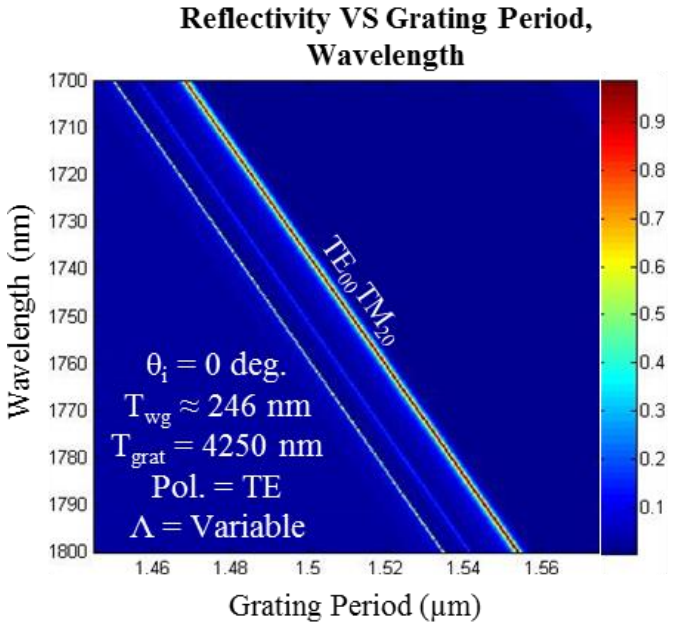

Fig. 3.32. Reflectivity is simulated versus wavelength as a function of the lateral grating period for the fabricated inverted hexagonal grating geometry. Incident radiation is TE polarized

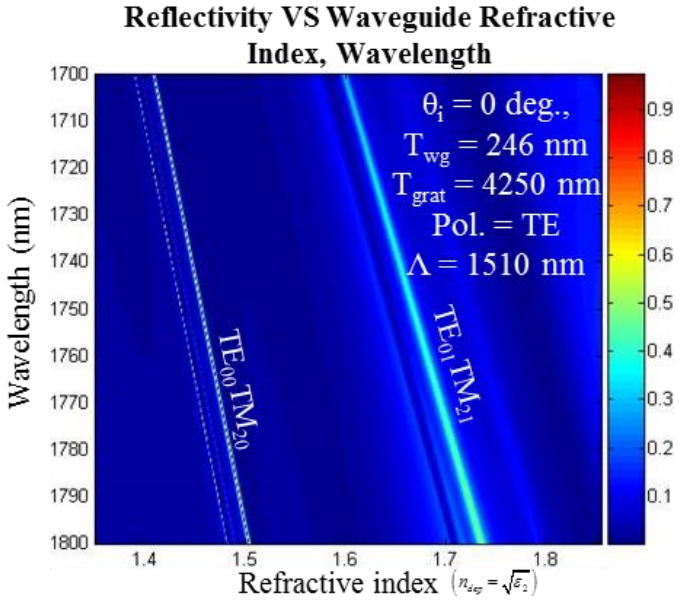

Fig. 3.33. Reflectivity is simulated versus wavelength as a function of the refractive index of the deposition for the fabricated inverted hexagonal grating geometry. Incident radiation is TE polarized.

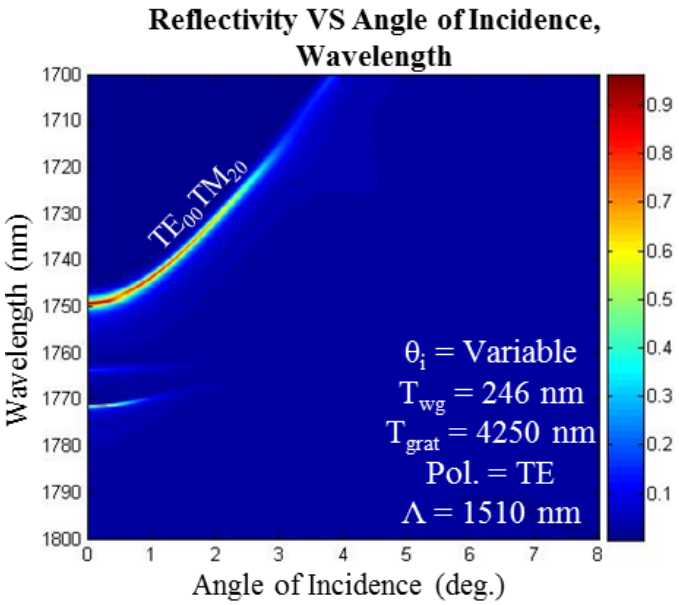

Fig. 3.34. Reflectivity is simulated versus wavelength as a function of the angle of incidence for the fabricated inverted hexagonal grating geometry. Incident radiation is TE polarized.

Due to small differences between the geometries of Figs. 3.28 and 3.30, variation is seen between the plots of reflectivity versus wavelength of the two devices (Figs. 3.28 and 3.31). However, this has little influence on mapping the process space shown above. For simplicity of discussion, the main resonance will be the primary concern. The strongest resonance in Fig. 3.31 was identified as a $TE_{00}TM_{20}$ mode with 95.73% reflectivity and a 1.5 nm FWHM. As the lateral period $\left(\Lambda_y\right)$ is increased, the resonance linearly redshifts at a rate of 12 nm for each increment of $\Lambda_y = 10$ nm; this is illustrated in Fig. 3.32. Similarly, increasing the refractive index of the deposition causes the refractive index of the waveguide to increase. For each increment the refractive index is increased by $\Delta n_{wg} = 0.01$, the resonance red-shifts 10.75 nm (Fig. 3.33). Finally, the resonance is predicted to blue-shift nonlinearly with an increasing angle of incidence (Fig. 3.34). As θ_i increases, the resonance maintains greater than 75% reflectivity out to 1.38 degrees. In the somewhat linear portion of its spectral shift, the resonance shifts at a rate of -14.93 nm/deg. Moreover, the less intense guided modes at the longer wavelengths quickly reduce beyond $\theta_i = 1°$.

3.6 Experiment and Analysis

The spectral response of both fabricated structures was measured on a Woollam Ellipsometer tool. The results, overlapped with modified simulation profiles are shown in Fig. 3.10 and Fig. 3.28 for the linear and hexagonal geometries, respectively. Measurements of the SEM cross-sections have allowed the resonance to be well

understood for the linear grating case, and good agreement has been found between experiment and theory.

However, the case of the hexagonal geometry is markedly different for two reasons. First, neither the modified simulation nor the experimental measurements yielded a strong resonance. Secondly, the ideal simulations of the hexagonal geometry predict a single resonance for the fabricated device – experimental measurements show that a second resonance arises, red-shifted of the main resonance by ~30 nm. Further investigation into the cause of the second resonance reveals that the deposition growth over the hex grating increases the effective index over the entire height of the shoulder, effectively increasing the thickness of the waveguide. The thick, non-planar nature of the waveguide allows additional hybrid modes to exist, manifesting as weakly guided modes across a higher effective index region. This is similar to the additional resonances in Fig. 3.22.

In contrast, the spectral responses from the linear and hexagonal gratings are noticeably different. Based on the fabrication space for the hexagonal structure, alterations to the fabrication design may be made in order to ensure a stronger, more stable resonance profile. Plots from Fig. 3.23 – 3.26 suggest that at normal incidence, the thickness of the grating and lateral period are adequate. However, the width of the resonance can be increased by increasing the radius of the grating holes to 500-600 nm. Furthermore, increasing the deposition length would bring the edges of the shoulders closer together allowing a more optically confined waveguide to form, causing stronger mode confinement.

3.7 Conclusion

The narrow linewidth and overall stability for mid- to high-power laser systems rely heavily on the geometry of the outcoupler component. While multilayer DBR devices are typically used to provide strong cavity feedback, their dependence on the refractive index and precise layer thickness make them an unattractive solution to providing cavity feedback. Furthermore, little work has been done to demonstrate DBR operation at large off-normal angles of incidence. Given the variation in thermal properties between the layer materials, high temperatures can lead to cracking and delamination of the layers based on the differential thermal expansion between materials.

Guided-mode resonance filters were explored as a means to provide narrowband reflectivity for cavity feedback. The GMRF designs are easily tunable, and can be spatially varied to exploit resonance across a range of incident wavelengths. Furthermore, by exploiting conditions, a monolithic resonant structure may be realized. Simultaneously protecting the grating layer, the single-material nature of the resonant device ensures that all portions of the device will react similarly to an increase in temperature and incident power density.

The fabrication process of the monolithic resonant structures takes advantage of the natural air-void formation during the top-down deposition process on an etched grating. With an increase in deposition thickness, the top-most edges of the grating ridges begin to naturally round, growing in size. When the shoulders become large enough, an air pocket is formed creating an index contrast between the submerged grating and the top waveguide layer.

In order to demonstrate control over the devices' polarization dependence, both linear and hexagonal grating geometries were explored. Due to the low index contrast between the device and its surrounding medium, narrowband resonance was achieved in both instances. The hexagonal grating produced similar responses for both TE and TM polarization states.

CHAPTER FOUR

ENCAPSULATED RESONANT WAVEGUIDE GRATINGS

4.1 Introduction

While the design of the inverted resonant structures protects the grating layer while providing homogenous resonant structures, the waveguide layer remains vulnerable to the surrounding atmosphere. A design was conceived to encapsulate the waveguide and grating, simultaneously protecting them both via addition of a thick cladding layer [74]. For simplicity, the grating and waveguide are combined into a single resonant layer [35]. Since the waveguide grating layer has a significantly high effective index, a low index cladding layer is added on top of the existing waveguide structure. A thick cladding layer is then added for protection.

4.2 Design and Process Space

In order to map the device's fabrication tolerances, an ideal refractive index profile was built (Fig. 4.1) and used to explore the dependence of the reflectance on each parameter (Figs. 4.2 – 4.7). Light of a certain wavelength is incident on the surface of the device at angle of incidence θ_i. Incident light is TE polarized, with the electric field oscillating parallel with the grating lines. The electric permittivity of the superstrate, grating/cladding, and deposition material are given by ε_1, ε_2, and ε_3, respectively; equation (1.19) is used to find the refractive index. Experimentally, the cladding layer will be bonded to the top of the grating. The fill factor of the grating pillars compared to

the lateral period is given by $f \cdot \Lambda,$ where Λ is the lateral period. The key hole in the center of the structure is used to further alter the effective index in the waveguide grating; its height and width are given by T_{kh} and w_{kh}, respectively.

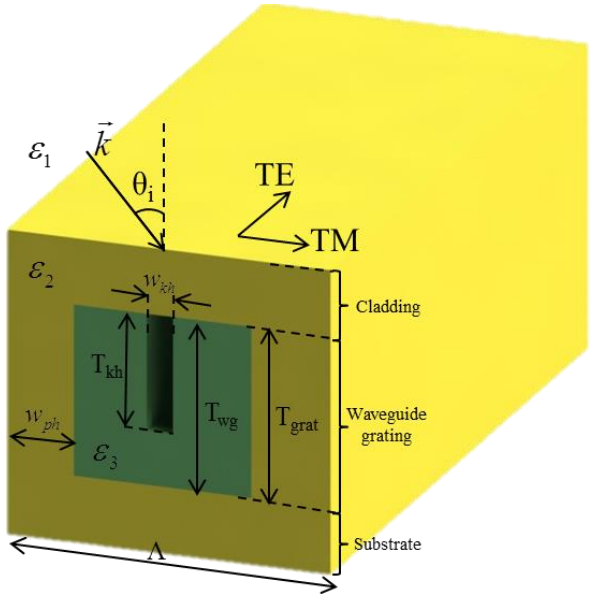

Fig. 4.1. Ideal refractive index profile for the encapsulated linear grating geometry.

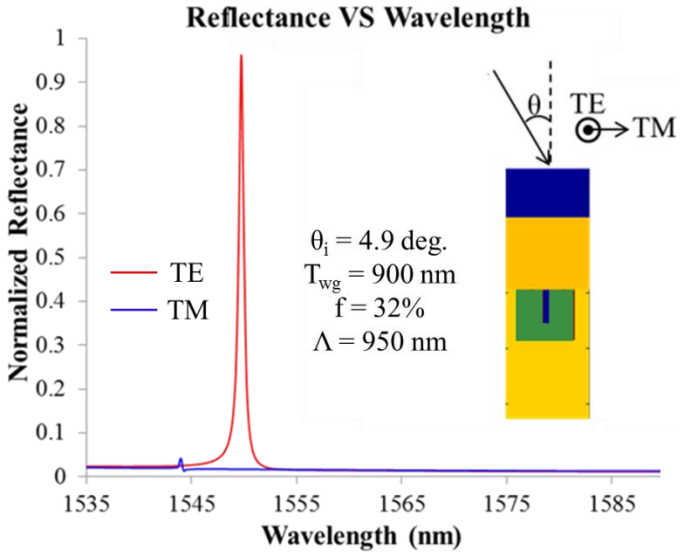

Fig. 4.2. Reflectivity is simulated versus wavelength for the ideal encapsulated linear grating geometry.

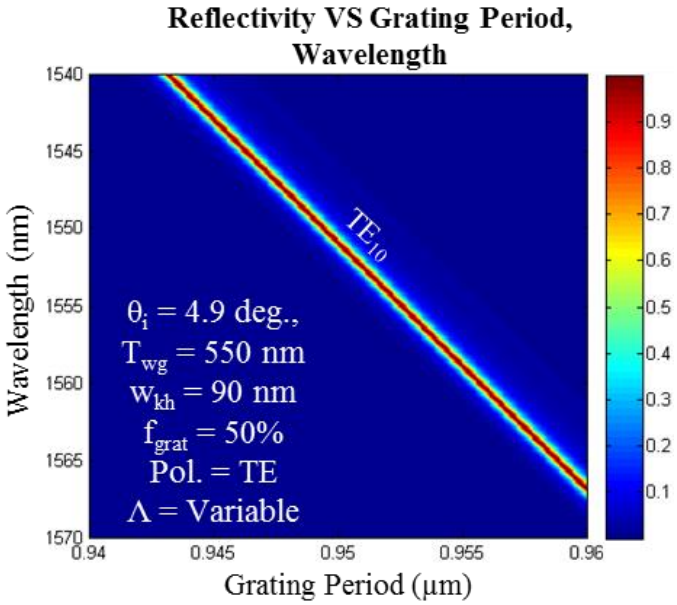

Fig. 4.3. Reflectivity is simulated versus wavelength as a function of lateral grating period for the ideal encapsulated linear grating geometry. Incident radiation is TE polarized.

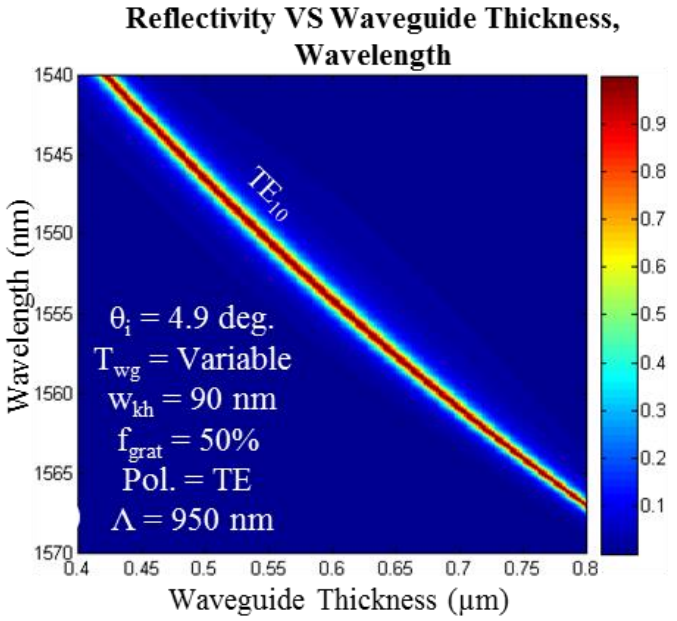

Fig. 4.4. Reflectivity is simulated versus wavelength as a function of the thickness of the waveguide layer, for the ideal encapsulated linear grating geometry. Incident radiation is TE polarized.

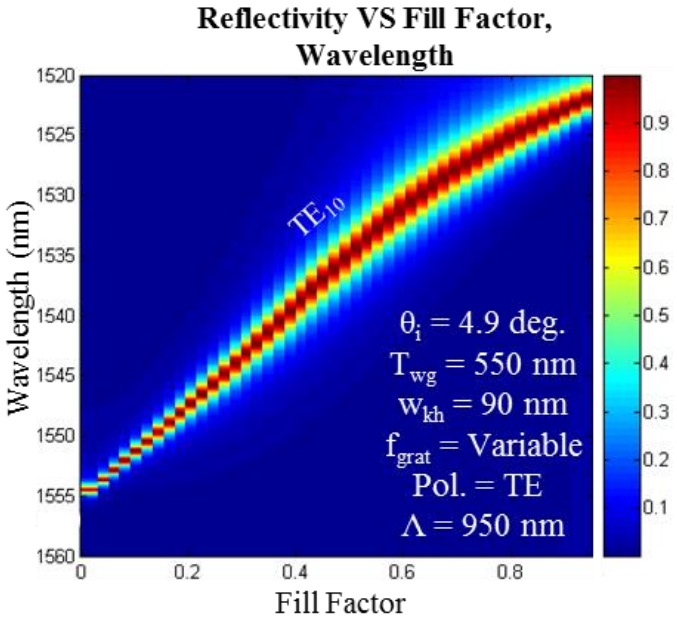

Fig. 4.5. Reflectivity is simulated versus wavelength as a function of fill factor for the ideal encapsulated linear grating geometry. Incident radiation is TE polarized.

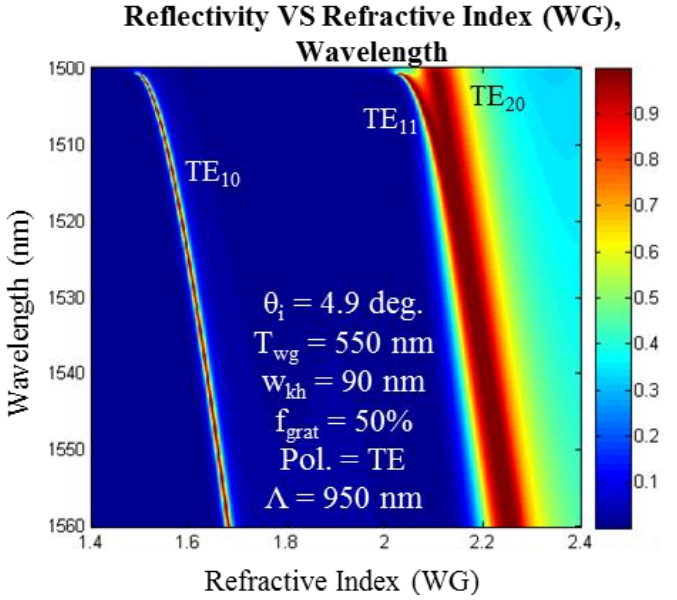

Fig. 4.6. Reflectivity is simulated versus wavelength as a function of the refractive index of the encapsulated material, for the ideal encapsulated linear grating geometry. Incident radiation is TE polarized.

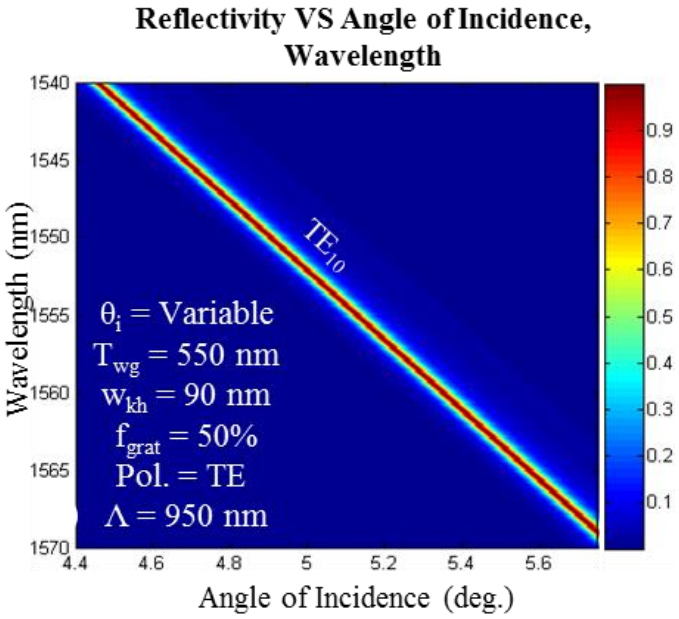

Fig. 4.7. Reflectivity is simulated versus wavelength as a function of angle of incidence for the ideal encapsulated linear grating geometry. Incident radiation is TE polarized.

As the lateral period of the encapsulated linear grating is increased, the resonance is seen to red-shift (Fig. 4.3) in a linear manner at a rate of ~16.7 nm for each increment of $\Delta\Lambda = 10$ nm. Over the range of the spectral shift, the linewidth remains constant; the resonant mode in this device demonstrates a TE_{10} mode profile. If the total height of the waveguide grating region is increased, the resonance undergoes a nonlinear red-shift (Fig. 4.4); with a short waveguide, this exhibits single-mode resonance, exhibiting only the TE_{10} mode. As the thickness of the waveguide increases, the resonance nonlinearly shifts to longer wavelengths. Over the change in waveguide grating thickness, the FWHM of the resonance decreases from 1 nm to 0.6 nm.

The air pocket was purposefully built into the design of the encapsulated grating so that the effective index in the waveguide layer can be carefully tailored. By adding a pocket of air, the overall effective index of the grating layer is lowered; this is similar in

nature to the lower effective index for the inverted grating structures. However, the air pocket can be replaced by another material to further alter the resonance condition. For a pocket of air, however, the effect of the void width on the resonance condition can be seen from Fig. 4.5. As the width of the void is increased, the resonance nonlinearly blue-shifts; in the linear region, this shifts at a rate of ~4 nm for each increment of $\Delta w_{kh} = 100$ nm. The asymptotic shift at larger values of w_{kh} can be explained by the effective index slowly approaching a single value – this occurs because w_{kh} cannot exceed the width between the grating pillars, and thus has a minimum value. The widening of the FWHM is also accounted for; the resonance conditions dictate that the strongest field enhancement will occur where the effective index is the highest. For this device, that places the resonances below the air pocket or keyhole; increasing the width of the keyhole has the effect of increasing the index contrast surrounding the waveguide region. As noted in the discussion of the inverted resonant structures, this increases the FWHM of the resonance [60].

Given that the deposition of the high-index material is conformal, a variety of materials may be deposited; the effect of altering the refractive index of this material is illustrated in Fig. 4.6. As the refractive index is increased, the spectral location of the resonance quickly shifts to long wavelengths at a rate of ~43.1 nm for each increment of $\Delta n_{dep} = 0.1$ that the refractive index of the deposition is increased. Although not immediately apparent, the FWHM of the resonance also increases in accordance to the increasing high index contrast between the waveguide and its surrounding layers, varying from less than 1 nm, to a 5.1 nm FWHM for the TE_{10} mode. At higher indices, a

broadband resonance may be found; upon closer inspection, the resonance is a combination of the TE_{11} and TE_{20} modes. When the resonances are split, the larger resonance has a 16 nm FWHM; however, with the combined resonances, the FWHM demonstrates a 53.1 nm FWHM, more than 10 times the width of the initial resonance.

Finally, the spectral location of the resonance is seen to linearly red-shift (Fig. 4.7) with an increase in the angle of incidence. The resonance location shifts at a rate of 22.4 nm for each increment of $\Delta\theta_i = 1$ deg.

4.3 Fabrication Process

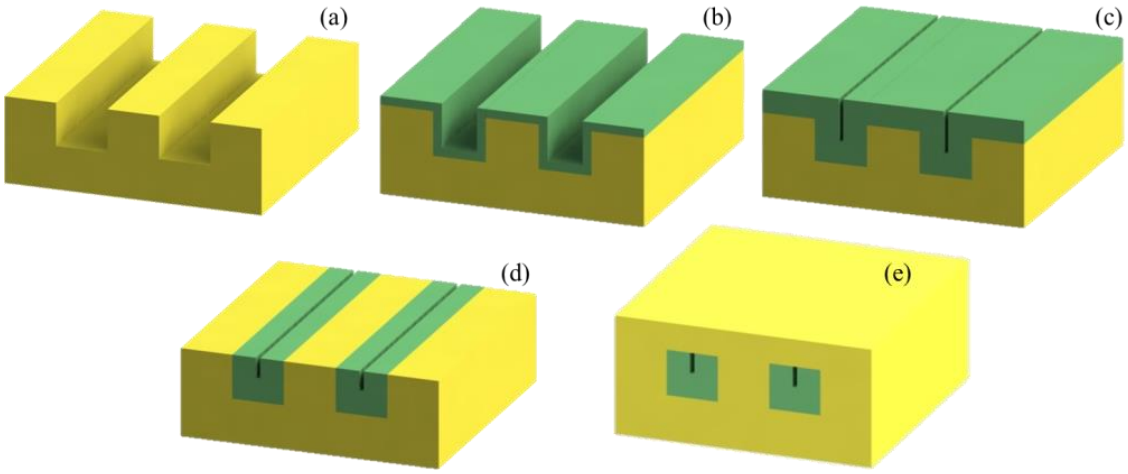

Fig. 4.8. The fabrication process for the encapsulated linear GMRF design is illustrated.

Prior to fabrication, the substrate was cleaned with an NMP bath and subsequent alcohol rinse. The UV-grade fused silica substrates (1 mm thick, 100 mm diameter) were immersed in a monolayer adhesion promoter to prevent resist liftoff during the fabrication process. A 1 µm thick coating of AZ MiR 701 photoresist [75] was spin coated onto the substrate and patterned with a GCA I-line 5X reduction stepper tool,

creating an array of latent images, each 25 mm^2 in size containing 950 nm period linear gratings. A post-applied and post-exposure bake were applied before and after the exposure to reduce stress in the patterns throughout the development process.

Following the PEB, an immersion process in AZ 300 MiF solution [76] for 60 seconds developed the latent image into a relief image in the resist. In preparation for the transfer etch, a short descum etch was performed to remove photoresist from the bottom of the grating trenches to prevent micro-masking. A Unaxis Versaline inductively-coupled plasma (ICP) reactive-ion etcher (RIE) tool was used to transfer the relief pattern 900 nm into the substrate (Fig. 4.8a); a follow-up post-etch descum was done to remove remaining photoresist on the surface on the wafer and grating. All three etches were performed with the same etching tool to ensure consistent processing.

The etched grating was coated using atomic layer deposition (Fig. 4.8b,c). Trimethyl Aluminum (TMA) was used as a precursor in an Oxford OpAL tool; TMA's high vapor pressure allows the precursor to be drawn directly into the processing chamber, by chemisorbtion to attach itself to the surface of the wafer. The process chamber is purged with argon, and oxygen plasma is used to form an atomic layer of amorphous Al_2O_3 via interaction with the TMA. The chamber is purged again to complete a single ALD cycle. The Al_2O_3 deposition recipe yields a deposition rate of 0.122 nm per cycle. A 350 nm deposition is used to nearly fill the etched trenches at a rate of 5 seconds per cycle.

Unlike the top-down deposition used in the inverted GMRF structures, ALD deposition conformally coats all surfaces of the etched pattern. This means that the top,

bottom and sides of each grating trench fill equally; if the walls of the grating are not sloped towards each other, formation of an air pocket is not possible. Given a long enough deposition, the trenches will fill completely; additional deposition will cause the Al_2O_3 to planarize. In this case, the trench is not completely filled, leaving a non-filled key-hole open to finely control the waveguide grating's effective index. This open void is shown in Fig. 3.1 with width w_{kh}.

An STS III-V ICP plasma etcher was used to selectively etch away the deposited material on top of the grating pillars. Unlike the ALD, the III-V etch process is unidirectional, and does not etch the sides of the grating at the same rate as the top and bottom of the trenches. This allows the top-most deposited material to be selectively etched away, leaving the top of the grating pillars exposed (Fig. 4.8d). The etch time was optimized to completely clear remaining Al_2O_3 from the grating pillar surface, and therefore the surface of the wafer. The etch recipe utilized 50 sccm gas flow of BCl_3, 800 W coil ICP power and 250 W platen ICP power to realize a 40 nm/min etch rate. The quality of the optical polish is preserved, since the III-V etch chemistry only attacks the Al_2O_3. The top-down nature of the etch attacks the deposition on top of the grating pillars as well as the conformally-deposited corners. Since the ALD deposition is conformal, a rounded corner will form on the edges of the grating prior to the selective etching. Combined with the natural etch bias of holes and grooves (compared to open areas), this creates a funneling effect in the top of the grating holes as seen in Fig. 4.9. At this point, an SEM was taken of the device's cross-section to ensure that the desired device geometry had been obtained. This is illustrated in Fig. 4.10a. Dimensional parameters

may be obtained from the SEM image to create a refractive index profile for simulations (Fig. 4.10b).

Fig. 4.9. The III-V etch sequence is illustrated for removing the Al_2O_3 deposition.

With the top of the wafer and grating pillars exposed, wafer-to-wafer bonding was chosen as a means of fulfilling the goal of encapsulating the resonant device. Instead of a conventional wafer bonder, the substrate surface was activated using an oxygen plasma [77], [78]. The two wafer surfaces that were to be bonded were simultaneously activated for 10 minutes with an O_2 plasma recipe. The plasma used a 50 sccm O_2 flow rate, 200 W RIE power, and 300° C platen temperature. Following the etch step, the initialized surfaces were rinsed with deionized water to create a hydrophilic surface, reduce particle contamination, and improve contact bond strength. The substrate was then dried with a nitrogen gun. The wafers were then brought into contact under a weight for 2 hours. In order to preserve the bonded wafers for optical testing, the bond strength was not tested; this would break the bond, and separate the wafers. An image of the bonded wafer is shown in Fig. 4.10c.

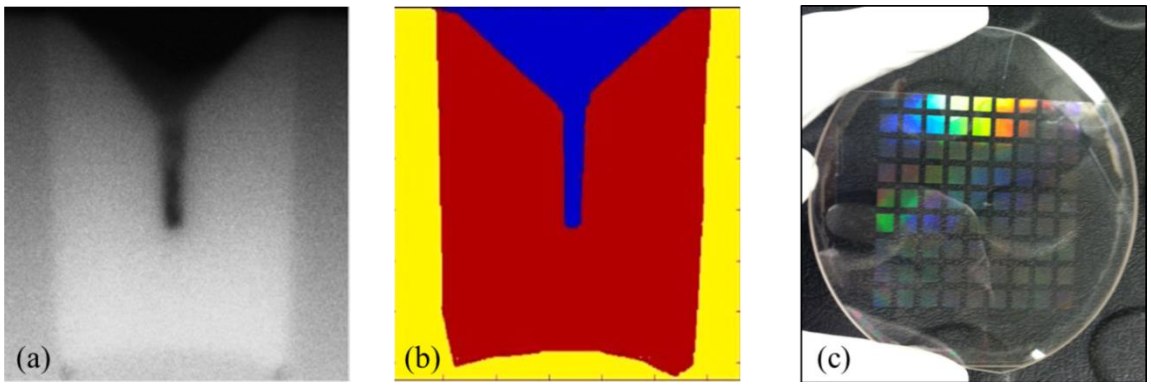

Fig. 4.10. (a) An SEM cross-section is shown of the fabricated device. (b) The SEM-based simulated refractive index profile is illustrated, bonded superstrate is not shown. (c) The fabricated wafer is bonded to a fused silica substrate.

The fabrication process remains the same regardless of the deposition material; the process space can be mapped for the fabricated devices. These are shown in Fig. 4.11 – 4.13. Using Al_2O_3 as the deposition material (n_{dep} = 1.6201), the dominant mode in the waveguide is the TE_{10}. The periodic modulation seen in Fig. 4.11 – 4.13 arises as a result of interference between the top surface of the bonded superstrate and the top of the resonant waveguide grating (labeled as “Cladding” in Fig. 4.1).

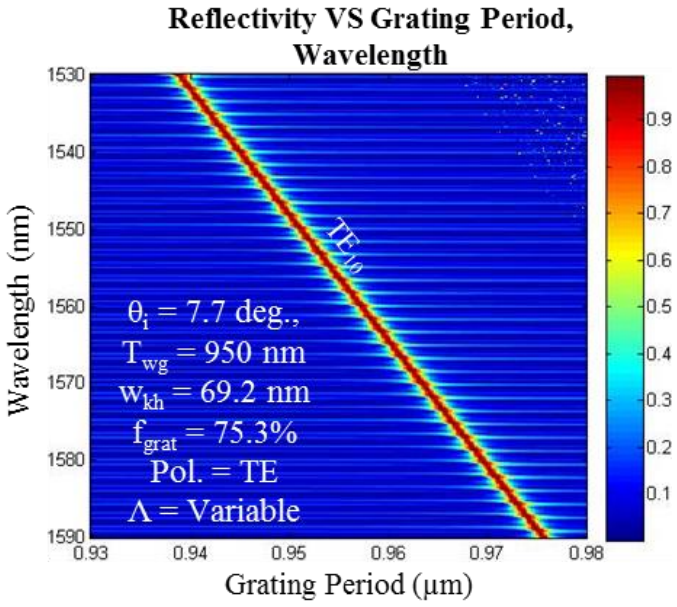

Fig. 4.11. Reflectivity is simulated versus wavelength as a function of lateral grating period for the fabricated encapsulated linear grating geometry. Incident radiation is TE polarized.

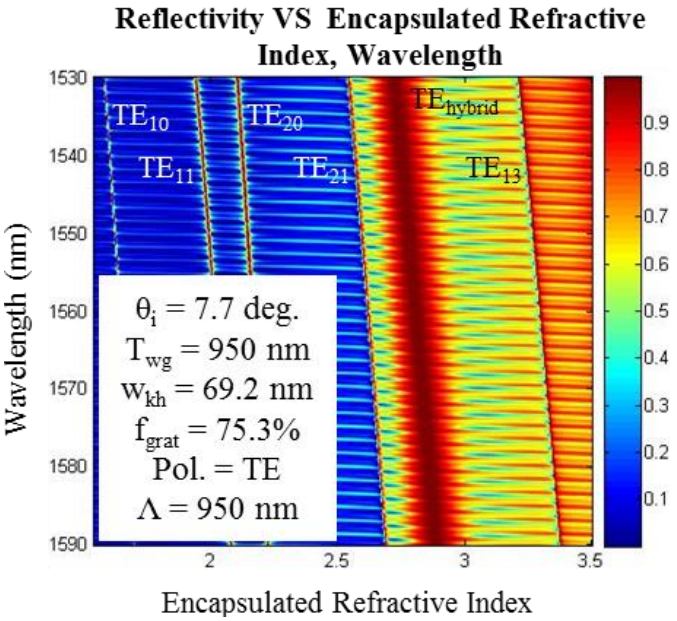

Fig. 4.12. Reflectivity is simulated versus wavelength as a function of the refractive index of the encapsulated material, for the fabricated encapsulated linear grating geometry. Incident radiation is TE polarized.

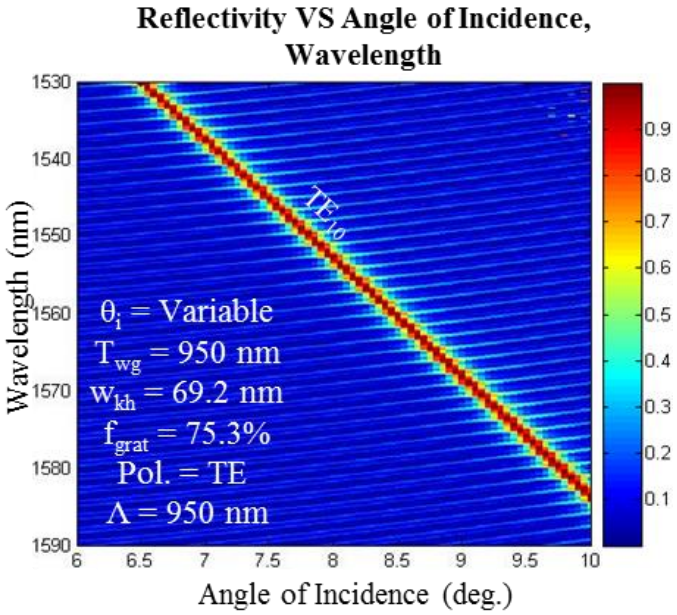

Fig. 4.13. Reflectivity is simulated versus wavelength as a function of angle of incidence for the ideal encapsulated linear grating geometry. Incident radiation is TE polarized.

Similar to the previous devices, a linear change in the grating's lateral period induces a linear red-shift in the resonance's spectral location (Fig. 4.11). The linewidth of the resonance goes unchanged, while the location red-shifts at a rate of 16.4 nm for each increment of $\Delta\Lambda = 10$ nm.

As the refractive index of the deposited material is increased, higher order modes begin to become present in the waveguide (Fig. 4.12). At low refractive indices (Al_2O_3), the dominant mode is the TE_{10} mode. As that increases to n_{dep} = 2.0, the TE_{11} mode becomes apparent, with the TE_{20} mode appearing around n_{dep} = 2.15. Likewise, the TE_{21} mode appears beyond n_{dep} = 2.59. The broad resonance at n_{dep} = 2.765 is a hybrid mode, similar to that predicted in Fig. 3.6. Finally, the TE_{13} resonance begins to propagate around n_{dep} = 3.263. All modes linearly red-shift with an increase in the refractive index

of the deposition material at an average rate of 50.1 nm for each increment of $\Delta n_{dep} = 0.1$.

Lastly, the spectral location of the resonance linearly red-shifts as the angle of incidence changes. With the parameters listed in the inset of Fig. 4.13, the resonance shifts at a rate of 15.2 nm for each increment of $\Delta\theta_i = 1$ deg.

4.4 Experiment and Analysis

The devices were tested using an amplified, polarized, tunable laser source, capable of scanning from 1525 nm to 1610 nm. Knife edge measurements confirmed the incident collimated beam size to have a diameter $1/e^2 = 700$ μm. Since the beam is collimated prior to interacting with the device, a polarization analyzer may be inserted after the collimating optics, while removing the wafer. By rotating the linear polarizer, the output power can be measured as a function of the rotation angle for the analyzer as shown in Fig. 4.12. A strong extinction ratio of $(R_{TE}/R_{TM}) = 35$ indicates a highly linearly polarized source.

Reinserting the test wafer and removing the polarizer, accurate alignment of the test wafer was achieved by mounting the device wafer on stages capable of rotation and lateral movement. During the spectral scan, wavelength increments of $\Delta\lambda = 0.5$ nm were used near the resonance; away from the resonance condition, steps of $\Delta\lambda = 1.0$ nm were used. The reflected and transmitted signals were measured simultaneously and recorded for proper normalization of the signal; this is necessary because the power of the tunable laser source varies with wavelength. The polarization of the incident beam was measured

as a function of a polarization analyzer to confirm the incident polarization. This allowed the incident polarization to be positioned in the TE plane of the wafer. An illustration of the experiment is shown in Fig. 4.14; the polarization analyzer was removed prior to the spectral measurements. The transmitted power is plotted against the rotation angle of the linear polarization analyzer in Fig. 4.15. Reflectivity versus wavelength is plotted in Fig. 4.16.

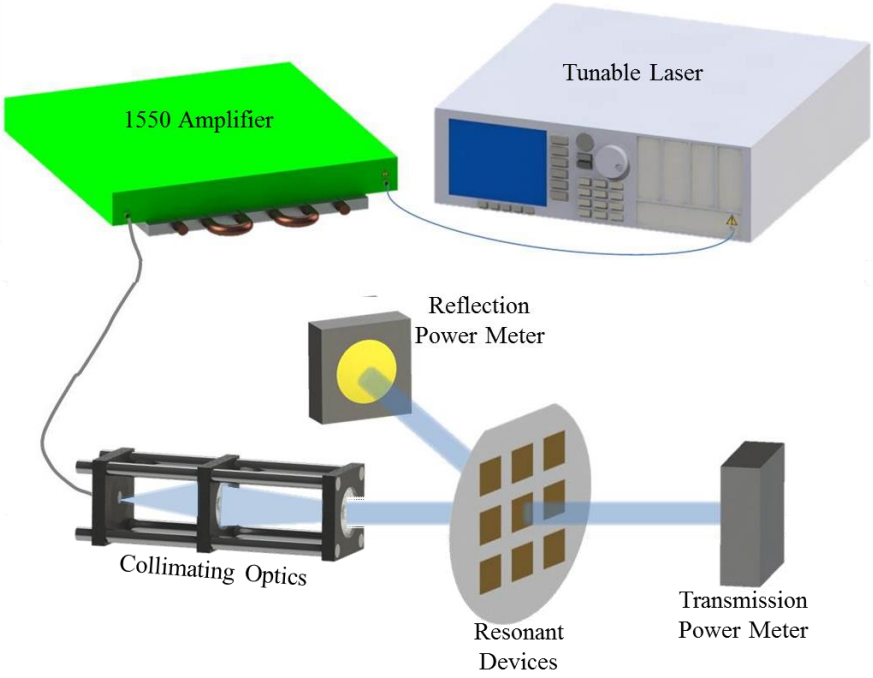

Fig. 4.14. The layout of the experiment is illustrated for testing the encapsulated resonant structures.

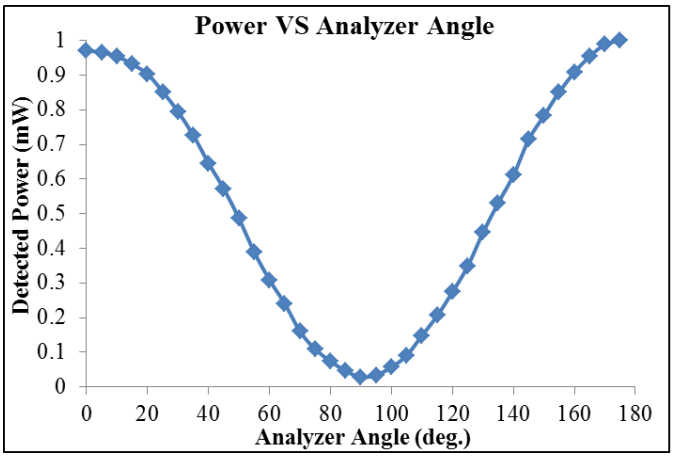

Fig. 4.15. Normalized power is plotted against the rotational angle of a polarization analyzer.

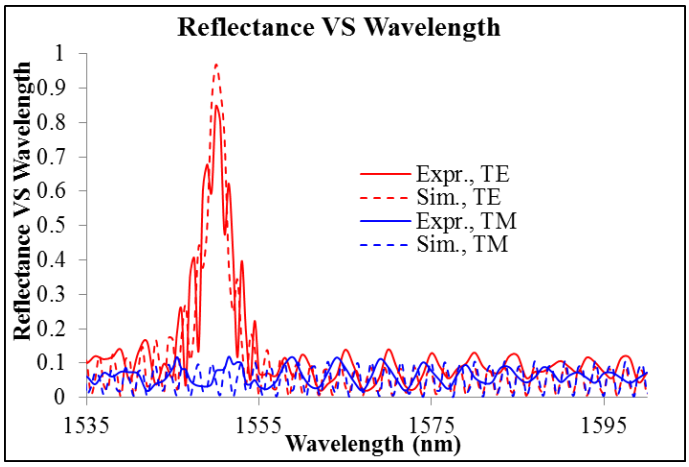

Fig. 4.16. Reflectivity is plotted against wavelength for the experimental and simulated devices in both TE and TM polarizations.

During the experiment, the device was angularly tuned to provide maximum reflection; this occurred at ~7.7 degrees relative to a normally incident beam. A strong resonance was demonstrated unique to the TE polarization, with a 5 nm FWHM and 84.6% peak reflectivity. In comparison, simulations predicted a 3 nm FWHM. Due to under-sampling in the spectral reflectivity measurements, fringes in the plotted data do

not accurately represent the etalon thicknesses. Finer sampling from SEM-based simulations predicts interference fringes with a smaller free spectral rage that was matched to the interference expected from the bonded superstrate wafer. The SEM-based refractive index profiles are shown in Fig. 4.10b; the bonded superstrate is now shown. The peak of the TE resonance, polarization sensitivity, and FWHM of the simulation agree well with the experimental results. Deviations between the two are the result of fabrication tolerances, overlapping between the interference and reflected signal, and optical alignment errors.

4.5 Conclusion

Conventional GMRF designs utilize a two-layer structure, with a planar waveguide layer underlying the top grating layer. If the grating and waveguide positions are reversed, the layers can be made from a single material. In each of these geometries, the waveguide or grating layer is rendered vulnerable to the environment. Any amount of contamination on either surface will alter the resonance conditions, thus changing the spectral response of the device.

However, the resonant conditions may remain unchanged if the resonant structure is removed from any risk of contamination. One way to achieve this is to sandwich the resonant structure between two thick, highly transmissive materials. In order to realize this geometry, a single-layer waveguide grating geometry was used in conjunction with conformal deposition and selective etching techniques. The conformal deposition of the high index material eliminates formation of unwanted air voids within the device, while

fully filling in trenches in a linear grating. Selective etching allows the topmost layer of the deposition to be removed, exposing the flat, polished tops of the grating ridges. This yields a bonding surface that can be used to anchor a second substrate, encapsulating the device.

CHAPTER FIVE

CONCLUSIONS AND FUTURE WORK

5.1 Conclusions

Guided Mode Resonance devices have seen a rapid deployment in a number of applications from imaging and sensing to laser systems at wavelengths in the UV through the mid-infrared. These devices have been used in the narrow spectral operating range to the broad spectral range, depending on the application and requirements. Given this broad application range, a number of limitations have been recognized based on the choice of material systems and the surface contamination inherent in a surface resonance structure. In order to address these weaknesses in the state of the art, this research has introduced novel concepts based on homogenous material systems to eliminate the need for different material systems that would have different thermo-optical properties and alternative ways to encapsulate structures for integration into hi power laser platforms. The contributions include modeling and design, fabrication, and testing of these new device platforms. The specific conclusions and contributions are highlighted in the following sections.

Prior to device fabrication, Rigorous Coupled-Wave Analysis and Particle Swarm Optimization algorithms were utilized to explore the process space of each device. Based on the optimized parameters, the devices were then fabricated. Cross-section SEM images of the GMRF profile were obtained along with width and height measurements of the device features. The gray-scale SEM profiles were imported into the RCWA routine for a more accurate representation of the refractive index profile. Updated simulations

were then compared with experimental results, allowing any discrepancies between the experimental and theoretical data to be better understood.

From these simulations, it was concluded that the spectral response of each device are heavily dependent on their fabrication process. Furthermore, the fabrication process can be better understood by comparing the ideal and fabricated device profiles. Based on this comparison, discrepancies between the experimental and theoretical spectral responses could be resolved.

In order to eliminate the use of multiple materials in GMRFs, an inverted resonant structure was conceived. Switching the location of the waveguide and grating layers allows for similar materials to be used for both portions, leading to a monolithic resonant structure. Top-down PECVD deposition was used to form the waveguide over etched grating pillars. Linear and hexagonal geometries were fabricated to illustrate control over the polarization dependence of the device. Cross-section SEM images of the fabricated devices were taken prior to testing. An ellipsometer was then used to obtain the spectral response of the monolithic GMRFs.

From fabricating and testing these geometries, it was concluded that inverted monolithic GMRFs are a viable solution for single-material narrowband resonant structures. This design eliminates the need for multiple materials, and addresses issues of different thermo-optical properties encountered at high power densities. By comparing the modified simulations and experimental data, a better understanding of the resonance mechanism and dependence on the fabrication space were obtained.

However, the inverted design renders the waveguide vulnerable to contamination and damage. In order to protect both the grating and waveguide, an encapsulated resonant structure was designed. A single-layer waveguide grating was fabricated on the top of a single substrate using conventional etching and ALD deposition techniques. The top layer of the deposition was selectively etched away, revealing the top-surface of the grating pillars. The newly-opened surfaces acted as a bonding surface for the second substrate. Chemical-free bonding fully encapsulated the waveguide grating between two thick substrates. Experimental measurements were taken of the spectral response before and after the bonding process.

From fabricating and testing the encapsulated devices, it was concluded that fully encapsulated resonant geometries are a viable solution for making resonant geometries free from the threat of contamination and damage. In doing so, conformal deposition, selective etching, and bonding are used to take advantage of the original optical polish of the substrate. The encapsulated devices have demonstrated high reflectivity at power densities exceeding 240 kW/cm^2.

5.2 Future Work

With the fabrication space mapped for the monolithic and encapsulated structures, future work on these devices is not limited. The resonance conditions of both geometries are well understood as a function of the fabrication parameters. Therefore, by taking advantage of different steps in the fabrication process, new and different geometries may be achieved.

The exposure step of the pattern in the photoresist can be exploited by using multiple reticles to create spatial variation along the structure's surface. Doing so will create a spatially-variant resonance condition, leading to wavelength-dependent transmitted and reflected beam profiles. These spatial variations can be applied to the monolithic and encapsulated structures to increase the functionality and protection of the resonant structures. In the monolithic structures, a smaller trench width would mean that the shoulders pinch off an air void sooner, whereas larger trench widths correspond to shoulders that may not have fused together at the end of the deposition step. Likewise, a larger trough width would lead to less filled grooves, while a thin trench width would fill much sooner.

Additionally, the deposition step can be exploited since the deposition profiles are only dependent on the deposition mechanism, not the materials. In the case of the ALD depositions, multiple materials could be used to create a multi-layered structure inside the etched trough of the grating. If the correct layer thicknesses and refractive indices can be achieved, a DBR-like stack may be made allowing field placement at the resonance condition.

Furthermore, the devices could be designed to work at diffractive orders of $m \neq 0$, allowing phase to be encoded into the reflected spectra as well. Moreover, the grating geometry could be changed to incorporate polarization selectivity. In doing so, the major characteristics of a source beam – wavelength, amplitude, phase, and polarization – could be controlled in a single device.

The power of the encapsulation and bonding scheme becomes apparent when applied to optically polished, flat substrates. The ability to bond optical fibers or ferules to a wafer substrate permits the resonant components to be used in optical fiber systems, independent of free space alignment schemes. Similarly, wafer-to-wafer bonding can create a single multi-functional device while eliminating the need for free-space alignment between separate devices in a single optical arrangement.

APPENDICES

Appendix A

Fabrication Methods

A.1 Introduction

During initial device simulation, necessary dimension and material properties may be fine-tuned to ensure the parameters lay within the fabrication space of the available lithography tools. In practice, limitations on fabrication, device testing, and material systems should be considered during simulation process. Each step in the process is coupled – limitations caused by one parameter may be somewhat relieved by alterations in another parameter. To understand the influence of each parameter, characterization is essential to the success, repeatability, and flexibility of a lithographic process. The microfabrication process described here focuses on wafer-sized fabrication. The construction of a general device is discussed for each step, applicable to the inverted and encapsulated structures alike. This discussion of the fabrication process covers the substrate preparation through pattern etching; deposition is not included, since the two deposition methods (PECVD and ALD) are discussed in the preceding chapters.

A.2 Substrate Preparation

Prior to device fabrication, wafer substrates will be immersed in a cleaning solution. One method is to use a "piranha etch." In this case, a 2:1 mixture of sulfuric acid (H_2SO_4) to hydrogen peroxide (H_2O_2) is used, creating a $H_2SO_4 + H_2O_2 \rightarrow H_2SO_5 + H_2O$ reaction. The piranha solution is highly volatile; the

strong exothermic reaction and dissolving properties of the chemical agents, dissolving organic materials (ex. photoresist, contaminants) on the immersed surfaces. Allowed to set, the strong reaction dissipates over a number of hours prior to disposal. Similar processes are available using automated tools. Alternatively, a stable photoresist remover may be used such as Nanostrip, NMP (1-Methyl-2-pyrrolidinone), or solvents such as isopropanol or methanol.

To promote adhesion of the photoresist to the wafers' surface, a priming agent is subsequently applied. A straight-forward time efficient method to do this is to use SurPass 3000 cationic priming agent, which provides a monolayer of dangling bonds on the wafer surface for the photoresist molecules to catch [62]. A longer, less effective method is to utilize an HMDS vapor priming oven. Oven priming utilizes programmed exposure to a heated and dehydrated atmosphere, eliminating the water absorbed from the air on any present long range hydrogen bonds [79].

A.3 Photoresist Application

With the wafer surface primed, photoresist may be applied. During the application process, the wafer is spun at a high rotational velocity to ensure uniform coating across wafer. The rotational velocity is an important factor determining the thickness of the photoresist on the substrate; as shown in Fig. A.1, the thickness scales asymptotically with spin speed, and is affected by the viscosity of the resist. While many different types of photoresists are used, this discussion will focus on the non-amplified resist commonly used for g-line and i-line exposure tools.

OiR-620, SPR-700 1.2, and SPR-220 3 photoresists were spun on UV-grade fused silica substrates; thickness was characterized on a Rudolph FTM ellipsometer tool following a post-applied bake (PAB) at 90 °C for 120 sec. Additionally, S1813 and AZ MiR 701 photoresist were spun onto similar substrates. In the analysis of these resists, depths were determined by exposing open, 1 mm wide metrology boxes in the photoresist with parameters that allowed photoresist to be completely removed from the exposed areas. After a development process, a profilometer was used to find the depth of the boxes.

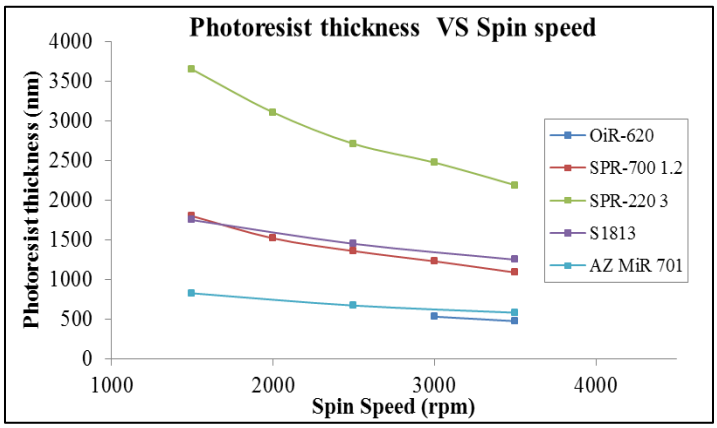

Fig. A.1 Photoresist thickness is shown as a function of spin speed for multiple photoresists. All substrates were fused silica. Data was taken after a post applied bake of 115 °C for 60 seconds.

The thickness of the resist plays an important role during the pattern exposure process – this parameter strongly affects the critical dimension (CD) and the dose-to-clear of the photoresist. The critical dimension is the smallest printable feature using the exposure system at hand; the dose-to-clear represents the required temporal length needed to clear the photoresist from the patterned area. The energy incident on the photoresist varies sinusoidally with a change in resist thickness; the resulting plot, or

"swing curve", is a function of the sinusoidal variation of reflectivity from the substrate. In turn, this variation is caused by the interference of the electric field inside the photoresist. An example swing curve is shown in Fig. A.2 for AZ MiR 701 photoresist, from Fig. B1 [75].

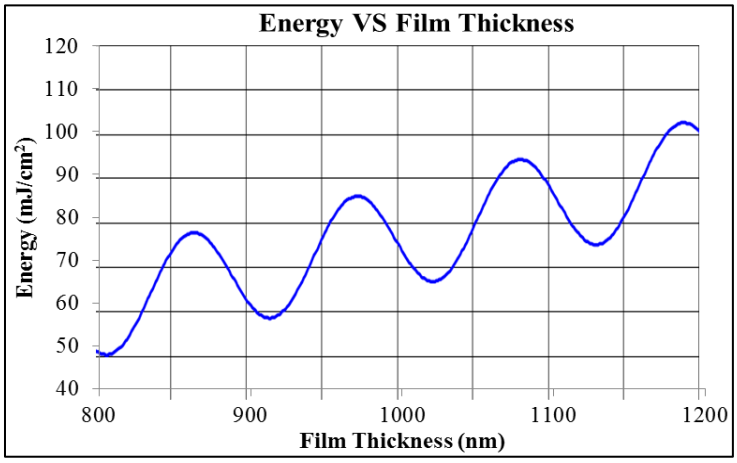

Fig. A.2 The "swing curve" is shown for AZ MiR 701 photoresist. Energy is plotted versus the film thickness.

The interference of the electric field occurs because the top and bottom interfaces of the photoresist layer will act as partial reflectors, unless an antireflection coating is placed at either interface. The reflections cause a standing wave to occur within the coating during the exposure process. The standing wave pattern is a function of the thickness and refractive index of the resist. The amplitude of the standing wave in the photoresist can be reduced by the aforementioned AR coatings, or by increasing the absorption in the photoresist by adding a dye [80]. Similar to the photoresist, liquid AR coatings are available that may be spun to yield a desired thickness. The amplitude of the swing also provides an indication of the how much of a problem the resist thickness has

become. The “swing ratio” is determined by the amplitude difference between two points on the swing curve, separated by one period. The larger the swing ratio, the larger effect the resist thickness has on the process.

A.4 Post-Application Bake

Following application of the photoresist, the substrate and applied photoresist are baked. Referred to as a “post-applied bake”, or PAB, dries the photoresist and removes excess solvent. Solvent removal impacts the photoresist in four distinct ways [80]. First, the thickness of the photoactive film is reduced and the film becomes durable against long wait periods prior to exposure. With the change in thickness, the subsequent steps in the exposure and development process are also changed. Third, the adhesion is improved between the photoresist and the substrate. Lastly, the film becomes less prone to contamination by particles in the atmosphere. In the work presented here, typical PAB processes are done at 115 ℃ for 60 sec. However, the high temperature may cause the photosensitive component to degrade and absorb less of the incident exposure.

A.5 Pattern Exposure

In order to imprint a pattern in the photoresist, many mature lithography techniques have become available, including contact lithography, proximity lithography, projection lithography, and direct laser writing. In contact lithography, a resist-coated wafer is brought into intimate contact with a patterned photomask. While the mask is held by vacuum on a chuck, the wafer is brought into contact with the mask via a piston.

Once contact is made, ultraviolet light illuminates the photomask; light that passes through transparent portions of the mask will interact with the photoresist, allowing it to be developed at a later step. Photoresist beneath the opaque portions of the photomask will receive no light, and will develop differently than the exposed regions. Since the mask and the wafer are brought into contact, the feature size is not limited by diffraction due to the lack of free-space propagation, and extremely high resolutions may be reached [71]–[73]. However, defects on the mask or substrate will also show up in the imprinted photoresist. An illustration of the contact photolithography process is shown in Fig. A.3.

Alternatively, proximity lithography utilizes similar principles, but the layout of the tool incorporates a small separation distance between the photoreticle and the photoresist-coated wafer of ~10 μm [81]. Due to this separation, the coated wafer never comes into contact with the lithography mask, resulting in a lower number of defects being transferred from the mask into the photoresist during patterning. However, this is traded for loss in resolution due to diffraction over the wafer/mask separation. Generally, the resolution of these systems is a function of the wavelength (λ), separation between the mask and wafer (s), and the thickness of the photoresist (z). This relationship is given by: $R = \frac{3}{2}\sqrt{\lambda(s + z/2)}$.

Given an exposure wavelength of 436 nm with a 1 μm thick coating of photoresist, contact lithography $(s = 0)$ yields a resolution of 700.3 nm, while similar settings with proximity lithography $(s = 10\ \mu\text{m})$ yields a resolution of 3.21 μm. feature sizes described in chapter 2 could only be obtainable using contact lithography. To

achieve higher resolution, smaller wavelengths are used as the exposure source. In the extreme case, X-rays are used, with photomasks made of different materials to avoid mask deformation [82].

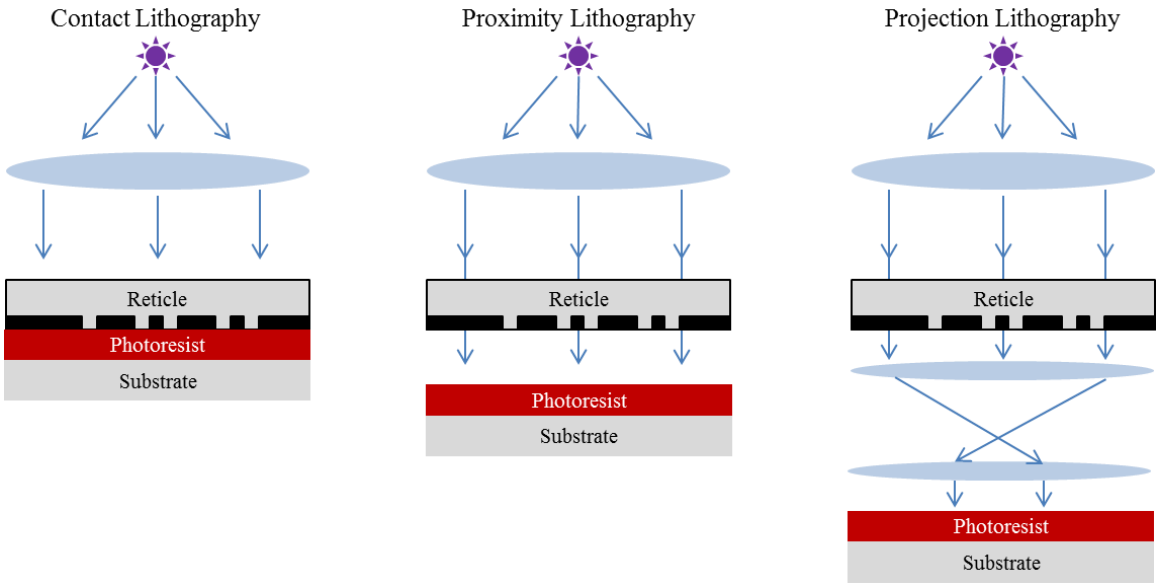

Fig. A.3 Basic illustration of light propagation through contact, proximity, and projection lithography systems.

A third type of lithography printing is projection lithography. In this technique, UV light is emitted from a gas-discharge lamp and passes through a regiment of optical components to before passing thought the reticle as a collimated beam. Once the reticle pattern is encoded into the illumination, an additional lens column reduces the mask image significantly to provide a smaller footprint on the coated wafer. Of the spectrum emitted from the discharge lamp, a single emission line is chosen to pass through the optical system. Most commonly used are the emission lines from a mercury lamp – these include the g-, h-, and i-lines at 436 nm, 405 nm, and 365 nm respectively. Shorter wavelength deep-UV systems utilize an Excimer laser to produce light at 193 nm [83].

For this discussion, an i-line stepper tool will be exemplified; an illustration of a projection tools' optical path is shown in Fig. A.4.

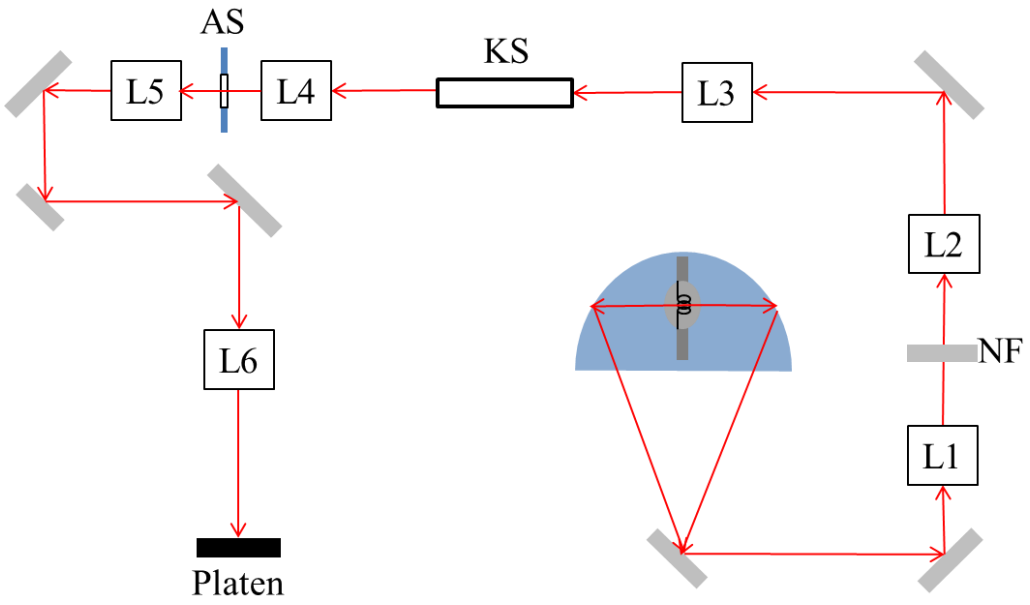

Fig. A.4 The light path for the i-line projection photolithography system is illustrated. L1 – L6 represent various lens systems; KS represents a kaleidoscope, and AS represents the aperture stop.

Light from a gas-discharge mercury lamp is emitted, collected, and reflected to the first lens system, L1. The broad spectrum is then passed through a narrowband spectral filter (NF) before passing through the second and third lens systems, L2 and L3. Light continues into the Kaleidoscope (KS), which homogenizes the light to remove any defects in the beam profile. Light passes through lens system L4 before encountering the aperture stop (AS). Apertures may be placed in the aperture stop to modify the illumination profile. By changing the geometry of the aperture stop, the amount of energy reaching the apodization plane can be varied. Furthermore, the geometry of the aperture stop affects the critical dimension of the exposed pattern.

Continuing through a fifth lens system (L5), the illumination reaches the apodization plane (AP) where the intensity and profile may be modified. Since the field has yet to pass through the reticle, an additional lithography reticle may be inserted to alter the illumination profile since the mask in the apodization plane is not resolvable. Light is then passed through the computer-controlled shutter; the time the shutter is open during an exposure is programmable by the user to allow the optimal amount of energy to reach the photoactive compound. Finally, the light passes through the lithography mask; the computer-generated pattern is often represented as a transparent pattern in the chrome layer, coated on a fused quartz mask. When the shutter opens, light passes through gaps in mask, propagating through the final lens column, L6. Here, the pattern is reduced by 5X and focused onto the photoactive layer. The light then strikes the photoresist, changing its solubility and chemistry to change, inducing cross-linking between polymers in the photoresist.

The minimum printable feature size is a function of the incident wavelength, the k_1 factor, and the numerical aperture of the lens system [84], described as $CD = k_1 \frac{\lambda}{NA}$. Therefore, the shorter wavelength exposure tools are able to create features with increasingly smaller dimensions. The critical dimension can also be improved by increasing the numerical aperture of the lens system. This can be done by increasing the focal length of the lens system or decreasing the diameter of the entrance pupil, but this can be costly in terms of the weight and size of lenses. k_1 is a constant, dependent on the

fabrication process. This is limited by the necessity of the first diffracted order to be transferred through the optical column to the optical system.

However, if the NA of a lens system is increased to provide a smaller CD, the depth of focus of the system is lost. As shown above, the depth of focus decreases quicker than the critical dimension for a similar wavelength. Similar to k_1, k_2 is process-dependent and typically has a value close to k_1. The depth of focus is given by: $DOF = k_2 \frac{\lambda}{NA^2}$.

As explained by L. R. Harriott, a reduced depth of field severely decreases tolerances on the fabrication process [84]. A reduced depth of focus also places limits on the thickness of the photoresist. Ideally, the depth of focus of the optical system should be larger than, or equal to the thickness of the resist; in this case, a focused pattern will be imaged through the entire resist layer. If the depth of focus is shorter than the resist thickness, non-ideal sidewalls can be obtained that will transfer poorly into the substrate.

In order to determine the best parameters for any combination of photoresist and exposure pattern geometry, a focus-exposure matrix is exposed. Since the clarity and dimension of the exposed pattern are a function of focus and exposure, methodically exposing an array of varying foci and exposure times for a given mask will reveal information as to which parameters give the best result. A sample FEM layout is illustrated in Fig. A.5, and was used to find optimal parameters for a hexagonal grating pattern. Blue "X" marks denote the die examined under an SEM. The FEM varied exposure times between 0.25 and 0.65 seconds in increments of 0.5 seconds, with varying

values of focus between -12 and +12 in increments of +3. Each unit increment in focus is one tenth of a micrometer. FEM results taken from a scanning electron microscope are in Fig. A.6 and Fig. A.7. In the following discussion, variations in focus are grouped together, as are variations in exposure dose; this is done for clarity of discussion.

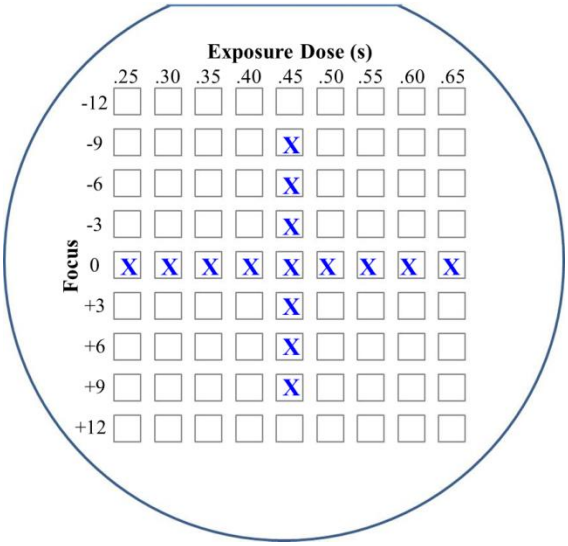

Fig. A.5 Sample parameters are illustrated for an exposed FEM.

First, the profile of hexagonal grating is examined as the value of the focus offset is increased. As shown in Fig. A.6, an increase in the focus offset corresponds to a greater distance above the surface of the photoresist. Furthermore, the focus can only be increased or decreased in increments of 1; this corresponds to a change of 0.1 µm in the proper direction.

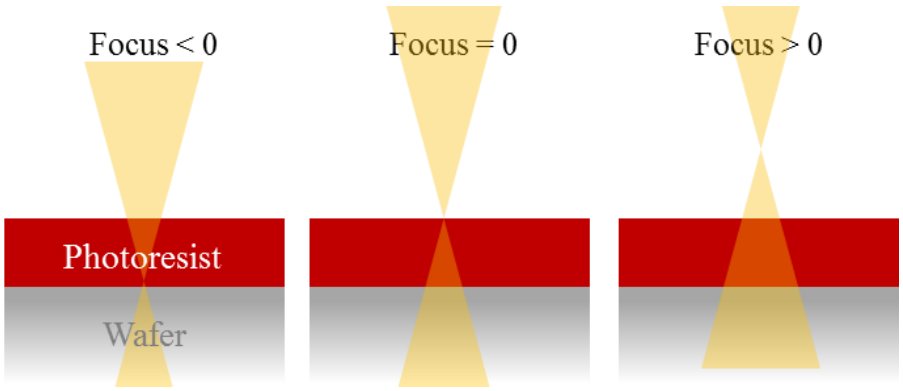

Fig. A.6 The progression of the focal point through the surface of the photoresist is illustrated.

The change in focus offset manifests in the photoresist as a dimension change in the exposed features. This can be seen by comparing the subsequent images of Fig. A.7. As the focus offset moves between $f = -6$ and $f = +6,$ the central holes are seen to widen until $f = 0,$ when the focus is at the top of the photoresist. After this point, the central hole becomes smaller. This occurs because the improper focus causes the sidewalls to become non-vertical, creating a V-shaped cone in the photoresist. As the focus continues to go deeper into the photoresist, the diameter of the inner holes begins to widen because the incident beam has a greater diameter.

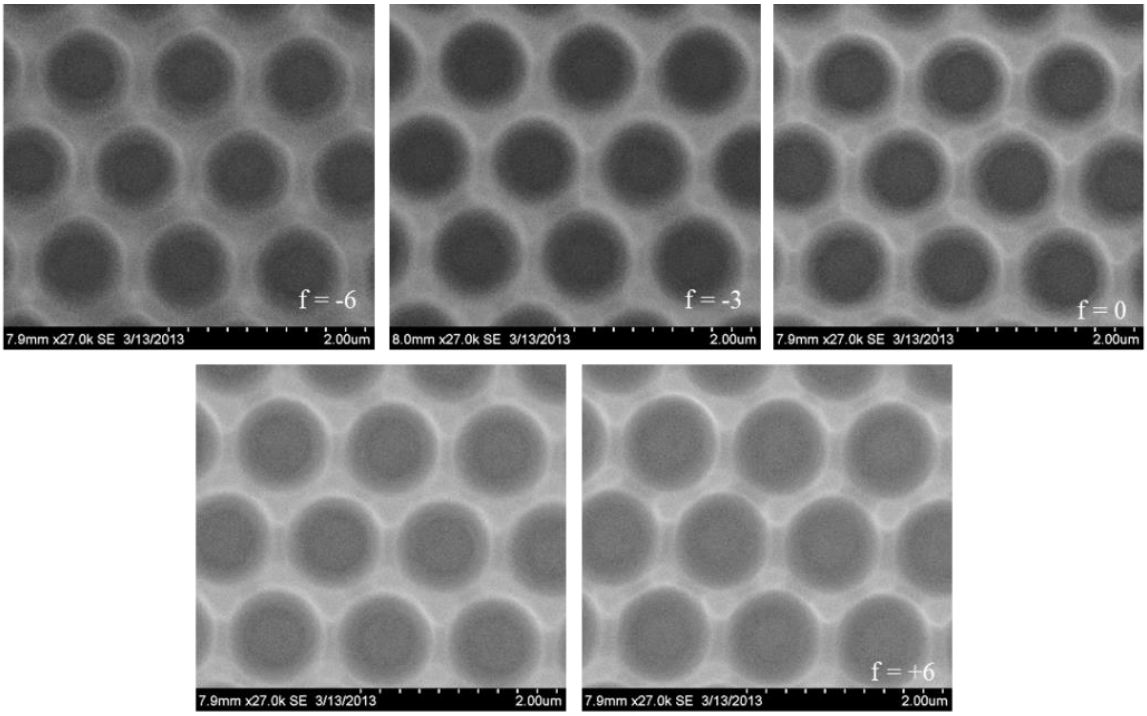

Fig. A.7 Top-down SEM images of a hexagonal grating, exposed with varying focus offsets. The focus used during the imprinting step is given in the lower right hand corner of the image. The bottom portion illustrates the progression of the focal point into the photoresist.

In a similar manner, the effect of an increased exposure time is examined. Fig. A.8 illustrates the increase in energy going into the surface, where $t_1 > t_2 > t_3$. As the illumination bombards the photoactive compound, more energy enters the photoactive compound, pushing the image deeper into the photoresist and widening the features. The end result is shown in the SEM results of Fig. A.9.

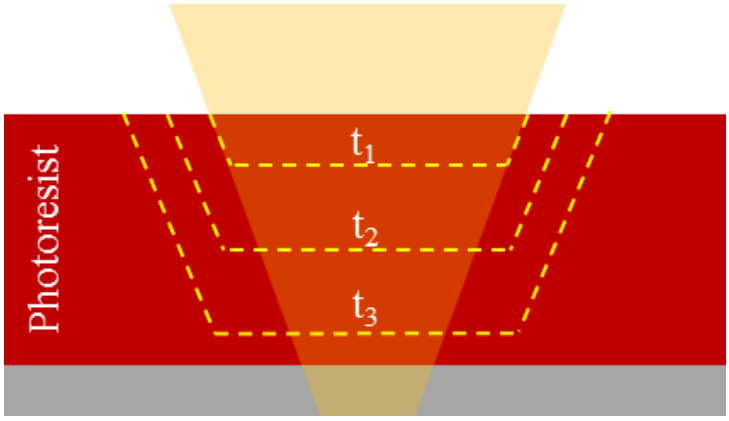

Fig. A.8 The effect of an increasing exposure dose is illustrated.

At exposure time $t = 0.25$ seconds, no central opening is seen in the photoresist because the amount of energy placed into the photoresist is not enough to reach the surface. At $t = 0.35$ seconds, a central opening becomes visible, indicative of the top of the substrate. As the exposure time increases, the central opening continues to widen, eventually reaching a similar diameter as the top of the grating.

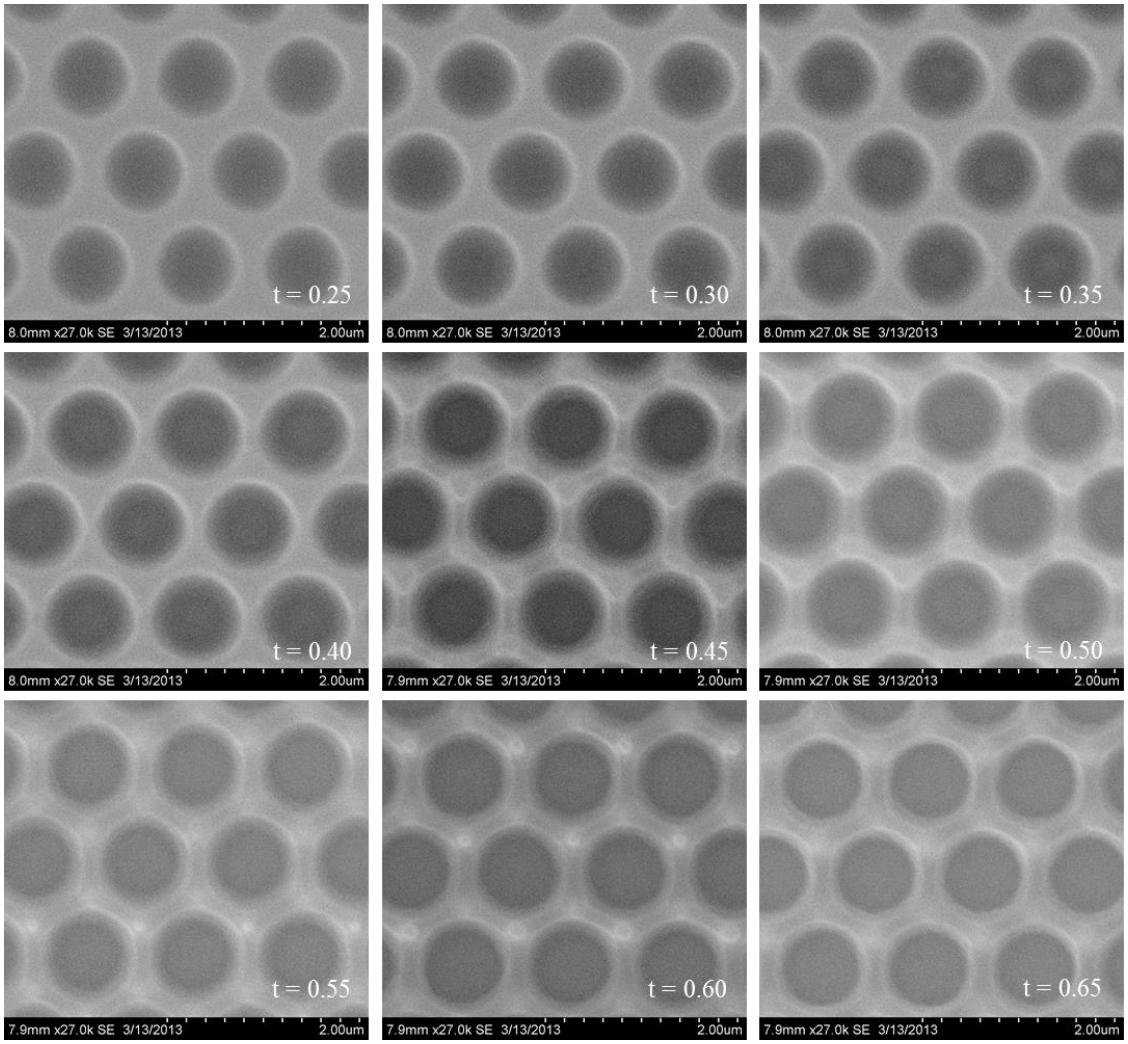

Fig. A.9 Top-down SEM images of a hexagonal grating, exposed with varying exposure times. The exposure time used during the imprinting step is given in the lower right hand corner of the image.

A second indication of the widening holes can be seen in the diameter of the exposed holes, as well as the webbing between them. At $t = 0.25$ seconds, the holes of the hexagonal grating a separated, and the space between them appears to be smooth. At $t = 0.45$ seconds, bright lines begin to appear on the walls between the holes; this is an indication that the holes of the hexagonal grating have merged, at the top, and are no

longer separated. To mitigate this, a better combination of exposure dose and focus offset may need to be sought after.

A.6 Post-Exposure Bake

Following the pattern exposure, a post-exposure bake (PEB) is performed to increase the diffusivity of byproducts created during the exposure. The solvent content in the resist directly effects the acid diffusion in the resist, in turn altering the profile of the standing wave pattern. Increased solvent content leads to increased acid diffusion, leading to greater smoothing of the standing wave pattern. Since both PAB and PEB alter the amount of solvent in the resist, optimum PEB settings is a function of the PAB parameters. In the previous device fabrication, both PAB and PEB processes were done with the same time and temperature values to promote solvent diffusion within the photoresist. Other studies have shown that similar bake temperatures with substantially longer bake times (~10 minutes) also show decreased standing wave amplitudes [85]. This occurs due to a 'reflow' effect on the resist. Furthermore, the post-bake step anneals the patterned photoresist and increases the hardness of the film in preparation of subsequent fabrication processes [81].

A.7 Development

The baked and exposed wafers are then developed with the appropriate development solution. During the development stage, the latent image that is formed during the exposure step is converted into a relief image by dissolving and carrying the

exposed resist out of the pattern. Although different methods of development exist, an immersion development process was used, submerging the exposed wafer in a liquid developer solution for a set time. After being rinsed (deionized water) and dried (nitrogen), a developed structure in photoresist remains that can be used as an etching mask subsequent processing steps. With the foresight that an etch ratio will exist between the photoresist and the substrate -- one will etch faster than the other at a known rate -- a more sturdy etch mask may be desired.

A.8 Etching

With a patterned mask in place, an etching step is used to transfer the pattern into the substrate or subsequent layers. Generally, two etching techniques are used: wet and dry etching. The choice of one technique over the other may be based on etch selectivity, etch rate, or the substrate material.

Isotropic and anisotropic wet etch techniques have been developed for a number of materials. As indicated by the names, the different techniques yield different etch profiles; this is illustrated in Fig. A.10. While most wet etch processes tend to yield an isotropic etch, anisotropic wet etch techniques have been developed for silicon [86] and germanium [87] due to their demand in microelectronic systems. In the case of the inverted hexagonal GMRFs, a pattern may be exposed on a chrome-coated wafer prior to being transferred into the chrome layer via wet etch. By incrementally monitoring the light transmitted through the backside of the wafer, a complete and successful chrome etch can be realized when the desired pattern is transmitted unbroken. This process was

used in the fabrication of the inverted hexagonal structures, shown in Fig. 2.26. It is also worth noting that the subsequent etch into glass could be realized via wet etch by immersing the wafer in buffered oxide etch (BOE), containing hydrofluoric acid [88].

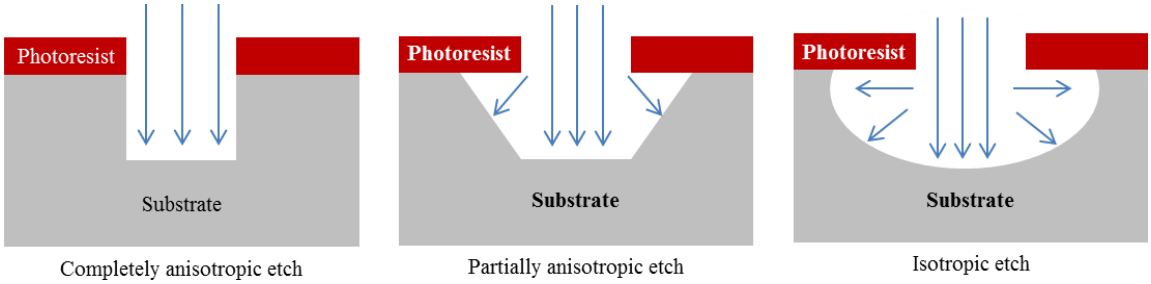

Fig. A.10 The differences between anisotropic, partially anisotropic, and isotropic etches is illustrated.

Alternatively, plasma processes allow for high selectivity etches while preserving the fidelity of the etch mask [89]. Based on their anisotropic etching mechanism, plasma etches lead to high aspect ratio structures while maintaining the feature sizes of the etch mask. During a typical plasma etch, patterned photoresist acts as the etch mask, offering low etch selectivity when compared to a "harder" etch mask. For this work, the etch selectivity between photoresist and fused silica was roughly 1:1.8; that is, for every 1 µm of resist that is etched away, 1.8 µm of fused silica will be removed from the exposed areas. This is in contrast to the 1:10 etch selectivity between chrome and fused silica. This can be overcome by increasing the thickness of the photoresist during the fabrication process, but it becomes increasingly difficult to pattern fine features in thick resists. This would require longer exposure times to place sufficient energy into the photoresist to achieve a proper dose-to-clear; as illustrated in Figs. B8 and B9, this can lead to degradation of the pattern.

Different configurations of dry etching systems typically utilize chemical plasma etching (PE), reactive ion etching (RIE), or physical ion beam etching (IBE) [90], [91]. For this work, an ICP RIE etcher was used to execute the transfer etch of the inverted and encapsulated grating structures.

For all etching systems, the etch rate, anisotropy, selectivity, and etch uniformity are indicative of the etch quality. By varying these parameters, changes in the etch rates of the substrate and etch mask may be monitored to achieve repeatable etch recipes and trends [92]. This study compared the etch rates of a patterned chrome etch mask and the underlying silica substrate as a function of gas chemistry, RIE power, ICP power, gas flow rate, and chamber pressure. The three different gas chemistries used were C_2F_2-CO_2, CHF_3-Ar, and C_4F_8-O_2. As a general trend, the etch rate of the substrate increased with an increase in RIE power and ICP power, while an increase in gas flow did not affect the etch rate significantly. An increase in pressure was seen to decrease the substrate etch rate in the cases of C_2F_2-CO_2 and C_4F_8-O_2. The etch rate of the chrome etch increased with an increase in RIE power, but consistently decreased with an increase in ICP power. Similar to the silica, an increase in the flow rate of the active gas (C_2F_2, CHF_3, and C_4F_8) did not result in a significant change in the etch rate of the chrome mask. Finally, the etch rate of the chrome mask was seen to consistently increase with an increase in the chamber pressure.

For the plasma system used in this study, a gas chemistry of CHF_3-O_2 was used with an ICP RIE Unaxis Versaline plasma etcher. Previously, an extensive characterization of the impact of each etch parameters has been completed along with a

discussion of the functionality of the tool [89]. From these results, the following table has been created which details some of the etch recipes used in this work. The parameters for five recipes are given along with their respective etch rates that include 0.8:1 – 1.8:1 etch selectivity. The "FS_descum" recipe does not utilize CHF_3, and thus does not etch glass. Instead, it is used prior to the etch in to remove organic debris to prevent micro-masking, as well as after the transfer etch to remove remaining resist from the surface of the wafer.

Recipe Name	CHF_3 (sccm)	O_2 (sccm)	ICP Power (W)	RIE Power (W)	D	Etch Rate (FS:Resist)
FS_08	40	10	750	75	10	0.8 : 1.0
FS_1	65	5	625	50	10	1.0 : 1.0
FS_1805_etch	70	5	500	50	10	1.3 : 1.0
FS_15	70	6	800	40	10	1.5 : 1.0
FS_18	70	2	800	40	10	1.8 : 1.0
FS_descum	-	20	100	50	10	-

Table A1. The etch parameters are shown along with their measured etch rates for an RIE ICP etcher.

A.9 Deposition

Lastly, additional layers may be added to a device in order to provide an additional etch mask, waveguide, or grating layer. Though many deposition techniques exist, two methods that were used in this work will be discussed: Plasma Enhanced Chemical Vapor Deposition (PECVD) and Atomic Layer Deposition (ALD).

PECVD is a deposition technique which utilizes multiple gasses (SiH_4 and N_2O) to combine in a chamber [93]. A current is driven between a top and substrate electrode, allowing a plasma to form in the chamber with the reactive gases. Once the gasses react,

SiO_2 deposits in a top-down manner at a rate of 48 nm/min. The deposition rate is known to vary with the substrate material, the applied power, gas chemistry, and other deposition variables. An illustration of the PECVD layout is shown in Fig. A.11 [93]. Due to the top-down nature of the deposition, a lengthy deposition process can lead to the formation of air holes in high aspect ratio gratings as shown in Fig. 3.11.

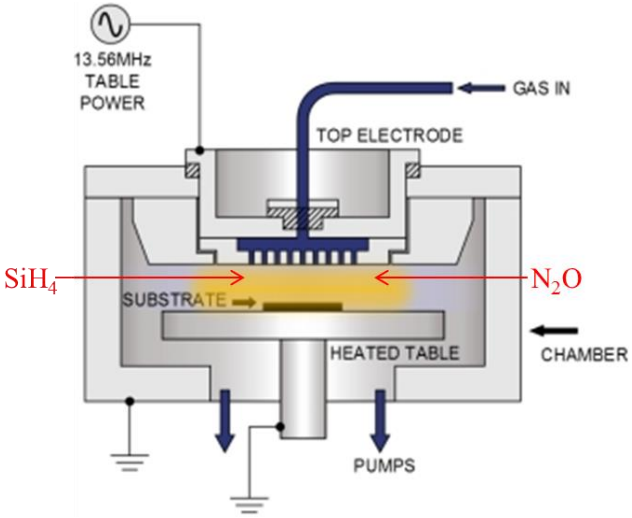

$$SiH_4 + O_2 \rightarrow SiO_2 + 2H_2$$

Fig. A.11 The layout of the process chamber of a PECVD tool is illustrated.

The PECVD technique can be used with high- or low-frequency mixing to exercise control over stress of the deposited film. A broad range of materials may be deposited, ranging from Silicon oxide, silicon nitride, amorphous silicon, and even diamond-like carbon [93]

Alternatively, a conformal deposition may be achieved if an ALD process is employed. In contrast to the top-down PECVD technique, ALD tools typically deposit metal oxides (Al_2O_3, TiO_2, HfO_2). The atomic nature of the deposition allows for < 5% variation thickness across the wafer, while avoiding air pocket formation. In doing so,

grating trenches are completely and evenly filled in. An illustration of the ALD chamber and a single cycle of the deposition is shown in Fig. A.12.

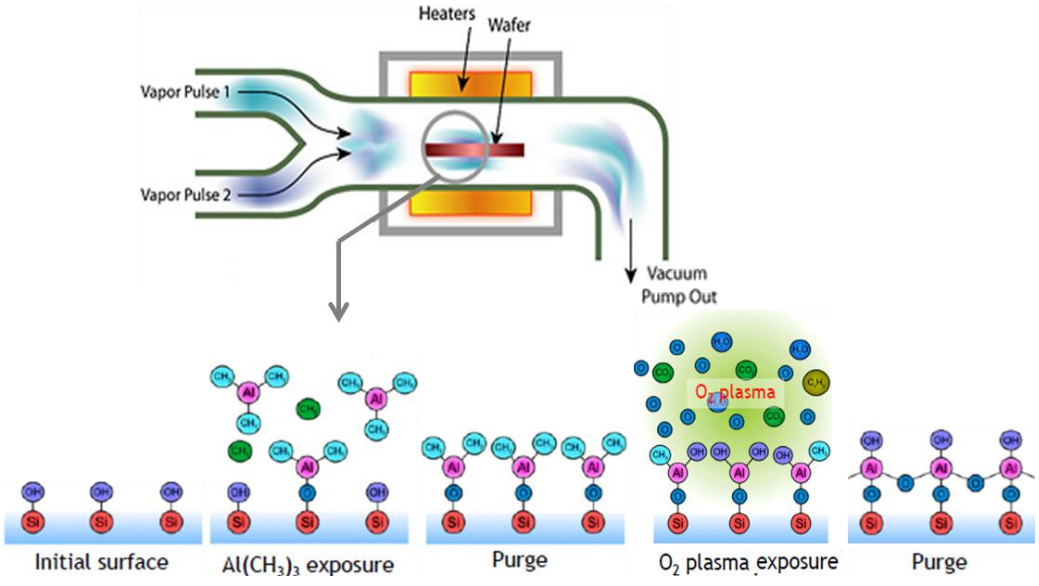

Fig. A.12 The layout of the process chamber of an ALD tool is illustrated along with the stages of a single ALD deposition cycle.

In the presented work, a Trimethyl Aluminum precursor was used; the naturally high vapor pressure allows the TMA to be drawn into the chamber and attach to the surface of the wafer. Following an Argon purge, the oxygen plasma is introduced; the plasma interacts with the TMA to form an atomic layer of Al_2O_3. A second purge removes the excess gasses from the chamber and completes the ALD cycle. A typical cycle takes ~5 seconds to complete, resulting in a deposition rate of 0.122 nm/cycle. The atomic nature of the deposition leads to the conformal aspects that become key in fabricating the encapsulated structures.

Appendix B

High Power Testing / Finite Beam Width Analysis

B.1 High Power Testing

The experiment in Fig. 3.11 may be modified by changing the location and characteristics of the lens combination in the collimating optics. Instead of collimating the beam, different lenses (f = 8 mm and f = 40 mm) were used to focus the beam down to a very small beam waist $\left(1/e^2 = 89.29\ \mu\text{m}\right)$; by measuring the transmitted power at the same location, the power density of the beam may be obtained – ensuring that the measurements are taken at the same location is not trivial. The altered experimental layout is illustrated in Fig. 3.14.

Prior to inserting the wafer, the beam profile is measured using knife edge KE_1. The power exiting the lens system is measured on power meter PM_1. As the knife edge progressively blocks the beam, the power that reaches PM_1 will drop off, as seen in Fig. 3.13.

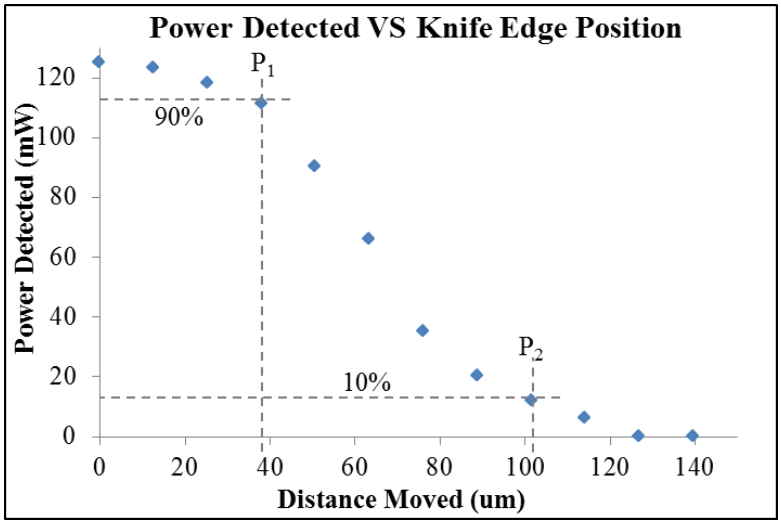

Fig. B.1. Detected power is plotted versus knife edge position for a knife-edge measurement.

Assuming a Gaussian beam, the $1/e^2$ width may be easily calculated [94] from equation (B.1), where X_{10-90} represents the lateral distance the knife edge traveled between 90% and 10% power transmission (indicated on Fig. 4.1), and can be calculated by $X_{10-90} = P_2 - P_1$. The beam radii in the X direction is represented by ω_x. Due to the Gaussian symmetry, this is also indicative of the beam radii in the Y direction. For nonsymmetrical beams, knife edge measurements along both X and Y are required at the same spatial location.

$$X_{10-90} = 1.28\omega_x \tag{B.1}$$

The beam (green arrows) enters the system from the right; it is then collimated and focused with the lens system. The beam is focused onto the wafer (marked "wafer"). Transmitted power measurements are detected with power meter PM_1. The resonance is obtained when the angle of incidence on the wafer is $\theta_i = 7.7°$, meaning the resonant beam will be reflected at $\theta_r = 15.4°$. Due to the short focal length of the lens system, the

reflected beam cannot exit the experiment due to spatial constraints. For this reason, broadband mirror M_1 is used to reflect the resonant beam onto power meter PM_2. Using this technique, a power density of 244.1 kW/cm^2 was obtained at the maximum output for the laser amplifier.

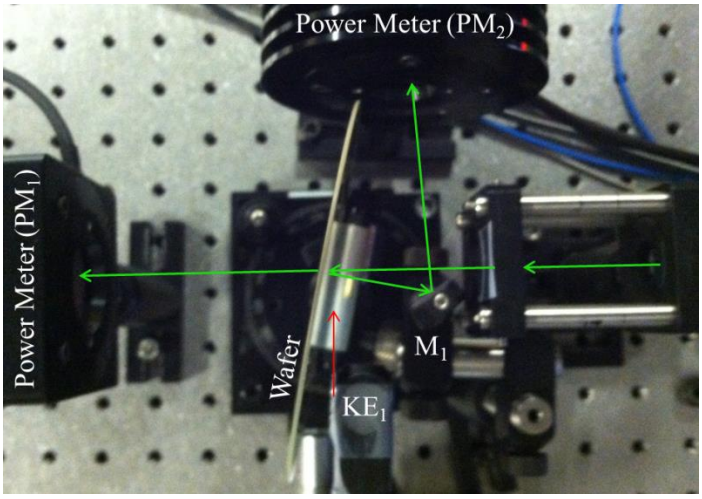

Fig. B.2. The layout of the experiment is shown for testing wafers at high power.

B.2 Finite Beam Width Analysis

Although high power densities may be obtained using a focused beam, the performance of the resonance suffers. As the width of the beam incident on the resonant gratings decreases, a lower number of periods are illuminated; the measured diameter of the focused beam only illuminates ~93 periods. The effect of the finite beam sizes on resonant optics is well understood [95]–[97]. A beam of finite width is similar to one passing through a circular aperture. The angular spread of a beam through a circular aperture is given as equation (B.), where λ is the incident wavelength and D is the diameter of the aperture.

$$\Delta\theta \approx \lambda / D \tag{B.2}$$

Upon diffracting through the aperture, the bandwidth of the diffracted wave is described by equation (B.3); solving for the spread in the wave vector yields equation (B.4).

$$\Delta k \Delta x \geq 2\pi \tag{B.3}$$

$$\Delta k \geq 2\pi / \Delta x \tag{B.4}$$

where $k = \sqrt{k_x^2 + k_y^2 + k_z^2}$, and each component is defined as $k_x = k \sin\theta$. Through algebraic manipulation, the angular spread of the beam is found to be related to the wavelength and beam width by equation (B.5).

$$\sin\theta \approx \frac{\lambda}{\Delta x} \tag{B.5}$$

This implies that a finite width in the beam diameter can be described as an angular spread in the incident beam. Simulations can be used to predict the reflection spectra of the resonant device at each angle included within $\pm\theta/2$. Fig. 4.3 illustrates the relationship of the angular spread to the incident beam diameter. As the beam diameter increases, the associated angular spread is seen to decrease asymptotically. In turn, this will increase the predicted maximum reflectivity of the device; this is expected, since an increase in the beam diameter illuminates and increasing number of periods. The indicated beam diameters (90 μm, 1000 μm, and 2540 μm) are indicative of experimentally examined beam profiles.

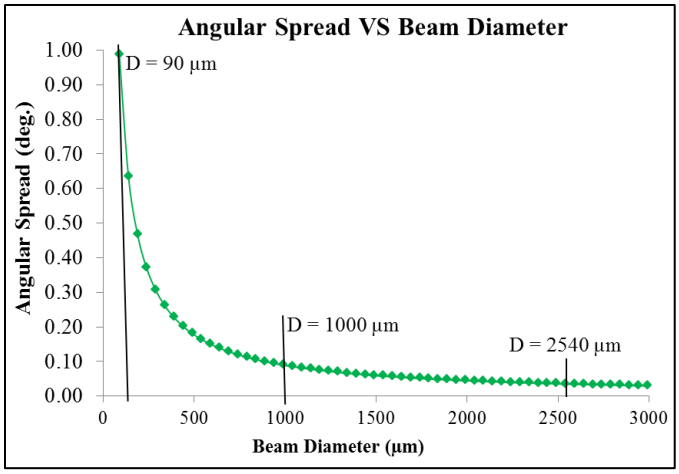

Fig. B.3 The angular spread is calculated versus incident beam diameter.

The final reflectivity of the device can then be predicted by averaging the sum of each of the reflection spectra. Further approximations may be made by using a weighted average instead, weighting the average by the profile of the incident beam. The simulations results, summation, and averaged spectra is shown in Fig. 4.4 and Fig. 4.5. The range of incident angles used in Fig. 3.15 was 7.7° to 8.7° in increments of 0.1°.

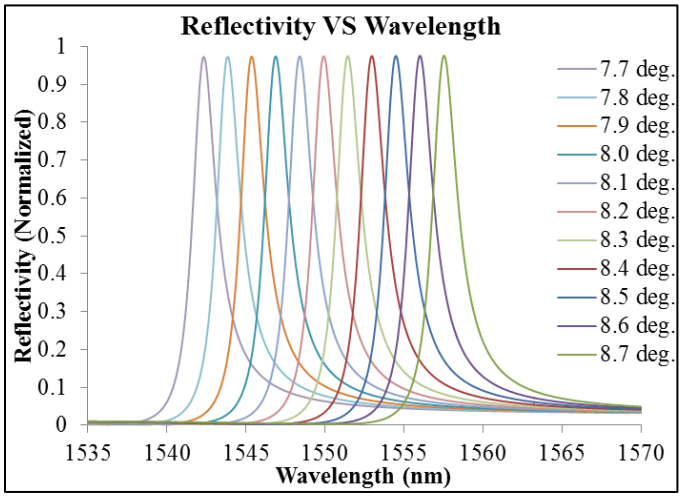

Fig. B.4. Reflectivity is plotted versus wavelength for a range of incident angles.

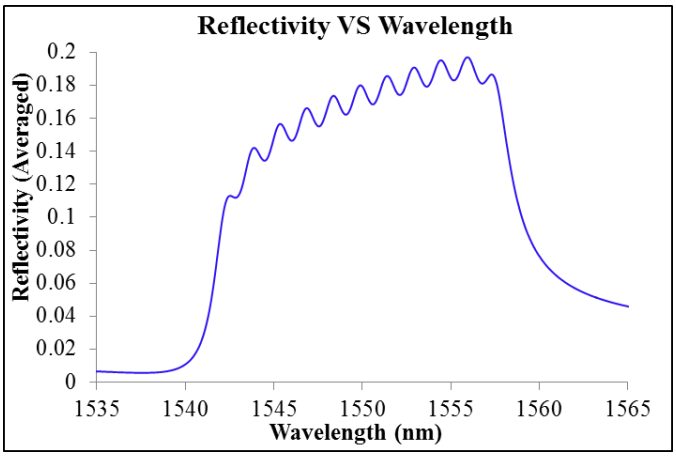

Fig. B.5. The average of reflectivity versus wavelength is plotted for the spectra shown in Fig. 3.16, weighted with a top-hat beam profile.

The results demonstrated in Fig. 4.5 indicate that the maximum reflectivity expected by the resonant devices with a 90 μm incident beam. Assuming a top-hat beam profile, all the values from Fig. 3.16 are averaged with a weight of value of 1. Multiple beam sizes were examined theoretically and experimentally for the device shown in Fig. 3.10(b); a comparison of the theoretical and experimental data is illustrated in Fig. 4.6. If a similar summation were averaged with weighting based on a Gaussian beam, the maximum expected reflectivity would decrease based on the difference in beam shape. Additionally, the width of the beam would the smaller since the Gaussian profile would lead to a decreased FWHM in contrast to the top-hat beam profile.

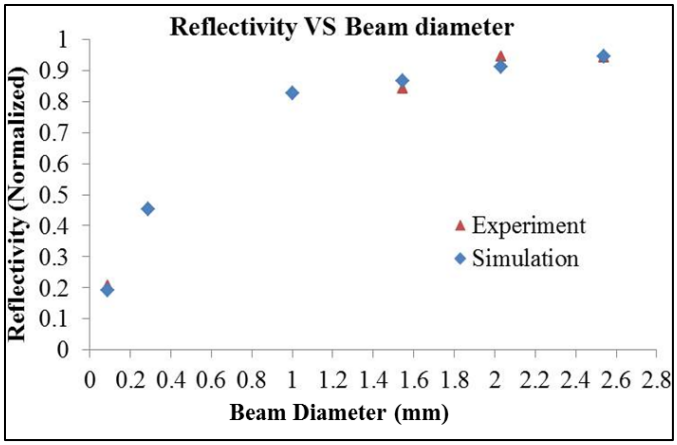

Fig. B.6. Theoretical and experimental reflectivity is compared for various beam diameters.

The finite beam size arises from the need to have a small spot size for light incident on the device; in turn, the small spot size is required in order to obtain high power densities needed to test the thermal and structural integrity of the devices for high energy laser systems.

REFERENCES

[1] R. Paschotta, *Encyclopedia of Laser Physics and Technology*, 1st ed. Wiley-VCH Verlag GmbH & Co., 2008.

[2] C. M. Talbott and R. H. Clifford, "Characterization of Light Emitting Diodes (LEDs) and Compact Fluorescent Lamps (CFLs) by UV-Visible Spectrophotometry," Columbia, MD, 2012.

[3] A. Eintein, "Strahlungs-emission und -absorption nach der Quantentheorie," *Verhandlungen der Dtsch. Phys. Gesellschaft*, vol. 18, pp. 318–323, 1916.

[4] A. Einstein, "Zur Quantentheorie der Strahlung," *Phys. ZS.*, vol. 18, pp. 121–128, 1917.

[5] A. L. Schawlow, "Masers and lasers," *IEEE Trans. Electron Devices*, vol. 23, no. 7, pp. 773–779, Jul. 1976.

[6] J. P. Gordon, H. J. Zeiger, and C. H. Townes, "Molecular Microwave Oscillator and New Hyperfine Structure in the Microwave Spectrum of NH3," *Phys. Rev.*, vol. 95, no. 1, pp. 282–284, 1954.

[7] A. L. Schawlow and C. H. Townes, "Infrared and Optical Masers," *Phys. Rev.*, vol. 112, no. 6, pp. 1940–1949, 1958.

[8] T. H. Maiman, "Stimulated Optical Radiation in Ruby," *Nature*, vol. 187, no. 4736, pp. 493–494, 1960.

[9] L.-H. Xu, R. M. Lees, E. C. C. Vasconcellos, S. C. Zerbetto, L. R. Zink, and K. M. Evenson, "Methanol and the Optically Pumped Far-Infrared Laser.pdf," *IEEE J. Quantum Electron.*, vol. 32, no. 3, pp. 392–399, 1996.

[10] S. F. Dyubko, L. D. Fesenko, A. S. Shevyrev, and V. I. Yartsev, "New emission lines of methylamine and methyl alcohol molecules in optically pumped lasers," *Sov. J. Quantum Electron.*, vol. 11, no. 9, pp. 1248–1249, 1981.

[11] F. Brown, S. Kronheim, and E. Silver, "Tunable far infrared methyl fluoride laser using transverse optical pumping," *Appl. Phys. Lett.*, vol. 25, no. 7, pp. 394–396, 1974.

[12] S. B. Mirov, A. O. Okorogu, W. Lee, D. I. Crouthamel, N. W. Jenkins, K. Graham, A. R. Gallian, A. Y. Dergachev, L. Age, and T. R. Drive, "All Solid State Laser System , Continuously Tunable Over 0 . 2-10 Micron Spectral Range," in

Intenational Conference on Applications of Photonic Technology III: Closing the Gap Between Theory, Development, and Applications, 1998, vol. 3491, pp. 1082–1088.

[13] "Quantronix Diode-Pumped Nd:Yag Lasersnd Hawk-HP Series," Santa Clara, CA, 2013.

[14] D. Schuocker, "A feasible concept for a 100 kW cw CO2 laser based on an existing 6 kW device," in *High-Power Laser Ablation V, Proc. SPIE*, 2004, vol. 5448, pp. 393–403.

[15] M. D. Perry, D. Pennington, B. C. Stuart, G. Tietbohl, J. A. Britten, C. Brown, S. Herman, B. Golick, M. Kartz, J. Miller, H. T. Powell, M. Vergino, and V. Yanovsky, "Petawatt Laser Pulses," *Opt. Lett.*, vol. 24, no. 3, pp. 160–162, Feb. 1999.

[16] R. A. Sims, C. C. C. Willis, P. Kadwani, T. S. McComb, L. Shah, V. Sudesh, Z. Roth, M. Poutous, E. G. Johnson, and M. Richardson, "Spectral Beam Combining of Thulium Fiber Laser Systems," in *Proc. of SPIE: Fiber Lasers VII: Technology, Systems, and Applications*, 2010, vol. 7580, p. 75801Q–75801Q–6.

[17] Y. Li, I. R. Srimathi, R. H. Woodward, A. J. Pung, M. K. Poutous, R. K. Shori, and E. G. Johnson, "Guided-Mode Resonance Filters for Wavelength Selection in Mid-Infrared Fiber Lasers," *IEEE Photonics Technol. Lett.*, vol. 24, no. 24, pp. 2300–2302, 2012.

[18] I. R. Srimathi, M. K. Poutous, A. Pung, Y. Li, R. Woodward, and E. G. Johnson, "Design and Fabrication of Mid-IR Guided Mode Resonance Filters," in *Advanced Photonics Congress (OSA)*, 2012, no. c.

[19] T. Sang, H. Zhao, S. Cai, and Z. Wang, "Design of guided-mode resonance filters with an antireflective surface at oblique incidence," *Opt. Commun.*, vol. 285, no. 3, pp. 258–263, Feb. 2012.

[20] R. A. Sims, Z. A. Roth, C. C. C. Willis, P. Kadwani, T. S. McComb, L. Shah, V. Sudesh, M. Poutous, E. G. Johnson, and M. Richardson, "Spectral narrowing and stabilization of thulium fiber lasers using guided-mode resonance filters.," *Opt. Lett.*, vol. 36, no. 5, pp. 737–9, Mar. 2011.

[21] L. Shah, R. A. Sims, P. Kadwani, C. C. C. Willis, J. B. Bradford, A. Pung, M. K. Poutous, E. G. Johnson, and M. Richardson, "Integrated Tm:fiber MOPA with polarized output and narrow linewidth with 100 W average power," *Opt. Express*, vol. 20, no. 18, pp. 20558–63, Aug. 2012.

[22] W. S. Mohammed, M. Pitchumani, J. D. Brown, and E. G. Johnson, "Polarization converting element for minimizing the losses in cylindrical hollow waveguides," in *Micromachining Technology for Micro-Optics and Nano-Optics III*, 2005, vol. 5720, pp. 212–221.

[23] M. K. Poutous, A. J. Pung, P. Srinivasan, Z. A. Roth, and E. G. Johnson, "Polarization selective, graded-reflectivity resonance filter, using a space-varying guided-mode resonance structure," *Opt. Express*, vol. 18, no. 26, pp. 27764–27776, 2010.

[24] Z. A. Roth, P. Srinivasan, M. K. Poutous, A. J. Pung, R. C. Rumpf, and E. G. Johnson, "Azimuthally Varying Guided Mode Resonance Filters," *Micromachines*, vol. 3, no. 4, pp. 180–193, Mar. 2012.

[25] K. Jia, D. Zhang, and J. Ma, "Sensitivity of guided mode resonance filter-based biosensor in visible and near infrared ranges," *Sensors Actuators B Chem.*, vol. 156, no. 1, pp. 194–197, Aug. 2011.

[26] T.-J. Ding, J.-H. Lue, Y. L. Tsai, T.-H. Yang, J.-Y. Chang, and W.-Y. Chen, "Monitoring DNA Hybridization with a Simply Manufactured GMR Biosensor," *Life Sci. J.*, vol. 9, no. 2, pp. 1–5, 2012.

[27] N. Ganesh, I. D. Block, P. C. Mathias, W. Zhang, E. Chow, V. Malyarchuk, and B. T. Cunningham, "Leaky-mode assisted fluorescence extraction: application to fluorescence enhancement biosensors.," *Opt. Express*, vol. 16, no. 26, pp. 21626–40, Dec. 2008.

[28] D. D. Wawro, P. Priambodo, and R. Magnusson, "Resonating periodic waveguides as ultra resolution sensors in biomedicine," in *Nanoengineering: Fabrication, Properties, Optics, and Devices*, 2004, vol. 5515, pp. 52–57.

[29] E. Sader and A. Sayyed-Ahmad, "Design of an optical water pollution sensor using a single-layer guided-mode resonance filter," *Photonic Sensors*, vol. 3, no. 3, pp. 224–230, Jun. 2013.

[30] M. J. Uddin, S. Member, R. Magnusson, and S. Member, "Efficient Guided-Mode-Resonant Tunable Color Filters," *IEEE Photonics Technol. Lett.*, vol. 24, no. 17, pp. 1552–1554, 2012.

[31] K. J. Lee, S. Member, D. Wawro, P. S. Priambodo, R. Magnusson, S. Member, and A. Abstract, "Agarose-Gel Based Guided-Mode Resonance Humidity Sensor," *IEEE Sens. J.*, vol. 7, no. 3, pp. 409–414, 2007.

[32] J.-N. Liu, M. V Schulmerich, R. Bhargava, and B. T. Cunningham, "Optimally designed narrowband guided-mode resonance reflectance filters for mid-infrared spectroscopy.," *Opt. Express*, vol. 19, no. 24, pp. 24182–97, Nov. 2011.

[33] Melles Griot, "Material Properties." Melles Griot, pp. 4.1–4.24, 2009.

[34] B. Yuan, F. Zhang, and T. Ning, "Relationship between linewidth and electric field intensity of guide-mode resonance filter," *Opt. - Int. J. Light Electron Opt.*, vol. 123, no. 5, pp. 439–441, Mar. 2012.

[35] S. S. Wang and R. Magnusson, "Theory and applications of guided-mode resonance filters," *Appl. Opt.*, vol. 32, no. 14, 1993.

[36] G. Niederer, "Resonant Grating Filters for Microsystems," Institut de Microtechnique, 2004.

[37] D. Griffiths, *Introduction to Electrodynamics*, 3rd ed. Upper Saddle River, NJ: Prentice Hall, 1999.

[38] K. Kawano and T. Kitoh, *Introduction to Optical Waveguide Analysis*. New York, NY: John Wiley & Sons, 2001.

[39] P. Lalanne and M. Hutley, "The optical properties of artificial media structured at a subwavelength scale," pp. 1–11.

[40] M. G. Moharam and T. K. Gaylord, "Rigorous coupled-wave analysis of planar-grating diffraction," *J. Opt. Soc. Am.*, vol. 71, no. 7, p. 811, Jul. 1981.

[41] R. C. Rumpf, "Design and optimization of nano-optical elements by coupling fabrication to optical behavior," University of Central Florida, 2006.

[42] R. C. Rumpf, "Improved formulation of scattering matrices for semi-analytical methods that is consisten with convention," *Prog. Electromagn. Res. B*, vol. 35, no. August, pp. 241–261, 2011.

[43] M. G. Moharam, D. a. Pommet, E. B. Grann, and T. K. Gaylord, "Stable implementation of the rigorous coupled-wave analysis for surface-relief gratings: enhanced transmittance matrix approach," *J. Opt. Soc. Am. A*, vol. 12, no. 5, p. 1077, May 1995.

[44] J. Kennedy and R. Eberhart, "Particle swarm optimization," in *Proceedings of ICNN'95 - International Conference on Neural Networks*, 1995, vol. 4, pp. 1942–1948.

[45] R. Eberhart and J. Kennedy, “A new optimizer using particle swarm theory,” in *MHS’95. Proceedings of the Sixth International Symposium on Micro Machine and Human Science*, 1995, pp. 39–43.

[46] W. Jiao, G. Liu, and D. Liu, “Elite Particle Swarm Optimization with mutation,” in *2008 Asia Simulation Conference - 7th International Conference on System Simulation and Scientific Computing*, 2008, no. 3, pp. 800–803.

[47] Z. Cui and J. Zeng, “A modified particle swarm optimization predicted by velocity,” *Proc. 2005 Conf. Genet. Evol. Comput. - GECCO ’05*, p. 277, 2005.

[48] C. J. R. Sheppard, “Approximate calculation of the reflection coefficient from a stratified medium,” *Pure Appl. Opt.*, vol. 4, pp. 665–669, 1995.

[49] W. Koechner, *Solid-State Laser Engineering*, 6th Revise. New York, NY: Springer Science + Business Media, Inc., 2006.

[50] J. W. Leem and J. S. Yu, “Broadband and wide-angle distributed Bragg reflectors based on amorphous germanium films by glancing angle deposition,” *Opt. Express*, vol. 20, no. 18, pp. 20576–20581, 2012.

[51] S. M. Rytov, “Electromagnetic Properties of a Finely Stratified Medium,” *Sov. Phys. JETP*, vol. 2, pp. 466–475, 1956.

[52] P. Lalanne, “Effective medium theory applied to photonic crystals composed of cubic or square cylinders,” *Appl. Opt.*, vol. 35, no. 27, 1996.

[53] G. Lifante, “Effective Index Method for Modelling Sub-Wavelength Two-Dimensional Periodic Structures,” pp. 72–77, 2005.

[54] P. Lalanne and D. Lemercier-lalanne, “Depth dependence of the effective properties,” *J. Opt. Soc. Am. A*, vol. 14, no. 2, pp. 450–458, 1997.

[55] S. T. Thurman and G. M. Morris, “Controlling the spectral response in guided-mode resonance filter design,” *Appl. Opt.*, vol. 42, no. 16, pp. 3225–3233, 2003.

[56] T. Sang, L. Wang, S. Ji, Y. Ji, H. Chen, and Z. Wang, “Systematic study of the mirror effect in a poly-Si subwavelength periodic membrane,” *J. Opt. Soc. Am. A. Opt. Image Sci. Vis.*, vol. 26, no. 3, pp. 559–65, Mar. 2009.

[57] H. Rathgen and H. L. Offerhaus, “Large bandwidth, highly efficient optical gratings through high index materials,” *Opt. Express*, vol. 17, no. 6, pp. 4268–4283, 2009.

[58] J. Ma, S. Liu, Y. Jin, C. Xu, J. Shao, and Z. Fan, "Novel method for design of surface relief guided-mode resonant gratings at normal incidence," *Opt. Commun.*, vol. 281, no. 12, pp. 3295–3300, Jun. 2008.

[59] A. Pung, M. Poutous, Z. Roth, and E. Johnson, "Fabrication of Low Contrast Homogenous Guided Mode Resonance Filters," *CLEO2011 - Laser Appl. to Photonic Appl.*, p. JTuI24, 2011.

[60] F. Brückner, D. Friedrich, M. Britzger, T. Clausnitzer, O. Burmeister, E.-B. Kley, K. Danzmann, A. Tünnermann, and R. Schnabel, "Encapsulated subwavelength grating as a quasi-monolithic resonant reflector.," *Opt. Express*, vol. 17, no. 26, pp. 24334–41, Dec. 2009.

[61] A. J. Pung, M. K. Poutous, R. C. Rumpf, Z. A. Roth, and E. G. Johnson, "Two-dimensional guided mode resonance filters fabricated in a uniform low-index material system," vol. 36, no. 16, pp. 3293–3295, 2011.

[62] "SurPass 3000 Cationic Priming Agent," no. 814. DisChem, Ridgway, PA, pp. 1–9.

[63] "Microposit S1800 Series Photoresist." Shipley.

[64] "Microposit MF-319 Developer." Shipley.

[65] D. Adalsteinsson and J. A. Sethian, "A Level Set Approach to a Unified Model for Etching, Deposition, and Lithography I: Algorithms and Two-dimensional Simulations," *J. Comput. Phys.*, vol. 120, no. 1, pp. 128–144, 1995.

[66] D. Adalsteinsson and J. A. Sethian, "A Level Set Approach to a Unified Model for Etching, Deposition, and Lithography II: Three-Dimensional Simulations," *J. Comput. Phys.*, vol. 122, no. 2, pp. 348–366, 1995.

[67] D. Adalsteinsson and J. A. Sethian, "A Level Set Approach to a Unified Model for Etching, Deposition, and Lithography III: Re-Deposition, Re-Emission, Surface Diffusion, and Complex Simulations," *J. Comput. Phys.*, vol. 120, pp. 138–193, 1996.

[68] J. a. Sethian, "Evolution, Implementation, and Application of Level Set and Fast Marching Methods for Advancing Fronts," *J. Comput. Phys.*, vol. 169, no. 2, pp. 503–555, May 2001.

[69] J. C. Rey, "Void Development in Plasma Enhanced CVD Models," pp. 1–5.

[70] J. Nishii, K. Kintaka, and T. Nakazawa, "High-efficiency transmission gratings buried in a fused-SiO2 glass plate.," *Appl. Opt.*, vol. 43, no. 6, pp. 1327–30, Feb. 2004.

[71] A.-L. Fehrembach, D. Maystre, and A. Sentenac, "Phenomenological theory of filtering by resonant dielectric gratings.," *J. Opt. Soc. Am. A. Opt. Image Sci. Vis.*, vol. 19, no. 6, pp. 1136–44, Jun. 2002.

[72] S. Boonruang, A. Greenwell, and M. G. Moharam, "Multiline two-dimensional guided-mode resonant filters.," *Appl. Opt.*, vol. 45, no. 22, pp. 5740–7, Aug. 2006.

[73] S. Boonruang, "Two-dimensional Guided-Mode Resonant Structures for Spectral Filtering Applications," University of Central Florida, 2007.

[74] A. J. Pung, S. R. Carl, I. R. Srimathi, E. G. Johnson, and S. Member, "Method of Fabrication for Encapsulated Polarizing Resonant Gratings," *IEEE Photonics Technol. Lett.*, vol. 25, no. 15, pp. 1432–1434, 2013.

[75] "AZ ® MiR ™ 701 Photoresist Positive Tone i-line Photoresist Data Package." .

[76] "AZ 300 MIF Developer." Clariant, pp. 1–4.

[77] G. Kalkowski, U. Zeitner, T. Benkenstein, J. Fuchs, C. Rothhardt, and R. Eberhardt, "Direct wafer bonding for encapsulation of fused silica optical gratings," *Microelectron. Eng.*, vol. 97, pp. 177–180, Sep. 2012.

[78] P. J. K. Paterson, M. Res, and S. Symp, "Chemical Free Room Temperature Wafer To Wafer Direct Bonding," *J. Electrochem. Soc.*, vol. 142, no. 1, pp. 7–13, 1995.

[79] "Photolithography Resist Processes and Capabilities." [Online]. Available: http://www.cnf.cornell.edu/cnf_process_photo_resists.html.

[80] C. Mack, *Fundamental Principles of Optical Lithography*, no. Ic. John Wiley & Sons, 2007.

[81] M. J. Madou, *Fundamentals of Microfabrication: The Science of Miniaturization*, 2nd ed. Boca Raton, FL: CRC Press LLC, 2002.

[82] "Proximity X-ray Lithography," *Optipedia*. SPIE Press.

[83] B. J. Lin, *Optical Lithography: Here is Why*. Bellingham, WA: SPIE Press, 2010.

[84] L. R. Harriott, "Limits of lithography," *Proc. IEEE*, vol. 89, no. 3, pp. 366–374, Mar. 2001.

[85] E. J. Walker, “Reduction of Photoresist Standing-Wave Effects by Post-Exposure Bake,” *IEEE Trans. Electron Devices*, vol. ED-22, no. 7, pp. 464–466, 1975.

[86] J. J. Kelly and H. G. G. Philipsen, “Anisotropy in the wet-etching of semiconductors,” *Curr. Opin. Solid State Mater. Sci.*, vol. 9, no. 1–2, pp. 84–90, Feb. 2005.

[87] R. Leancu, N. Moldovan, L. Csepregi, and W. Lang, “Anisotropic etching of germanium,” *Sensors and Actuators*, vol. 46–47, pp. 35–37, 1995.

[88] R. C. Jaeger, *Introduction to Microelectronic Fabrication*, 2nd ed. Upper Saddle River, NJ: Prentice Hall, 2002.

[89] M. Pitchumani, “Additive Lithography Fabrication and Integration of Micro Optics,” University of Central Florida, 2006.

[90] H. Jansen, H. Gardeniers, M. De Boer, M. Elwenspoek, and J. Fluitman, “A survey on the reactive ion etching of silicon in microtechnology,” *J. Micromechanics Microengineering*, vol. 6, no. 1, pp. 14–28, Mar. 1996.

[91] M. Shearn, X. Sun, M. D. Henry, A. Yariv, and A. Scherer, *Semiconductor Technologies*. InTech, 2010, pp. 79 – 104.

[92] C. C. Welch and V. J. Genova, “Characterization and comparison of fused silica etch processes in fluorocarbon based ICP chemistries.” [Online]. Available: http://www.oxfordplasma.de/pla_news/Characterization of fused silica etch processes.pdf.

[93] “Plasma Enhanced Chemical Vapor Deposition,” 2013. [Online]. Available: http://www.oxford-instruments.com/products/etching-deposition-and-growth/plasma-etch-deposition/pecvd.

[94] “Gaussian Beams and the Knife-Edge Measurement.” Durham University Atomic and Molecular Physics Group, Durham, United Kingdom, pp. 1–6.

[95] I. A. Avrutsky and V. A. Sychugov, “Reflection of a beam of finite size from a corrugated waveguide,” *J. Mod. Opt.*, vol. 36, no. 11, 1989.

[96] J. M. Bendickson, E. N. Glytsis, T. K. Gaylord, and D. L. Brundrett, “Guided-mode resonant subwavelength gratings: effects of finite beams and finite gratings.,” *J. Opt. Soc. Am. A*, vol. 18, no. 8, pp. 1912–28, Aug. 2001.

[97] D. W. Peters, S. A. Kemme, and G. R. Hadley, “Effect of finite grating , waveguide width , and end-facet geometry on resonant subwavelength grating reflectivity,” *J. Opt. Soc. Am. A*, vol. 21, no. 6, pp. 981–987, 2004.